U.PORTO

FEUP FACULDADE DE ENGENHARIA
UNIVERSIDADE DO PORTO

Numerical studies on micro-combustion

António Manuel Pereira Cova

Supervisor:
Carlos Manuel Coutinho Tavares de Pinho

Co-Supervisor:
Alexandre Miguel Prior Afonso

A Thesis submitted for the degree of
Master of Science in Mechanical Engineering
to the Faculty of Engineering, University of Porto

Porto, July 2016

Acknowledgements

I take this opportunity to express my gratitude to Prof. Dr. Carlos M. C. Tavares de Pinho and Dr. Alexandre M. P. Afonso for the opportunity to participate in this project, for taking the time to share his expertise and for all the support and encouragement without which this dissertation would not have been possible.

To Dr. Albert Cuoci and his colleagues, from Politecnico di Milano, that developed the computational framework *laminarSMOKE* for OpenFOAM, which code was a fundamental pillar to the execution of this work, and for always being available to provide clarifications relatively the code and its use.

I must acknowledge the Faculty of Engineering, University of Porto (FEUP), particularly for providing access to the High Performance Computing (HPC), which made possible performing substantially more numerical simulations for this work.

A special thanks to Maria for always being beside me, and to all my friends from my hometown, Leiria, and Porto, to my friends from CF and from *República*, for taking this journey alongside me, and for all their support and advice in the most relaxing and exhausting moments. To all my friends in BEST (Board of European Students of Technology), a huge thanks for the good times we have been through and for the valuable lessons I will carry with me forever.

Finally, but most importantly, I would also like to thank my family for the amazing unconditional support I have always dreamed of, for acknowledging my own little successes and for always motivating me to give the best of myself and never to give up.

Abstract

Micro-combustion is being studied all over the world due to its high potential power source in the future, as the combustion of hydrocarbon fuels at micro-scale can have up to 60 times higher energy density compared with lithium batteries. The majority of researchers worldwide have been using commercial software, such as ANSYS Fluent® or other ANSYS products, which are indeed powerful Computational Fluid Dynamics (CFD) softwares but very expensive, making it less financially accessible to the combustion community.

Investigators from Politecnico di Milano developed a computational framework for the open-source OpenFOAM, a solver called *laminarSMOKE*, suitable for the modelling of multi-dimensional laminar flames, having shown a very good agreement with experimental values for macro and meso-combustion. However, its application for micro-combustion flows was not intensively studied yet, and this is what it is proposed to do in this work.

The numerical validation of the *laminarSMOKE* solver is firstly performed on premixed flames in 1D using H_2 and CH_4 as fuels, in the OpenSMOKE framework. Afterwards, two simulations of coflow diffusion flames were performed, one fed with a mixture of H_2/N_2 and the other fed with pure CH_4. Overall, the obtained results were in very good agreement with experimental values available for the different cases, proving *laminarSMOKE* code was indeed suitable for simulations at macro and meso-scale combustion.

Numerical simulations using the gas phase model were applied to micro-scale combustion flows to analyse its capability to correctly describe these type of flows. Several types of micro-combustion chambers and flows were simulated in order to assess the versatility of the gas phase model. It was concluded that *laminarSMOKE* is not capable of simulating a combustion flow in a micro-chamber autonomously, due to the fact that the surface to volume ratio increases deeply from macro to micro-scale and the heat loss through the combustor walls can no longer be neglected. Several thermal boundary conditions were employed in the computational domain attempting to simulate the existence of walls. Most of the applied boundary conditions lead to either sustainable flames with temperature and mass fraction profiles different from the results obtained by homologous studies, or no sustainable flames at all.

A new version of the *laminarSMOKE* code was developed, named *chtlaminarSMOKE*, that included the possibility of simulating combustor walls represented

by an additional solid domain in which only the energy equation is solved through a coupled approach with the fluid domain. This code was validated against analytical results in a case of transient heat transfer in a forced convection in laminar flow. Two numerical simulations were then performed, on laminar hydrogen micro-jet diffusion flames and hydrogen premixed flames in a cylindrical micro-tube. In both cases, the obtained results were substantially in better agreement than those obtained when neglecting the walls effects.

A numerical study was made on coflow diffusion flames fed with a mixture of H_2/N_2 to study the effect of inserting a porous media within the combustion chamber, on the emission of pollutant gases, at meso-scale. It was observed that the decrease of the temperature imposed at the porous surface also decreased the NO_x formation. Furthermore, reducing the size of the porous media, and consequently the porous holes that the combustion flow has to go through, results in higher velocities of the flow and therefore lower residence times, which leads to lower NO_x formation.

Resumo

A micro-combustão tem vindo a ser estudada em todo o mundo devido ao seu elevado potencial de fonte de energia no futuro, visto que a queima de combustíveis hidrocarbonetos à micro-escala pode ter até 60 vezes maior densidade de energia em comparação com as baterias de lítio. A maioria dos investigadores em todo o mundo tem utilizado softwares comerciais, como o ANSYS Fluent® ou outros produtos ANSYS, que são de facto poderosos softwares em *Computational Fluid Dynamics* (CFD), mas são bastante caros, tornando-os financeiramente menos acessíveis para a comunidade de combustão.

Investigadores do Politécnico de Milão desenvolveram uma aplicação para o *open-source* OpenFOAM, um *solver* chamado *laminarSMOKE*, adequado à modelação de chamas em regime laminar, multi-dimensionais, tendo mostrado uma boa concordância com os valores experimentais para a macro e meso-escala. No entanto, a sua aplicação para escoamentos de micro-combustão ainda não foi intensivamente estudada, e é isto que se propõe fazer neste trabalho.

A validação numérica do *solver laminarSMOKE* é primeiramente executada em chamas de pré-mistura em 1D usando H_2 e CH_4 como combustíveis, na plataforma OpenSMOKE. Posteriormente, foram realizadas duas simulações de chamas difusivas, uma alimentada com uma mistura de H_2/N_2 e o outra com CH_4 puro. No geral, os resultados obtidos estavam em muito boa concordância com os valores experimentais disponíveis para os diferentes casos, provando que o código *laminarSMOKE* era de facto apropriado para simulações de combustão à macro e meso-escala.

Simulações numéricas usando o modelo de fase gasosa foram levadas a cabo para escoamentos de combustão à micro-escala, para analisar a capacidade do modelo descrever corretamente este tipo de escoamentos. Vários tipos de câmaras de combustão e escoamentos foram simulados de modo a avaliar a versatilidade do modelo de fase gasosa. Concluiu-se que o *laminarSMOKE* não é capaz de simular escoamentos de combustão à micro-câmara de forma autónoma, devido ao facto que o rácio área-volume aumenta profundamente da macro para a micro-escala e a perda de calor através das paredes da câmara de combustão já não pode ser ignorada. Várias condições de fronteira térmicas foram aplicadas ao domínio computacional na tentativa de simular a existência de paredes. A maioria das condições de fronteira aplicadas resultaram em chamas sustentáveis com perfis de temperatura e de frações mássicas diferentes dos resultados obtidos por estudos homólogos, ou nem chamas sustentáveis foram obtidas.

Uma nova versão do código *laminarSMOKE* foi desenvolvido, denominado *chtlaminarSMOKE*, que inclui a possibilidade de simular as paredes da câmara de combustão representadas por um domínio sólido adicional em que apenas a equação da energia é resolvida, através de uma abordagem a par com o domínio fluído. Este código foi validado por comparação com resultados analíticos num caso de transferência de calor em regime transiente com convecção forçada em regime laminar. Posteriormente, foram realizadas duas simulações numéricas, micro-jato de chamas difusivas de hidrogénio e chamas de pré-mistura de hidrogénio num microtubo cilíndrico. Em ambos os casos, os resultados obtidos estão em substancialmente melhor acordo do que os obtidos quando se ignorou os efeitos paredes.

Um estudo numérico foi realizado em chamas difusivas alimentadas com uma mistura de H_2/N_2 para estudar o efeito da inserção de uma estrutura porosa, no interior da câmara de combustão, na emissão de gases poluentes, à meso-escala. Observou-se que a diminuição da temperatura aplicada à superfície dos poros também diminui a formação de NO_x. Além disso, a redução do tamanho da estrutura porosa, e consequentemente, dos poros que o escoamento de combustão tem de atravessar, resulta em maiores velocidades do escoamento e, por conseguinte, menores tempos de residência, o que leva a uma mais baixa formação de NO_x.

Contents

List of Figures

List of Tables

List of Symbols and Acronyms

$1D$	One-dimensional
$2D$	Two-dimensional
$3D$	Three-dimensional
$4G$	Fourth generation
a_P	Planck mean absorption coefficient
$a_{P,k}$	Extinction coefficient of species k
ASIC	Application-Specific Integrated Circuit
Bi	Biot number
BC	Boundary condition
$\mathbf{C}(\psi, t)$	Vector of rate of change of ψ due to convection
CFD	Computational Fluid Dynamics
CMOS	Complementary Metal–Oxide–Semiconductor
CPU	Central Processing Unit
Co	Courant number
C_P	Specific heat capacity at constant pressure of the fluid
$C_{P,s}$	Specific heat capacity at constant pressure of the solid
$C_{P,k}$	Specific heat capacity at constant pressure of individual species k
$\mathbf{D}(\psi, t)$	Vector of rate of change of ψ due to diffusion
δt	Time step
δx	Cell size in the direction of the velocity
Δt	Time interval
D_k	Individual-species mixture averaged diffusion coefficient
ϵ	Material emissivity
FD	Fully Developed
FREI	Flame with Repetitive Extinction and Ignition
$\mathbf{g}$	Gravitational acceleration vector
h	Convective heat transfer coefficient
H	Combustor height
HCCI	Homogenous Charge Compression Ignition
HPC	High Performance Computing
HRR	Heat Recirculation Reactor
h_k	Enthalpy of individual species
λ_f	Thermal conductivity of the fluid
λ_s	Thermal conductivity of the solid
MEMS	Micro-Electro-Mechanical System
MIT	Massachusetts Institute of Technology

MOL	Method of lines
ODE	Ordinary differential equation
Ω_k	Formation rate of species k
p	Pressure
ϕ	Equivalence ratio
Φ	Vector of mass fractions and temperature
p_k	Partial pressure of species k
$\mathbf{q}$	Heat flux vector
$\mathbf{q}_{rad}$	Radiative heat flux
$\mathbf{R}(\psi, t)$	Vector of rate of change of ψ due to chemical reactions
ρ	Density of the fluid
ρ_s	Density of the solid
RPM	Rotations per minute
Re	Reynolds number
σ	Stefan-Boltzmann constant
τ	Fluid stress tensor
T	Temperature
t	Time
T_{af}	Adiabatic flame temperature
T_{env}	Environment temperature
T_f	Flame temperature
T_{wall}	Wall temperature
Γ_{ij}	Binary diffusion coefficients
TPV	Thermophotovoltaic
u	Axial component of the flow velocity
$\mathbf{v}$	Velocity vector
v	Normal component of the flow velocity
V_c	Constant correction factor
V_k	Diffusion velocity of species k
V_c^k	Correction diffusion velocity
X_k	Mole fraction of species k
Y_k	Mass fraction of species k

Chapter 1

Introduction

1.1 Thesis context

The last years have experienced a huge development of micro and nano-fabrication technologies which consequently accelerated drastically the miniaturization and multi-functionalization of mechanical, electro-mechanical, portable, imaging, communicational and biomedical devices [1][2][3]. These devices require a compact, long lifetime, and instantly rechargeable power supply capable of providing power from several milliwatts to hundreds watts. However, nowadays, these devices are highly reliable on batteries, which suffer not only from short operation cycles between charges or replacements, but also from significant fractions of both mass and volume of the entire devices. As portable devices like cell phones and notebook computers keep being developed, so does the market demand for small power generators. Unfortunately, the energy density of the existing batteries, even the lithium ones which are considered to be the most advanced, is very low. It is about 0.20 kWh/kg, can only support a few hours for notebook computers and video cameras, apart from the fact that they take several hours to recharge, with a limited number of rechargeable cycles. Additionally, the batteries after use disposal represent a major environmental concern.

Similarly to the aforementioned, other more advanced devices, with higher precision required, are being fabricated using Micro-Electro-Mechanical Systems (MEMS), demonstrating the efforts being made towards the integration of micro-electronic and micro-mechanical systems on a single chip. Although initially the micro-devices produced using MEMS were mostly sensors and actuators, recent more complex devices like motors, pumps and micro-airplanes are being developed. Unfortunately, current MEMS are still relying on an external power source. The lack of compact, durable, efficient, light weighted and instantly rechargeable power sources is limiting the development of such devices, exampled in Figure 1.1.

Therefore, there is a high need to combine MEMS with micro-power generation. The existence of efficient micro-power generators will substantially enhance the functionality of MEMS for numerous portable devices: (1) 4G cellular phones and notebook computers requiring increased energy density and reduced recharge time; (2) biomedical devices needing higher efficiencies and more compact power sources. In order to reduce system weight, increase operational lifetimes and reduce

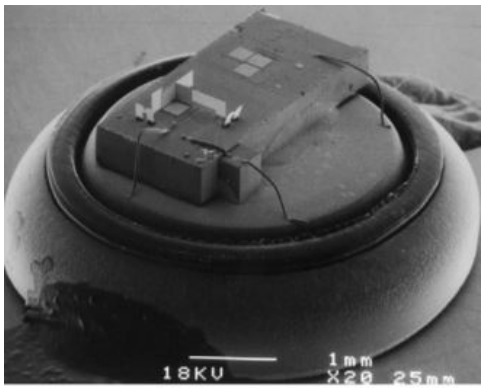

Figure 1.1: Autonomous bidirectional communication mote with a MEMS optics chip containing a corner-cube retroreflector on the large die, a CMOS application-specific integrated circuit (ASIC) for control on the 300 x 360 micron die, and a hearing aid battery for power. The total volume is 63 mm^3 [3].

unit cost, the field of micro-power generation has been engendered and the attentions were directed to the potential of high energy density of hydrocarbon fuels. The concept behind this new field was to use the high energy density of these fuels in combustion driven micro-devices to generate power. Table 1.1 and Figure 1.2 show the comparison of energy densities between existing batteries and hydrocarbon fuels.

Table 1.1: Energy densities of different sources. The energy density of combustion-based sources is based on complete combustion to carbon dioxide and liquid water, at 298 K and 1 atm [4]

Source	Energy density [MJ/kg]
Lead acid batteries	0.0792
Nickel cadmium (NiCad) batteries	0.158
Lithium ion batteries	0.468
Lithium sulfur batteries	0.792
Methanol combustion	22.7
Ethanol combustion	30.5
Heating oil combustion	42.5
Diesel combustion	45.3
Gasoline combustion	45.8
n-Octane combustion	48.2
n-Butane combustion	49.6
Propane combustion	50.3
Methane combustion	55.5
Hydrogen combustion	142

It can be seen that the lithium battery with highest energy density, around 0.8 MJ/kg, corresponds approximately to one sixtieth of the hydrocarbon fuels, typically around 45 MJ/kg. Moreover, the energy density of hydrogen fuel is around 180 times higher than that of lithium. Although the energy conversion efficiency still has a long way to go, even with 10% efficiency, the energy density of a micro-combustor is still 6 times greater than that of lithium batteries.

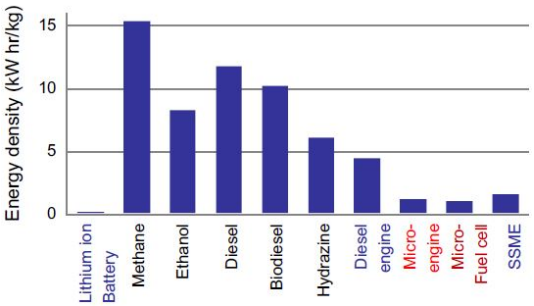

Figure 1.2: Comparison of specific energy densities of lithium ion batteries with hydrocarbon and oxygenated hydrocarbon fuels as well as different engines [2].

These potential advantages, in terms of unit per mass (depicted in Table 1.1 and Figure 1.2) and of unit per volume, were eloquently illustrated around 30 years ago at the 1974 International Symposium on Combustion by Felix Weinberg: *"I can put several million Joules safely into my pocket in the form of a large tin of lighter fuel. The cost of petroleum would have to rise several hundred times before the price of such a tin would approximate to that of, for example, electrical storage batteries for a comparable amount of energy - and then they would be too heavy for me to pick up."* [5].

As such, micro-combustion of hydrocarbon fuels have the potential to replace lithium batteries and deliver way higher power for the development of MEMS for biomedical applications, telecommunications, chemical sensing and micro-propulsion.

1.2 Objectives

Micro-combustion is being studied all over the world due to its high potential power source in the future. Combustion of hydrocarbon fuels at micro-scale can have up to 60 times higher energy density compared with lithium batteries. However, micro-scale combustion still has several practical limitations in its design and performance, and that is the reason why currently is being subject to extensive investigation, both numerically and experimentally. The majority of investigators worldwide have been using ANSYS Fluent® or other ANSYS products, which are indeed powerful computational fluid dynamics (CFD) softwares. However, the fact that their cost can be from 15 up to 30 thousand euros with additional 3 to 6 thousand euros for an annual license and updates, makes it less financially accessible to the whole scientific and commercial community.

On the other hand, investigators from Politecnico di Milano developed an application for the open-source OpenFOAM, a solver called *laminarSMOKE*, suitable for the modelling of multi-dimensional laminar flames, both for steady and unsteady flows and for structured an unstructured meshes. This solver was released as an open-source code for the whole combustion community, which was welcomed to use and improve it. However, the application of this new computational framework for micro-combustion flows was not intensively studied yet.

In this thesis, with the previous arguments in mind, the author will firstly validate the previously mentioned solver on premixed and diffusion mesoscale flames, using hydrogen and methane as fuels, to establish ground credibility concerning the following numerical studies. Secondly, the author will study numerically micro-scale combustion using the *laminarSMOKE* code for several, but in general, simple geometries using the hydrogen and methane fuels, and compare the obtained results with available literature. This comes with the greater goal to validate the capability of *laminarSMOKE* to correctly describe micro-scale combustion flows. Thirdly, it is proposed to perform a numerical study on diffusion flames fed with a hydrogen/nytrogen mixture with a porous media inserted within the combustion chamber with different geometries, in order to analyse the effect of the porous media on the emission of pollutant gases such as NO_x, CO and CO_2.

1.3 Thesis outline

This thesis is divided into nine chapters and three appendixes.

In Chapter 2, a literature review on the fundamental concepts and definitions of combustion is given, followed by the presentation of the main discoveries in the field of micro-combustion.

In Chapter 3, the governing equations in micro-combustion flows are presented as well as a brief description of the numerical model adopted to solve the mentioned equations.

In Chapter 4, the main pre-processing, running and post-processing tools and features provided by OpenFOAM software are briefly explained, in order to give the reader the insight of setting up simulations for the following chapters.

In Chapter 5, numerical validations of the *laminarSMOKE* solver are made, in order to ensure that the installation of OpenFOAM and respective libraries are working properly, and that the results obtained are credible.

In Chapter 6, numerical studies are made both for diffusion and premixed flames using the presented *laminarSMOKE* solver. For each study, the simulation setup as well as the results and discussion are presented.

In Chapter 7, a new solver that includes simultaneously solid and gas phase modelling, based on *laminarSMOKE* solver, is created. A numerical simulation is performed in order to validate the new solver.

In Chapter 8, several numerical studies carried out in Chapter 6 using *laminarSMOKE* solver, are repeated here using the created solver in Chapter 7.

In Chapter 9, the main conclusions and the future work that should be addressed are presented.

In Appendix A, the detailed kinetic mechanisms are presented for H_2 fuel with and without NO_x.

In Appendix B, there are displayed the graphics involving the evolution of average temperature, heat released and OH, NO_x, CO and CO_2 mass fraction profiles in time until reaching steady-state, regarding the investigation on diffusion flames with a porous media inserted within the combustion chamber.

In Appendix C, it is shown the content of the two main files that were manipulated to create the new solver including the solid modelling.

Chapter 2

Literature review

2.1 Combustion concepts and definitions

In the present subchapter will be presented the main combustion concepts and definitions, based on [6][7].

2.1.1 Stoichiometric reactions

Combustion, whether in macro, meso or micro scale, is an exothermic chemical reaction between a substance, the fuel, and a gas, the oxidizer, normally oxygen, when they are in suitable conditions, to release heat. In most practical devices, air is used as an oxidizer that consists approximately of 21% of oxygen (O_2) and 79% of nitrogen (N_2) in molar concentration:

$$\text{Air} = 0.21O_2 + 0.79N_2 \Rightarrow 4.76\text{Air} = O_2 + 3.76N_2 \tag{2.1}$$

To describe the combustion process, it is necessary to know the chemical reaction related to the process, which indicates how the reactants atoms bond with each other resulting in the reaction products. Knowing that the mass of each element remains constant during and after the reaction, the number of reactants and products molecules can be easily obtained. Because this study will focus only on the micro-combustion characteristics of two fuels, hydrogen (H_2) and methane (CH_4), the respective global chemical reactions with the oxygen from air are presented below, respectively:

$$H_2 + O_2 + 3.76N_2 \rightarrow 2H_2O + 3.76N_2 \tag{2.2}$$

$$CH_4 + 2O_2 + 7.52N_2 \rightarrow CO_2 + 2H_2O + 7.52N_2 \tag{2.3}$$

These chemical reactions are presented in the stoichiometrical form, a condition where is assumed that the reactants are completely consumed through the process although it should be mentioned that N_2 is assumed to be an inert gas, not participating in the chemical reaction. This would be how a combustion process would reach the highest efficiency. However, practically, it is known complete combustion is impossible to achieve, unless the amount of oxidizer is higher than the one theoretical needed. This happens because the characteristics of the used burners and the flow itself do not allow the execution of perfectly homogeneous fuel

air mixtures.

2.1.2 Equivalence ratio

The equivalence ratio ϕ, indicates the deviation of fuel and air quantities provided for a combustion process, relatively to its stoichiometrical state:

$$\varphi = \frac{\left(\frac{F}{A}\right)}{\left(\frac{F}{A}\right)_s} \tag{2.4}$$

where F/A expresses the fuel-air mass ratio of the chemical mixture, while the subscript s represents the stoichiometrical state. Naturally, if $\varphi = 1$, it means that the fuel-air mixture is stoichiometric. If $\varphi < 1$, the mixture is referred as fuel-lean, while if $\varphi > 1$ it is called fuel-rich.

At this point, it is also relevant to present the definition of mass fraction Y_k, which is the ratio of a specie with mass m_k to the mass of the total mixture m_{tot}. Summing all species mass fractions together equals to 1.

$$Y_k = \frac{m_k}{m_{tot}} \tag{2.5}$$

$$\sum_{k=1}^{\infty}(Y_k) = 1 \tag{2.6}$$

The quantity of a specie can also be expressed in terms of mole fraction X_k, which is defined as the amount of a constituent, n_k, divided by the sum of all constituents in a mixture, n_{tot}. Summing all species mole fractions together equals to 1.

$$X_k = \frac{n_k}{n_{tot}} \tag{2.7}$$

$$\sum_{k=1}^{\infty}(X_k) = 1 \tag{2.8}$$

2.1.3 Flame temperature

The minimum temperature above which the chemical reaction accelerates releasing huge amounts of heat, is called the autoignition temperature. Most commonly, combustion is initiated by supplying an exterior heat source to a small fraction of the mixture, followed by combustion reactions which, in certain conditions, may spread throughout all mixture volume. What separates this reaction zone, that is constantly spreading, from the unburned reactants, is the so called flame front. The autoignition temperature depends on the nature and composition of the mixture in question. Table 2.1 presents autoignition temperatures for hydrogen and methane.

Associated to the autoignition temperature, there is also the minimum amount of energy supply above which the mixture will ignite, which also depends on the composition of the mixture. Once ignited, the flame will only propagate across the

Table 2.1: Autoignition temperatures of hydrogen and methane [7]

Fuel	Autoignition temperature (K)	
	With pure oxygen	With air
H_2	833.15	843.15
CH_4	827.15	853.15

mixture if the fuel concentration lies within well-defined lower and upper bounds determined experimentally, referred to as flammability limits, specified in Table 2.2. These limits are also called the lean and rich flame propagation limits.

Table 2.2: Flammability limits and flame properties for some common fuel gases at atmospheric pressure. The flammability limits apply to upward propagation in tubes. The flame temperature refers to stoichiometric mixtures, except those marked $*$ which are maximum values [8]

Reactants	Flammability limits (% by volume)		Adiabatic flame temperature (K)	Maximum burning velocity (m/s)
	Lower	Upper		
$H_2 + O_2$	4.0	94	3083	11.0
$CO + O_2(+H_2O)$	15.5	94	2973	1.08
$CH_4 + O_2$			3010	4.5
$C_2H_2 + O_2$			3431	11.4
H_2 + air	4.0	75	2380	3.1
CO + air	12.5	74	2400	0.45
CH_4 + air	5.3	15	2222	0.45
C_2H_2 + air	2.5	80	2513	1.58
C_2H_4 + air	3.1	32	2375	0.75
C_2H_6 + air	3.1	15	2244*	0.40
C_2H_8 + air	2.2	9.5	2250*	0.43
n-C_4H_{10} + air	1.9	8.5	2256*	0.38
C_6H_6 + air	1.5	7.5	2365*	0.41
C_2H_3OH + air	3.0	80	2411*	1.05

The flame temperature T_f is one of the most important parameters when characterizing a combustion process. It is determined by the energy balance between the existing reactants and products at equilibrium. In case the reaction zone is very small comparing with the rest of the domain, then it is common practice to denote the maximum temperature in the reaction zone to be the flame temperature. If the combustion process takes place in an adiabatic chamber, then the flame temperature is referred to as adiabatic flame temperature T_{af}. It consists on the maximum temperature for a combustion process with a given fuel, because every heat transfer to outside of the chamber or any incomplete combustion would decrease the temperature. In most cases, calculating T_{af} values is more accurate than obtaining them experimentally. For most hydrocarbons, the maximum flame temperature occurs for equivalence ratios slightly higher than 1 ($\varphi \sim 1.05$). Table 2.2 presents T_{af} values for some characteristic fuels.

2.1.4 Classification of flames

Flames can be classified in different ways, depending on how the fuel and oxidizer reach the reaction front. There are non-premixed flames, partially and fully premixed flames, as well as flames that are categorized in stirred reactor or plug flow reactors, and more [9]. Since this thesis will only focus on non-premixed and premixed flames, only them will be presented next.

2.1.4.1 Non-premixed or diffusion flames

In non-premixed combustion, the fuel and oxidizer are separated until they reach the reaction zone. They enter the reaction zone through the diffusion of reactants and leave as products. The reaction zone is located where the total enthalpy of reactants equals the total enthalpy of products plus any energy losses. Therefore, ideally the reaction should take place at stoichiometric conditions, to maximize the flame temperature released as much as possible for a certain reactant mixture. A particular case of non-premixed flames, known commonly as coflow flames, is distinguished when both fuel and air streams flow in parallel and separated from one and the other until reaching the reaction zone [9].

2.1.4.2 Fully premixed flames

In premixed flames, the fuel and the oxidizer are thoroughly mixed before they reach the reaction zone. In these flames, the reaction zone is defined by balancing the local velocity of the reactants with the rate of consumption of the reactants, known as flame speed (see Section 2.1.5). Such flames can be burned at equivalence ratios different than 1, making it possible to achieve lower temperatures [9].

2.1.5 Flame speed

The flame speed is defined as the local velocity of the reactant mixture normal to the reaction. The flame speed is mainly dependent on the value of the flame temperature. Therefore, if there is a variation of the equivalence ratio, that determines the adiabatic flame temperature, there will be a variation of the flame speed [10]. In table 2.2 is presented the maximum burning rates for several characteristic fuels [9].

2.1.6 Flashback and blow off

In premixed flames, there are situations when the supply velocity of the reactant may be lower or higher than the flame speed. When is lower, the flame propagates upstream towards the incoming reactants, phenomena known as flashback. On the opposite case, if the supply velocity is higher than the flame speed, then the flame

moves downstream, the so called blow off [9].

2.1.7 Flame regimes at micro-scale

Three types of flames responses are commonly distinguished in order to better characterize a micro-combustion process. There are normal flames, FREI (Flame with Repetitive Extinction and Ignition) and weak flames. Each of them for different flow velocities, and their flame temperature also depends on the fuel and equivalence ratio in question. Figure 2.1 illustrates these different responses for a stoichiometric mixture of methane, oxygen and carbon dioxide.

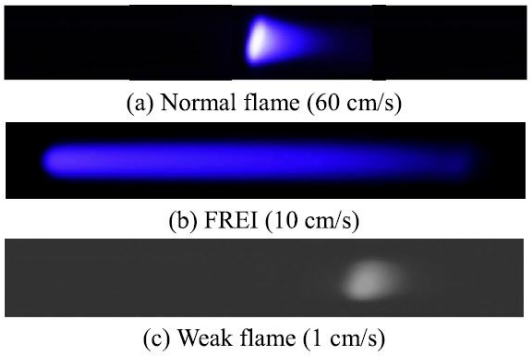

Figure 2.1: Flame images of the stoichiometric $CH_4/O_2/CO_2(X(O_2)/X(CO_2) = 0.62)$ mixture at different inlet flow velocities in the micro flow reactor [11].

2.2 State of the art

2.2.1 Scaling parameters of micro-combustion

In the last decade, several MEMS have been developed. Due to the arbitrary choices of reference dimension scales, the definition of "micro-scale combustion" is ambiguous and sometimes confused with "mesoscale combustion". In general, in previous studies, to distinguish these two concepts, the most objective and used reference length scales were: (1) if the combustor physical length scale is below 1 mm, it is considered to be micro-combustion, otherwise, if the physical length scale is greater than 1 mm, then it is called mesoscale combustion; (2) if the combustor size is smaller than the flame quenching diameter, it is called micro-combustion, but if it is bigger, it is called mesoscale combustion. Note that the quenching diameter is defined as the minimum tube diameter below which a flame fails to propagate along the channel. In the case of flat plates, it is commonly referred to as quenching distance [12]. While the combustor physical length scale was widely used in the development of micro-engines, the flame quenching diameter reference was more favored by researchers for fundamental studies of micro-combustion [2].

As a consequence of reducing from macro to meso or micro-scale, most of the flows become laminar, which simplifies the numerical analysis when compared with turbulent flows. In fact, this study will only focus in laminar flows.

2.2.2 Progress made

The progress of the micro technology allowed the development of prototypes involving micro-combustion. For instance, in 1997, Epstein et al [13] designed and developed a micro-gas turbine generator capable of producing 10 to 20 W of electric power consuming 10 grams per hour of H_2.

Later on, Mehra et al [14] managed to reach a stable combustion with hydrogen in a micro-fabricated silicon combustor chamber of 66 mm^3, for a gas turbine, where exit gases temperature reached 1800 K. This device was the first demonstration of high power density micro-combustion system, around 2000 MW/m^3.

Tanaka and Esashi [15], in 2007, developed the smallest gas turbine in the world, using a Brayton cycle with a rotation of 360000 RPM and a combustor temperature between 800 and 900 ^oC.

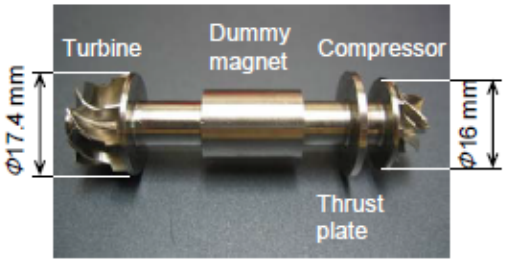

Figure 2.2: Rotor with compressor and turbine impellers [14].

There were also advances in internal combustion engines using micro-combustion, Fernando et al [16] developed rotationary engines in micro and mesoscale, using liquefied hydrocarbon fuel, reaching in micro-scale an output in the order of milliwatts. In terms of mesoscale, they got an output of 2.7 W, with a rotation of 9300 RPM, but with low thermal efficiency – less than 0.5%, caused by the low compression rate and leakages between the rotor and the support box.

As an alternative to solve the sealing problems, it was developed an engine with a specific piston in mesoscale, Aichlmayr et al [17], with Homogeneous Charge Compression Ignition (HCCI) using hydrocarbon fuel, having in mind the goal of reaching 10 W of electric power for a 1 cm^3 volume. It was concluded that correcting the leakage problems limited the fuel conversion efficiency and shorten the engine lifetime due to high wear of the materials.

Another option in micro-power generation was the combination of micro-reactors with energy conversion devices, such as thermoelectric, thermophotovoltaic and piezoelectric, with the advantage of absence of friction caused by movable parts. In this type of devices, the thermal control is necessary to obtain stable combustion sustained in extremely small scale reactors, and normally this control is done by heat recirculation and the usage of catalysers. The first studies being developed in this area were done in the 70's, Weinberg [18][19], combining a thermoelectric device with a combustion chamber in a "Swiss-roll" shape to maximize the system

efficiency, through the reduction of heat loss from the system to the environment.

Even with the experimental studies done so far, it is not possible to obtain detailed analysis of the micro-combustion phenomena, due to its scale factor, i.e., the impossibility to insert measurement instruments in the micro-devices. For that reason, numerical studies were carried out with the goal of better understanding the aforementioned phenomena. In this sense, the first numerical studies emerged as a consequence of the prototypes development involving micro-combustion, like the gas micro-turbine of MIT [13].

Spadaccini et al [20] made an experimental and numerical study with the objective of better understanding the effects of micro-combustion in the gas micro-turbine of MIT, so that they could obtain a better energy efficiency, considering diverse aspects: stable ignition, flammability limits range, conversion efficiency from chemical to kinetic and thermal energy of the fluid with low total pressure loss. However, these obstacles are difficult to overcome in micro-scale, due to the low residence time to complete combustion and due to the high heat loss from the combustion chamber. The numerical simulation consisted in obtaining the temperature and velocity fields in the combustion chamber with two annular and slotted injectors, allowing to study the importance of the recirculation zones in micro-combustion, to a rapid and uniform reactants ignition.

Another effect of the reduction for micro-scale, analysed through 2D numerical simulations in a microchannel, using parabolic and elliptical models, was the flame quenching due to two primary effects: thermal and radical, Raimondeau et al [21]. Both mechanisms are generated by the wall effect, the thermal quenching occurs when the heat from the combustion chamber removed through the wall is high, in a way that the combustion is no longer auto-sustainable, while the radical quenching is caused by the absorption of radicals at the wall and their subsequent recombination, resulting in a deficit homogeneous chemistry. For that reason, a careful choice of the wall material of the combustion chamber, in terms of insulating and radical quenching properties, is essential for flame propagation, and therefore, becomes crucial to project. Comparing the two models used for simulating temperature and mass fraction fields, it was verified that for the parabolic model there is an over-prediction of the ignition distance.

Based on the previous study, the numerical simulations of Norton and Vlachos [22] were solved exclusively on the elliptical model to study the thermal effects in the wall, analysing the wall thermal conductivity and thickness, external heat loss, dimensions of the combustion chamber and operation conditions, with the objective of obtaining an auto-sustainable methane/air mixture flame. The study allowed to discover that wall thermal conductivity and thickness have an important role in the flame ignition and in its stability, because they determine the heat flux upstream. With thick walls or high thermal conductivities, these have a tendency to become isothermal-like and with lower temperatures. Despite of being a larger heat source for external heat transfer, they become susceptible to induce spatially global-like extinction. In the opposite case, low thermal conductivity walls, limit the heat transferred upstream, consequently limiting the fuel pre-heating, inhibiting the

beginning of combustion and causing extinction. Both extreme situations reduce flame stability, confirming that these aspects are to be considered at micro-scale. Optimum values for the wall thermal conductivity should vary between 3 and 5 W/(mK), typical of ceramics, for a two-parallel plates combustor length of 1 cm and height of 600 μm. It was also verified the importance of the flow rate on the flame stability. For higher values, there is a decrease of heat transfer upstream and this may cause the extinction. For low flow rates, the flame may extinct because the conductive heat transfer becomes dominant, expanding the reaction zone and increasing substantially the heat loss for the exterior, in a way that outperforms the heat generation to sustain the combustion. In this study, the optimal value of flow velocity was around 0.5 m/s.

The reduction to micro-scale in micro-combustion requires a more detailed analysis in terms of project due to parameters that initially, in macro-scale, were not considered due to its small impact in the flame stability, like the effect of wall thermal conductivity of the combustion chamber. For that reason, Hua et al [23], conducted a fundamental numerical study of combustion of hydrogen/air mixtures in micro-scaled chambers, varying the scale factor of the combustion chamber, and verified that, if they reduced the scale they would be also reducing the reactant residence time thus originating an incomplete and possibly unsustainable combustion, i.e., a low efficiency combustion can create a heat generation deficit to reach an auto-sustainable combustion, hence occurring quenching. Note that, theoretically, to obtain a complete combustion it is necessary that the reactants residence time is higher than the chemical reaction time, but with the scale reduction the chemical reaction time remains the same while the residence time strongly decreases. In these simulations, it is indicated that stable combustion may only be obtained through increasing the ratio of flow residence time to chemical reaction time.

Hua et al [23][24], simulated numerically the prototype of the gas micro-turbine of MIT in 3D, to analyse the performance of the combustion chamber, and presented ranges for the operating parameters such as equivalence ratios, flow rates, heat loss transfer rate and materials, to obtain higher efficiencies.

With the objective of improving the thermal efficiency of the combustion chamber, Federici and Vlachos [25] presented a numerical study to analyse the flame stability of a propane/air mixture with heat recirculation in the reactor (HRR), and compared it with a reactor in a simple channel. They concluded that, on the verge of highly conductive inner walls or low entrance velocities, the system is susceptible to extinction and the effect of stability is similar to both situations. On the opposite, with low-conductivity walls or high velocities, the system with recirculation is much more stable, because the recirculation gases and the outer wall provide additional heat to the cold reactants in the transversal direction, causing ignition and flame stabilization. Summing up, the heat recirculation has a great influence in the extinction mode or flame stability. The obtained results were qualitatively according to the data of Kaisare e Vlachos [26]. To be noted, these simulations were conducted in a commercial CFD program.

Li et al [27], also using a commercial CFD program, simulated a cylindrical

combustion chamber and compared it with a 2D parallel plates channel (tridimensionally a rectangular channel) combustor, using a methane/air mixture. The study consisted in varying the dimensions, geometry and boundary conditions of the combustion chamber, as well as the inlet velocity profiles, having in mind their effect on the flame temperature, since this is one of the most important parameters to characterize the combustion process. For normal operating conditions, it was verified that the flame temperature in a 2D channel, of 1 mm height, is higher than that of the cylindrical tube with 2 mm diameter (hydraulic equivalent diameter), for the range of simulated velocities. In the typical limit situations, the flame temperature remained practically equal. As far as the velocity profiles were concerned, a fully developed profile had the flames anchored further from the entrance compared to the uniform profile, but no significant differences of the flame temperature were observed.

Aikun et al [28], simulated the combustion of a hydrogen/air mixture in a 3D rectangular micro-channel, using a commercial CFD program, and analysed the effect in the flame temperature and length, when varying the inlet velocity, channel height and wall material. The temperature fields clearly showed the preheating, combustion and cooling region, where the mixture ignites and anchors near the entrance in a cone-shaped structure. The combustion remained stable and persistent for a wide velocity range, even in the limit cases the extinction phenomena does not occur. In relation to the channel height, for the studied range, the bigger it is, the higher the flame temperature can get – for $H = 0.2$ mm the maximum was 1915 K, for $H = 0.8$ mm it was 2431 K.

Li et al [29] also conducted numerical simulations for premixed hydrogen/air flames, in cylindrical and parallel plates micro-channels, to study the aforementioned aspects and highlighted the importance of axial heat conduction to preheat the unburned mixture. They verified the influence of axial heat conduction in widening the flame stability, but also noticed that for low inlet velocities, where there is practically no contact between the wall and the unburned mixture, the axial conduction practically does not influence.

In relation to the conduction phenomena and wall properties of a combustor, Norton and Vlachos [22][30] further suggested that the ideal case is when the combustor has anisotropic properties, which allows axial but inhibits transverse heat conduction, in which case the heat loss is minimised while the heat recirculation is maximised.

Rahaghi et al [31], based on a two-dimensional numerical approach, additionally studied the effects of a micro-combustor external convection heat transfer coefficient on the flame temperature and species mass fraction profiles. They verified that the higher the external convection heat transfer coefficient, the lower the temperature inside the combustor. The temperature seemed to decrease 2 to 3 times more next to the wall compared to the centreline of the combustor.

In order to further develop the micro-thermophotovoltaic systems, Li et al [32] undertook an experimental study to analyse the possibility of extending flame stability limits of premixed hydrogen/air in a H = 1 mm planar micro-combustor, since

this aspect is very important to its design and operation. It was found that, when the combustor is filled with porous medium, it widens the flame stability limits, especially for the flashback critical conditions. Note that inserting a porous medium in a combustion chamber reduces the flame temperature, besides making this happen consequently reduces pollutants emissions, such as NO_x and CO, which represents a major environmental concern nowadays [33].

In the area of diffusion flames, Cheng et al [34] conducted a detailed measurement and assessment of laminar hydrogen jet flames with non-intrusive experimental techniques, and compared the obtained data with computed results. The ability to predict the effects of the complex transport phenomena associated with the chemical kinetics of these type of flames, most common in practical combustion devices, is critical to improve efficiencies, as well as better understanding of flame extinction and pollutant formation. Flows with Re = 30 and Re = 330 were investigated, and it was observed that thermal diffusion affected more the flame structure in the higher Reynolds number, whereas it became minor in the lower one. Five different chemical kinetics were used to investigate the flame structure for Re = 30 and no major differences were observed among them. The effects of the burner wall on the flame structure were also computed, and the obtained results suggested a more severe effect for lower Reynolds number flows. It also suggested that considering a variable wall temperature would lead to a better agreement between the computed and measured data. The complete measurements of laminar hydrogen jet diffusion flames in this experiment provided a benchmark for development and validation of CFD codes. Hossain et al [35] investigated deeper the effects of different burner wall materials on the thermal and chemical structures of laminar hydrogen jet flames. They verified that even with extremely low Reynolds number, a flame, although tiny, could be stabilized due to the effective usage of the burner wall properties and heat transfer.

2.2.3 Current applications of micro-combustion

The chemical energy which is released during the process of combustion can be exploited in different ways, as it is represented in Figure 2.3, such as: (1) heating systems; (2) electricity production; (3) driving endothermic reactions, like reforming; (4) mechanical work.

Fernandez-Pello et all [36] and Weinberg et al [37] reviewed the concept of converting combustion heat to electricity, and this is possible either with photovoltaic or thermoelectric devices integrated to the micro-burner. Through coupling a Swiss-roll micro-burner, in Figure 2.4, with a thermoelectric element, it is possible to directly convert thermal energy to electrical energy. Net power outputs from 50 to 600 mW, using this method, have been obtained, [38][39], and another substantial improvements in thermal efficiency of such systems can be seen in [40]. The advantage of these devices is that they do not have movable parts, therefore, are not susceptible to mechanical fracture or wear.

Thermophotovoltaics (TPV) devices coupled with micro-burners represent another way of directly converting thermal to electrical energy. Many were already de-

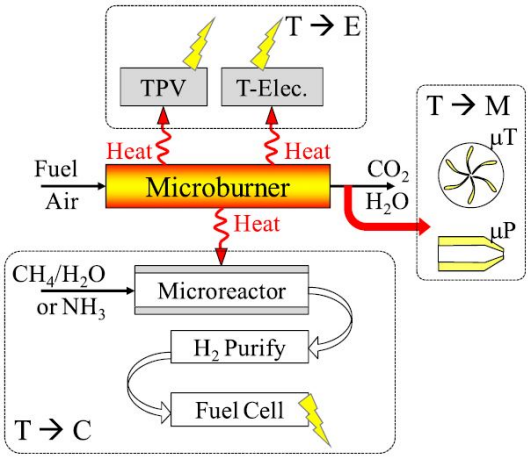

Figure 2.3: Schematic of utilization paths for thermal energy released on micro-combustion. The thermal energy is used as a heat source to drive thermoelectric elements, an endothermic reactor producing H_2 or a micro-turbine (μT)/micro-propulsion (μP). The micro-turbine may then convert mechanical energy to electrical energy. "$T \rightarrow E$" (thermal to electrical), "$T \rightarrow C$" (thermal to chemical) and "$T \rightarrow M$" (thermal to mechanical) [4].

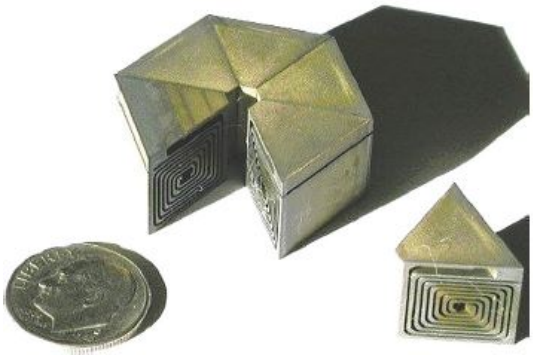

Figure 2.4: 3-D "Swiss-roll" type combustor [P. Ronney, CPL, USC] [3].

signed, managing to have an electricity power output from 0.92 to 4 W [41][42][43].

The heat generated during the process of combustion can also be a source of micro-reactors to drive endothermic reactions. The goal behind is process intensification, known as the activity that improves the yields and selectivities of chemical reactions at more extreme parameters, only safely possible in micro-scale. With this, by reducing system sizes and enabling heat transfer from the combustion process to the endothermic chemical reaction, through thin conductive walls, the time scale of heat transfer is reduced by orders of magnitude. The usage of catalysts next to the walls can reduce the processing time, as represented in Figure 2.5. For instance, the time scale of reforming methane from a conventional reactor to a micro-reactor can be reduced from seconds to microseconds. To sum up, the result is a more compact and intensified unit, with a thermal efficiency higher than that of conventional reformers [4].

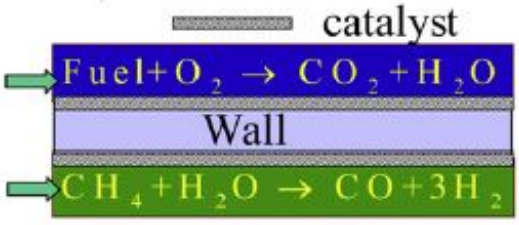

Figure 2.5: Blowup of two adjacent channels in thermally coupled micro-reactor, for a methane steam reformer [4].

In 1997, the MIT Gas Turbine Lab developed one of the first micro-scaled heat engines. Since then, micro-turbines and heat engines designs have undergone a series of changes and improvements, to face keys issues like lack of stable combustion, thermal management, friction, leakages, and more, as described in Section 2.2.2.

Micro-combustion also represents a good alternative when compared to conventional propellants, to deliver low thrust (around 1 mN) and low impulse bits (around 10-5 Ns), for precise behaviour and positioning control of micro-satellites [44].

A MEMS prototype thruster containing 15 individual thrusters in a 3 by 5 array was developed by TRW, Aerospace Corporation and Caltech [45], and it is represented in Figure 2.6. Each chamber had a volume of nearly 0.5 mm^3, and was able to produce 0.1 mNs of impulse, 0.1 N of thrust, and around 100 W of mechanical power.

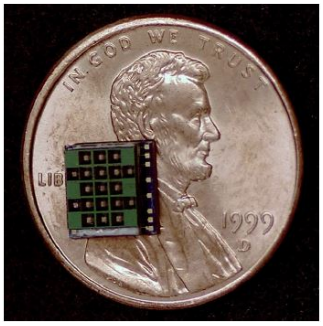

Figure 2.6: MEMS fabricated array of "Digital-Propulsion" micro-thrusters [3].

At MIT [46], in order to improve the performance of micro-thruster, a high pressure, bi-propellant micro-rocket engine has been manufactured and tested. The chamber, with around 100 mm^3, was able to produce 1 N thrust and a specific impulse of 300 Ns, and delivered a thrust power of 750 W, represented in Figure 2.7.

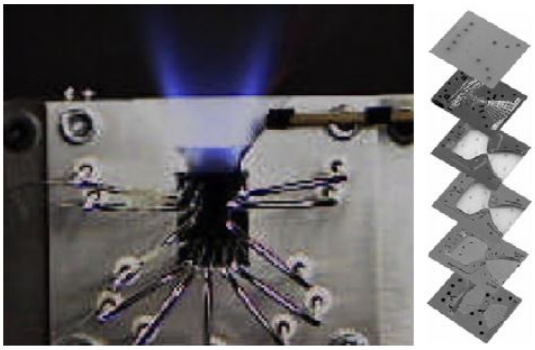

Figure 2.7: A bi-propellant micro-thruster developed at MIT [46].

Chapter 3

Governing equations and numerical modelling

This chapter has the purpose of presenting the governing equations in the combustion process, as well as the numerical framework adopted to solve the governing equations, based on [47][48]. These matters will be presented briefly, once approaching all of the numerical methods implied within the framework is beyond the scope of this document.

3.1 Governing equations

The reactive, laminar flows that will be investigated in the present work are mathematically described by the conservation equations for continuous, multicomponent, compressible, thermally-perfect mixture of gases, considered as Newtonian fluids. The conservation equations of total mass, mixture momentum, individual species mass fractions and mixture energy, are reported in the following:

$$\frac{\partial \rho}{\partial t} + \nabla(\rho \mathbf{v}) = 0 \tag{3.1}$$

$$\frac{\partial}{\partial t}(\rho \mathbf{v}) + \nabla(\rho \mathbf{v}\mathbf{v} + \mathrm{p}\mathbf{I}) = \nabla\tau + \rho\mathbf{g} \tag{3.2}$$

$$\frac{\partial}{\partial t}(\rho Y_k) + \nabla(\rho Y_k \mathbf{v}) = \nabla(\rho Y_k \mathbf{V}_k) + \dot{\Omega}_k \qquad k = 1, \ldots, NC \tag{3.3}$$

$$\rho C_P \frac{\partial T}{\partial t} + \rho C_P \mathbf{v} \nabla T = -\nabla \mathbf{q} - \rho \sum_{k=1}^{NC} C_{P,k} Y_k \mathbf{V}_k - \sum_{k=1}^{NC} h_k \dot{\Omega}_k \tag{3.4}$$

where t is the time, ρ is the mixture density, p the pressure, $\mathbf{v}$ the mixture velocity vector, τ the fluid stress tensor, $\mathbf{g}$ the acceleration vector due to gravity, Y_k the mass fraction of species k, $\mathbf{V}_k$ is the diffusion velocity of species k, $\dot{\Omega}_k$ the formation rate of species k, T the temperature, C_P and $C_{P,k}$ are the specific heat at constant pressure of the mixture and of the individual species k, respectively, $\mathbf{q}$ the heat flux vector and h_k the individual species enthalpy.

The density of the mixture is calculated through the ideal gas equation of state, while the heat flux vector, which includes conduction and radiation, is calculated as

following:

$$\mathbf{q} = -\lambda \nabla T + \mathbf{q}_{\text{rad}} \tag{3.5}$$

where λ is the mixture thermal conductivity and $\mathbf{q}_{\text{rad}}$ is the radiative heat flux. The diffusion velocities of species k are calculated, considering both Fick's law and thermal diffusion (also known as Soret effect):

$$\mathbf{V}_k = -\frac{D_k}{Y_k}\nabla Y_k - \frac{D_k \Theta_k}{X_k}\frac{1}{T}\nabla T \tag{3.6}$$

where X_k is the mole fraction and Θ_k the thermal diffusion ratio of species k and D_k is the individual-species mixture-averaged diffusion coefficient, which is related to the binary diffusion coefficients Γ_{jk} through the expression:

$$D_k = \frac{1 - Y_k}{\sum_{j \neq k}^{NC} \frac{X_k}{\Gamma_{jk}}} \tag{3.7}$$

The approach proposed by Coffee and Heimerl [49] was adopted here to enforce the mass conservation, which consists of replacing $\mathbf{V}_k$ in Equations (3.3) and (3.4), for a correction diffusion velocity, $\mathbf{V}_k^{\text{C}}$, defined as:

$$\mathbf{V}_k^{\text{C}} = \mathbf{V}_k + \mathbf{V}_{\text{C}} \tag{3.8}$$

where V_{C} is a constant corrector factor that is species-independent, although varies in space and time. It is used to satisfy the mass conservation and is calculated through:

$$\mathbf{V}_{\text{C}} = -\sum_{k=1}^{NC} Y_k \mathbf{V}_k \tag{3.9}$$

The radiative heat transfer was modelled by assuming the optically thin radiation hypothesis, in which self-absorption of radiation is neglected. It was only taken into account the following significant radiating species - H_2O, CO, CO_2, CH_4. The radiative heat transfer contribution in the energy equation is described as:

$$\nabla \mathbf{q}_{\text{rad}} = -4\sigma a_{\text{P}}(T^4 - T_{\text{env}}^4) \tag{3.10}$$

where T_{env} is the environment temperature and σ is the Stefan-Boltzmann constant. The Planck mean absorption coefficient, a_{P}, is defined here as:

$$a_{\text{P}} = p_{\text{H}_2\text{O}} a_{p,\text{H}_2\text{O}} + p_{\text{CO}_2} a_{p,\text{CO}_2} + p_{\text{CO}} a_{p,\text{CO}} + p_{\text{CH}_4} a_{p,\text{CH}_4} \tag{3.11}$$

where p_k is the partial pressure of species k. The extinction coefficient $a_{p,k}$ of species k is estimated according to RADCAL software [50].

3.2 Numerical modelling

The developed solver (defined in Section 4.1) *laminarSMOKE* by Cuoci et al [47][48] solves the previous presented equations, and it was derived from the pisoFoam solver for unsteady, compressible, non-reacting flows, available in the standard OpenFOAM solver collection.

The conventional CFD methods based on segregated algorithms are usually not suitable to solve reacting flows with detailed kinetics due to its high stiffness and substantial nonlinearities that characterize the transport equations of species and energy. On the other hand, coupled algorithms already present several advantages for the solution of stiff, large systems of nonlinear equations, where the two main known approaches are fully coupled and operator-splitting methods. The problem about adopting fully coupled methods is that, especially in presence of cases with detailed kinetics, as the ones considered in this study, the number of coupled equations to be solved are very large, and the computational resources required can become rapidly prohibitive. And it becomes even worse when high-order approximations to the spatial derivatives are used.

So, in order to solve the governing equations, the operator-splitting method is adopted, because this is the one that faces effectively the reacting, stiff processes associated with detailed kinetics. The idea behind the operator-splitting technique is very simple and consists of splitting the governing equations into several subequations. In the presented case, the transport and reaction terms will be properly separated in the equations of energy and species. In particular, it is also very convenient to separate the convective and diffusive transport terms (nonstiff processes) from the chemical reaction terms (stiff processes), once it helps to avoid or reducing some expensive matrix operations, typical of fully coupled algorithms.

The operator-splitting method implemented in the *laminarSMOKE* solver will be briefly presented. The method of lines (MOL) was considered, meaning that after the spatial discretisation, the transport equations of species and energy are rewritten in following form:

$$\frac{\mathrm{d}\psi}{\mathrm{d}t} = \mathbf{C}(\psi, t) + \mathbf{D}(\psi, t) + \mathbf{R}(\psi) \tag{3.12}$$

where ψ is the vector of mass fractions and temperature (i.e., the primary variables), $\mathbf{C}(\psi, t)$ and $\mathbf{D}(\psi, t)$ are the vectors of rates of change of ψ due to the transport (i.e., convection and diffusion, respectively), and $\mathbf{R}(\psi)$ is the vector of rates of change of ψ due to chemical reactions. The numerical solution of Equation (3.12) is obtained by discretising the time in increments Δt and getting closer to the solution on each of these time steps. Each of the terms on the right-hand side of Equation (3.12) contributes some amount to the overall change in ψ during the numerical time step.

Because this study is in the presence of complex kinetics mechanisms, the stiff operator (due to the chemistry) has to be the last in the splitting process in order to ensure stability and accuracy. Keeping this in mind, the Strang splitting scheme [51] was adopted, to group together the convection and diffusion terms and separate them from the stiff chemical reaction term. The numerical integration is then performed in three substeps.

Substep 1. Firstly, the reaction term is integrated over the time step $\Delta t/2$ by solving the following stiff ordinary differential equation (ODE):

$$\frac{\mathrm{d}\psi^a}{\mathrm{d}t} = \mathbf{R}(\psi^a) \tag{3.13}$$

where the initial condition $\psi^a(0)$ corresponds to the final state from the previous time step, and the solution of Equation (3.13) is denoted as $\psi^a(\Delta t/2)$.

Substep 2. The convection and diffusion terms are integrated along the whole time step Δt by solving the following (ODE) system:

$$\frac{\mathrm{d}\psi^b}{\mathrm{d}t} = \mathbf{C}(\psi^b, t) + \mathbf{D}(\psi^b, t) \tag{3.14}$$

where the initial condition $\psi^b(0)$ is equal to the final state of the system from substep 1, $\psi^a(\Delta t/2)$, and the solution of Equation (3.14) is denoted as $\psi^b(\Delta t)$.

Substep 3. This last step is identical to the substep 1, with the exception that the initial condition corresponds to the final state of the system from substep 2, $\psi^b(\Delta t)$. The solution is then used as the initial condition of substep 1 of the following time step.

Substeps 1 and 3 (the reaction steps) have no spatial dependence, therefore do not require boundary conditions. However, the transport operators $\mathbf{C}(\psi, t)$ and $\mathbf{D}(\psi, t)$ do have spatial dependence, and need the specification of appropriate boundary conditions, as it will be mentioned in Section 4.3.2. Through implementation of several numerical methods, these equations are possible to be solved [47][48].

Only the species and energy equations are solved through the Strang splitting algorithm. Since the continuity and momentum equations are solved based on a segregated method, in order to ensure the mass conservation at each time step, pressure implicit with splitting of operators (PISO) algorithm [52] is applied. The time step is automatically adjusted during the calculations to have always a sufficiently small maximum Courant number, this way avoiding stability issues. Figure 3.1 shows the whole numerical algorithm structure adopted in the *laminarSMOKE* code.

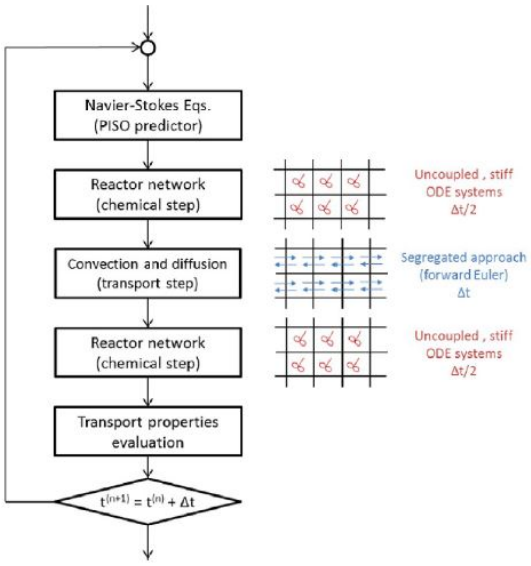

Figure 3.1: Numerical algorithm adopted in the laminarSMOKE code [48].

3.3 Kinetic mechanisms

Combustion phenomena cannot be simply described by its stoichiometric chemical reaction as presented in Section 2.1.1. In fact, multiple species are produced due to recombination and interaction between radicals and stable species throughout the process.

Therefore, in order to solve the aforementioned governing equations, all species involved in the chemical reaction, along with their thermophysical properties, have to be properly identified and available for the calculations.

Politecnico di Milano, specifically the CRECK Modelling Group, developed several detailed kinetic mechanisms, attempting to describe extensively these chemical reactions. They validated the proposed mechanisms in [53][54]. In the present study, hydrogen flames were simulated with the *POLIMI_H2CO_1412* mechanism, consisting of 14 species and 33 reactions, while methane flames used the *POLIMI_C1 C3HT_1412* (84 species and 1698 reactions). For the simulations regarding porous inert media influence on the pollutants emissions, it was used the *POLIMI_H2CO_ NOX_1412*, consisting of 32 species and 173 reactions. The chemical reactions involved in the H_2 kinetic mechanisms are presented in appendixes A.1 and A.2, respectively. But they are not shown for CH_4 case [55], since its kinetic mechanism is too long.

3.4 Final remarks

Two slightly different codes of *laminarSMOKE* for different applications were actually designed by the CRECK Modelling Group and used throughout this thesis: *laminarSimpleSMOKE* and *laminarPimpleSMOKE*. *laminarPimpleSMOKE* was developed to simulate transient flows, being able to impose desired time steps as long as it does not make the Courant number to exceed its maximum value. *laminarSimpleSMOKE* was developed to reach steady-state conditions very fast and (normally) does not contain any time derivation and therefore no time information.

Chapter 4

Software description

4.1 Introduction

The numerical simulations that will be presented in this study were conducted on the Open Source Field Operation and Manipulation (OpenFOAM), the most used open-source tool for Computational Fluid Dynamics worldwide, across most areas of engineering and science, both commercial and academically. It is based on a C++ library, used to create executables, so called applications, and these can be divided into two categories: solvers and utilities. The solvers are developed to solve numerically a specific problem in continuum mechanics, while the utilities are designed to perform certain tasks involving data manipulation.

OpenFOAM is designed as an easily extendible package of functions for numerical solutions, based on Finite Volume Method. OpenFOAM not only provides a wide range of features to solve complex fluids flow involving turbulence, chemical reactions, heat transfer and more, but also allows the users to manipulate the existing features like solvers and utilities as better suits them for specific studies.

In the following subchapters, it will be presented some of the main features used to manipulate in order to run simulations in this study, and other important aspects of the software that the user should be aware of, as explained in OpenFOAM User Guide [56].

4.2 File structure

To execute a simulation in OpenFOAM, the required data to run a simulation case, has to be set up and organized into three specific subdirectories, each of them containing several files. Those are:

- *constant*, where not only the fixed parameters along the simulation are set up such as physical properties, but also contains the description of the case mesh in the subdirectory *polyMesh*.

- *system*, where the user sets the parameters related with the procedure of the simulation. This directory has to contain at least three files: *controlDict*, where the user can define the starting/ending time and time steps of calculations;

fvSchemes and *fvSolution*, where discretization schemes and equation solvers are set, respectively. In addition, the use of *decomposeParDict* can allow the user dividing all fields that will be calculated by taking advantage of the parallel processing, saving computational time.

- First time instant considered in the simulation (frequently *0*), containing all individual files of particular fields, such as initial and boundary conditions that are imposed by the user. In the presented study, typical fields are the velocity, temperature, molecule concentration of all species involved, etc.

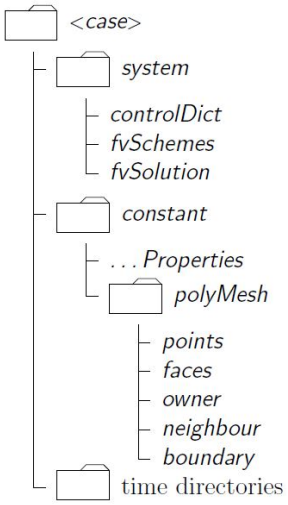

Figure 4.1: Case directory structure [56].

While the simulation is running, the fields for predefined time instants are being calculated, and as soon as each time instant is calculated, a new subdirectory, named with that specific time instant, is created automatically in the same level as the three previous present subdirectories. Each of these time instant subdirectories will be composed of individual files describing the same variables that composed the first time instant considered for the simulation, and other additional specific requested fields, like reaction product species for example.

4.3 Pre-processing

4.3.1 Mesh generation

As mentioned previously, OpenFOAM numerical solutions are based on the Finite Volume Method, which requires the decomposition of the physical domain into a discrete mesh.

To generate a mesh, the user has to, whether create a *blockMeshDict* file from scratch, or manipulate other file from a different case, in the subdirectory *constant/polyMesh*. This file is composed by the geometry description of the mesh. Firstly, the user has to point out all existing vertices using Cartesian coordinates and each vertex will have a label associated to it. Then, the blocks, constituted by

eight vertices each, are formed in the shape of a hexahedron, as presented in Figure 4.2.

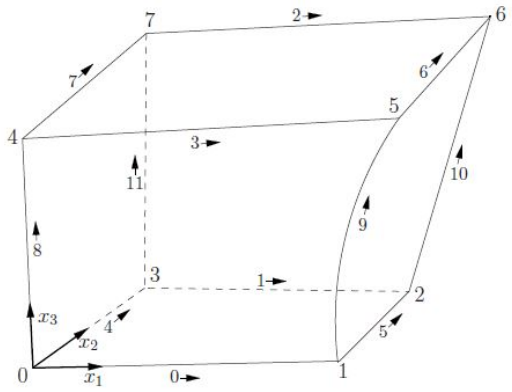

Figure 4.2: Single block of a mesh [56].

Each block of the geometry is constituted by a number of cells specified by the user, having in mind that the more cells specified, which means the more refined mesh imposed, the more processing time the software will take to conclude the simulation. Each block can also have a cell expansion ratio, which enables the cells to expand gradually relatively the previous one, in a specified direction. Each edge of a block is assumed to be straight by default, however, if desired, it is possible to specify a curved edge.

Once all blocks of the geometry are properly defined, all of their outer faces that represent the boundaries of the mesh, will have to be set up. The next section will approach the main issues on the boundary conditions.

Additionally to the *blockMesh* utility, OpenFOAM also provides the *snappyHexMesh* utility. This last one, more than a mesh generator, is more of mesh sculptor, requiring an already existing base mesh to work with. Depending on the intentions of the user, several options are given in the *snappyHexMeshDict* file in *system* folder: (1) refine the mesh; (2) adjust to fit onto provided geometries; (3) add boundary layers near the requested patches. Figure 4.3 presents an example of the use of *snappyHexMesh* utility, where features (1) and (2) are performed.

4.3.2 Boundary counditions

The boundaries, as well as the initial conditions, have to be set up in order to close the equations system governing the flow and to start the simulation.

The boundaries are divided into patches (regions), where each patch has a keyword associated to it, which describes the interaction with the fictitious exterior of the domain, so called boundary types. The name addressed to each patch is later on used for setting initial conditions and respective boundaries of the field data files in the first time instant considered in the simulation.

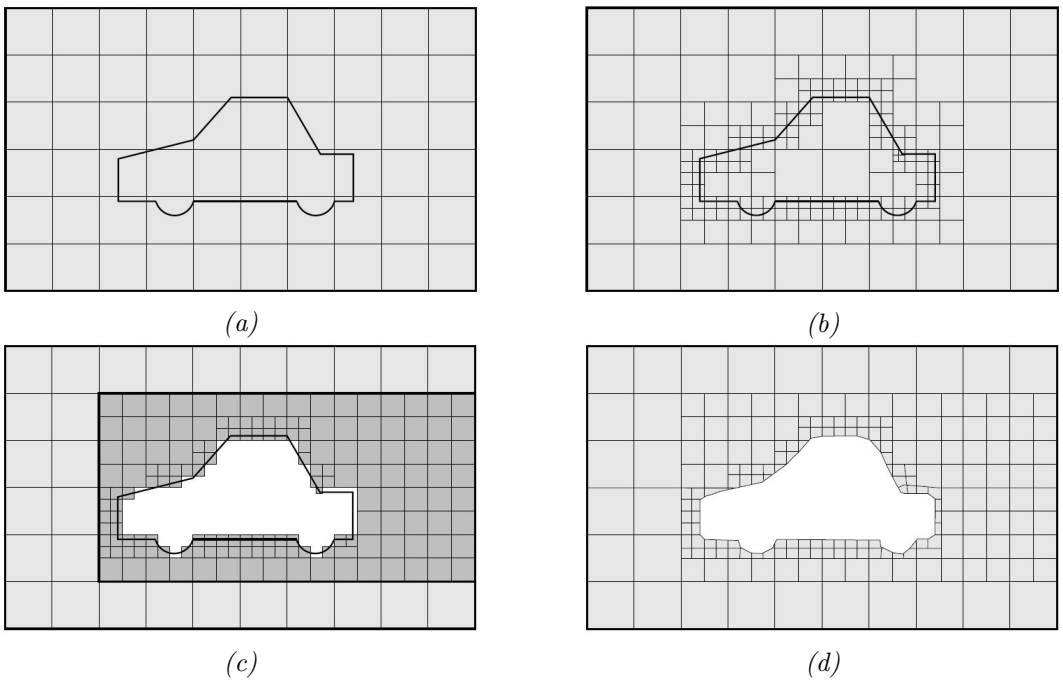

Figure 4.3: Example of the use snappyHexMesh utility: a) creation of the background mesh, b) cell splitting by surface, c) cell splitting by region and cell removal, d) final surface snapping [56].

The main boundary conditions (BC) provided by OpenFOAM used in the present study are:

- *fixedValue*, which is used to impose a fixed value of the function throughout the patch (surface) for all time instants of the simulation. This is also known as the Dirichlet BC.

- *fixedGradient*, that imposes a fixed gradient throughout the patch also for all time instants. In case the imposed gradient is zero, *zeroGradient* can be simply applied. This BC is often called as Neumann BC.

- Robin BC, that combines both Dirichlet and Neumann conditions.

The thermal boundary conditions, if applied to the previous presented cases, are exampled in Figure 4.4, and take the following form:

- Dirichlet, on a surface S_1:

$$T = f_1 \tag{4.1}$$

- Neumann, on surface S_2:

$$q = f_2 \tag{4.2}$$

- Robin, on surface S_3:

$$q = h(T - T_a) \tag{4.3}$$

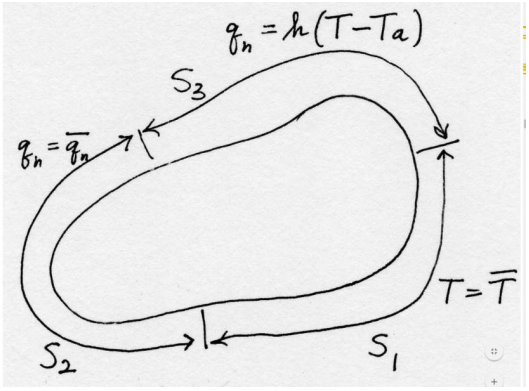

Figure 4.4: Example of different boundary conditions applied on a surface [57].

Furthermore, and since OpenFOAM does not allow the imposition of an expression or function, whether for *fixedValue* or *fixedGradient* boundary conditions, it was developed a tool called *swak4Foam*, which stands for swiss army knife for FOAM. This tool offers the user the possibility of specifying expressions involving the fields and evaluating them. Further information on this tool can be found in *swak4Foam* user guide [58].

4.3.3 Discretisation and solution of equations

As mentioned in Chapter 3, the flows present in this study are described by a number of partial differential equations depending on time and spatial dimensions. Since these variables are continuous, they go through an approximation transformation into discrete variables, process known as discretisation. In CFD analysis, those variables have to be discretised in order to be able to be solved numerically. As the variables are discretised, there is always some amount of error inherent to the process, so the numerical methods implemented should reduce these errors to a negligible level.

The specification of the Finite Volume discretisation schemes to solve the partial differential equations are set in the *fvSchemes* dictionary located in the *system* directory. Relatively the solution of the equations, tolerances and algorithm controls, these are set in *fvSolution* dictionary, also located in the *system* directory. The ordinary differential equations associated to the kinetic mechanisms are solved through OpenSMOKE framework.

4.3.4 Simulation control

The execution of a solver follows certain parameters that are set in the *controlDict* file in the subdirectory *system*. In this file is specified the starting and ending time of the simulation, the time step between calculations, the time intervals the software records the existing fields values and their respective precision.

Note that in order to achieve numerical stability and temporal accuracy in every cell, Courant number (Co) must be always less than 1. The Courant number

is defined as:

$$\mathrm{Co} = \frac{\delta t \mid U \mid}{\delta x} \tag{4.4}$$

where δt is the time step, $\mid U \mid$ is the magnitude of the velocity through the referred cell and δx is the cell size in the direction of the velocity. Because it must ensure Co < 1 everywhere, it is common to determine δt based on the worst case scenario of the combined effect of the larger flow velocity and smaller cell size. It is possible to run simulations on an adjustable time step mode, where a new time step is calculated for each time instant, where the maximum Courant number in the mesh cannot exceed an imposed maximum value.

4.3.5 Flame ignition in combustion studies

As mentioned in Section 2.1.3, combustion can be ignited either by supplying an exterior heat source to a small fraction of the mixture, or if the mixture temperature is higher or equal to the autoignition temperature.

In this thesis, both diffusion and premixed flames will be an object of numerical studies. In the diffusion cases, a spark will be imposed in the domain region where is most likely the fuel and oxidizer to first meet, in order to ignite the mixture. The spark is set, either *on* or *off*, in *solverOptions* file located in *constant* folder. In this file, the position, the starting time and duration, the temperature and the diameter of the spark are set. Generally, the spark temperature imposed was 2050 K with a diameter around 0.3 mm and duration of about 3 milliseconds.

However, in the premixed cases, the mixture will be ignited by simply setting the internal field temperature of the domain equal to or higher than its autoignition temperature.

4.4 Running a simulation

After the user is done with pre-processing and setting up the case, typing which solver is intended to be used, will run the simulation. OpenFOAM applications can either run the simulation as a foreground or as a background process. As a foreground process, the progress of a simulation will be written in the terminal window, telling the user the current time, maximum Courant number, initial and final residuals for all fields. As a background process, the user can request these information to be saved in a file, while using the terminal window for other tasks.

As mentioned before, a more refined mesh can increase significantly the running time of a simulation. To shorten the processing time, the user can decide to run a simulation by splitting its geometry by several processors connected with each other. These parameters, in case needed, should be defined in the pre-processing phase, in the *decomposeParDict* file, in the subdirectory *system*.

4.5 Post-processing

The main post-processing tool supplied with OpenFOAM is the utility *paraFoam* that uses ParaView [59], an open source visualization application. Among several convenient features, its intuitive interface allows the user to see interactively all individual fields in all time instants calculated throughout the simulation. ParaView can also show the computational mesh before running the simulation.

4.6 Final remarks

Once the simulations taking place here involve very complex calculations and iterations, they require a lof of computational power, that cannot be simply held in a standard computer if it is intended to obtain various results in a short period of time (in this work, approximately four months). As if it was not enough, there will be a need to run these complex simulations in parallel, emphasizing the need of proper computational resources capable to do so. Therefore, FEUP provided access to High Performance Computing (HPC) resources, a research tool used to solve complex problems such like these, that is organized in a cluster of machines. These machines are based on the same technology used in a normal desktop or laptop computers, but have more powerful CPU's, more RAM and a faster network than normally find in a consumer level machine.

The used cluster was *Avalanche*, at FEUP, has 29 nodes, each with 16 cores and between 64 GB and 128 GB of RAM. Each node is connected via a 40 Gbps InfiniBand network. There is 10 TB of central storage, with each node having 500 GB of local storage. The clusters run version 6 of the Scientific Linux operating system.

Chapter 5

Validation of gas-phase model

This chapter has the main purpose of validating the numerical model presented in Chapter 2. Since the discretisation of the transport equations is managed by OpenFOAM platform, the *laminarSMOKE* solver is able to simulate very general reacting flows with detailed kinetics under both steady-state and unsteady conditions on arbitrarily simple and complex geometries (2D and 3D). These chapter does not exploit all the features and capabilities of the solver, since its interest is to validate the numerical methodology. Therefore, the author focused on axisymmetric, laminar flow flames, using both H_2 and CH_4 as fuel, not only because these cases are already well studied and a large amount of accurate experimental data is available to final comparisons, but also because these are precisely the fuels which will be studied in the upcoming chapters.

laminarSMOKE was extensively validated by Cuoci et al [47][48]. Nevertheless, in this thesis it was also performed some validations, since OpenFOAM data structure can be complex to work with in the beginning stages, so it seemed of great importance to start by establishing credibility relatively the obtained results, before going on to the numerical studies. This step was also important to assess the correctness of the installation process.

Each of the following sections will be focused on the validation of one particular numerical investigation: (1) H_2/air and (2) CH_4/air premixed flames in 1D, both validated using *OpenSMOKE* code; (3) diffusion flames fed with a mixture of H_2/N_2, experimentally studied by Toro et al [60]; (4) diffusion CH_4/air flames, experimentally studied by Bennet et al [61].

5.1 1D H_2/air premixed flames

For the validation of H_2/air premixed flames in 1D, the numerical simulations were performed using *OpenSMOKE* code, and afterwards the results are briefly compared with the ones also obtained numerically by Cuoci et al [48].

5.1.1 Simulation setup

In order to check the ability of the kinetic mechanism *POLIMI_H2CO_1412* to correctly describe H_2/air premixed flames, a simulation was run at atmospheric pressure, fed with a mixture with the following mole fractions: $x_{H_2} = 0.1909$, $x_{O_2} = 0.0910$ and $x_{N_2} = 0.7181$. The incoming mixture was at 300 K with an inlet velocity of 57.3 cm/s, whereas the computational domain length was 1.6 cm with a grid composed of 294 points.

5.1.2 Results and discussion

Figure 5.1 shows both the temperature and the OH and HO_2 mole fraction profiles along the axial distance obtained in this work and obtained by Cuoci et al [48]. Note that the curves obtained by Cuoci et al [48], as well as all the other curves obtained from literature, presented merely for comparison were extrapolated directly from its article figures and any instability in the curves was a consequence of the extrapolation process and not a obtained result. According to the Figure 5.1a, that depicts the temperature profile, around 0.8 cm of the domain, the temperature rises rapidly to its peak, 1705 K, and stabilises. The flame position is located in the middle of the computational domain, around 0.5 cm further downstream when compared with the results obtained by Cuoci et al [48]. This happened due to fact that, contrarily to the older version of *OpenSMOKE*, the current version forces the flame to be always centered in the middle of the computational domain. This was preferred in the current version, in order to avoid the flame front being closer to the boundaries, which would give wrong results. Anyway, a shift on the axial direction equal to approximately 0.5 cm was applied to the results obtained by Cuoci et al [48] and then presented in Figure 5.1 to better compare. As it can be seen, the similarities are evident in both profiles.

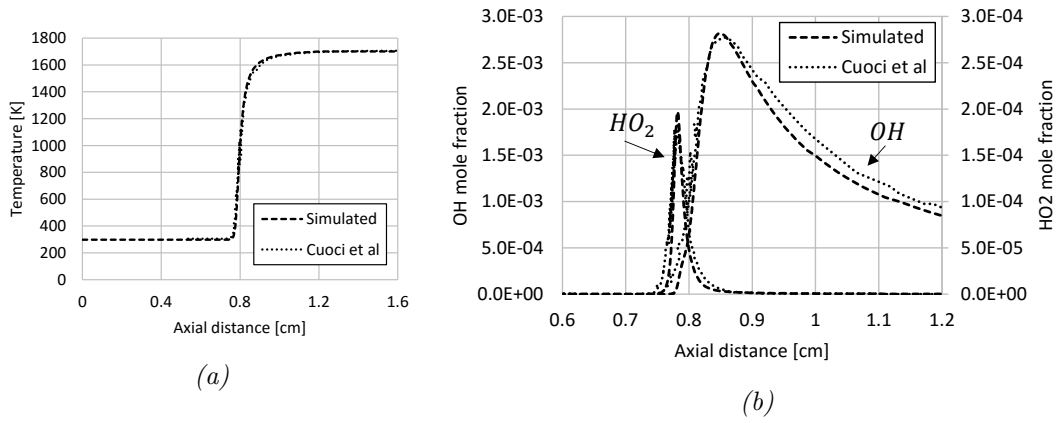

Figure 5.1: Numerical predictions of different profiles in the axial distance: a) temperature, b) OH and HO_2 mole fractions. Comparison between results obtained here and obtained by Cuoci et al [48].

5.2 1D CH_4/air premixed flames

For the validation of CH_4/air premixed flames in 1D, the numerical simulations are also performed using *OpenSMOKE* code, and afterwards the results are compared with those obtained experimentally in [62][63][64][65].

5.2.1 Simulation setup

In order to check the ability of the kinetic mechanism *POLIMI_C1C3HT_1412* to correctly describe the laminar flame speed of CH_4/air at atmospheric pressure, several inlet mixtures with equivalence ratios from 0.65 up to 1.40 were simulated, with the incoming mixture at 298 K and an inlet velocity of 38 cm/s, for a computational domain length of 3 cm.

To evaluate the computational grid dependence on the obtained results, 3 grids with different levels of refinement were used: (1) 134 points; (2) 258 points; (3) 506 points.

5.2.2 Results and discussion

Figure 5.2 shows the comparison between experimental measurements and numerical predictions of the flame speed in function of different equivalence ratios, for steady-state. As it can be seen, the laminar flame speed peak for the 506 points grid is 37.3 cm/s whereas for the 134 points grid is 38.3 cm/s. As expected, the more refined the grid is, the more accurate the numerical predictions will be comparing with the experimental results.

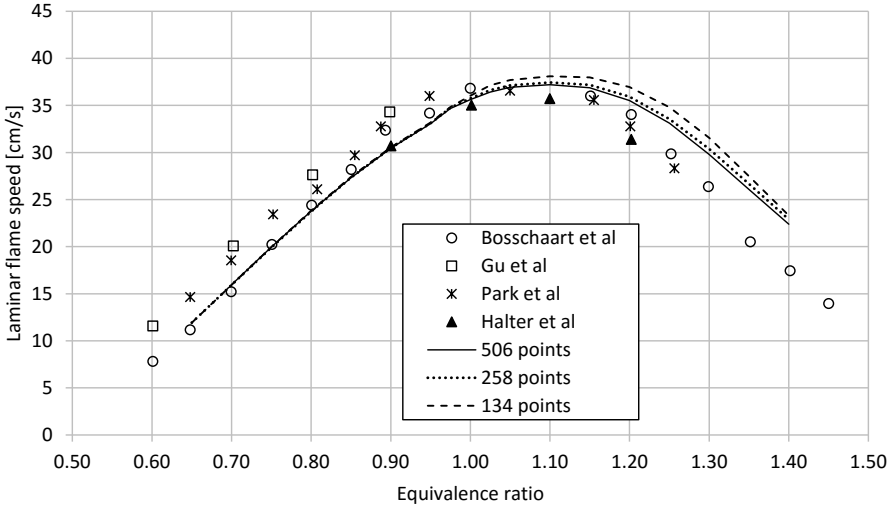

Figure 5.2: Comparison between experimental measurements and numerical predictions of flame speed in function of different equivalence ratios, for steady-state CH_4/air premixed flames. Different refinements of the mesh were used to evaluate its influence. Experimental values obtained by: Bosschaart et al [62], Gu et al [63], Halter et al [64] and Park et al [65].

Figure 5.3 shows both the temperature and the OH mole fraction profile along the axial distance, for different equivalence ratios. As shown in both Figures 5.3a and 5.3b, independently of the equivalence ratio, the flame is always centered in the middle of the computational domain, characteristic of the current *OpenSMOKE* code, as mentioned in the previous section. Furthermore, according to Figure 5.3a, for the lower equivalence ratio, $\phi = 0.70$, the peak temperature is around 1850 K, and as the equivalence ratio is higher, so does the flame temperature until the equivalence ratio is equal to 1 or higher, for which cases the temperature peak is nearly 2200 K. Figure 5.3b shows a very intimate relation between the flame temperature and the OH mole fraction peaks. The higher the flame temperature, the higher OH mole fraction will be. For equivalence ratios equal to 1 or higher, there is not much difference, as it happens for the temperature profile as well.

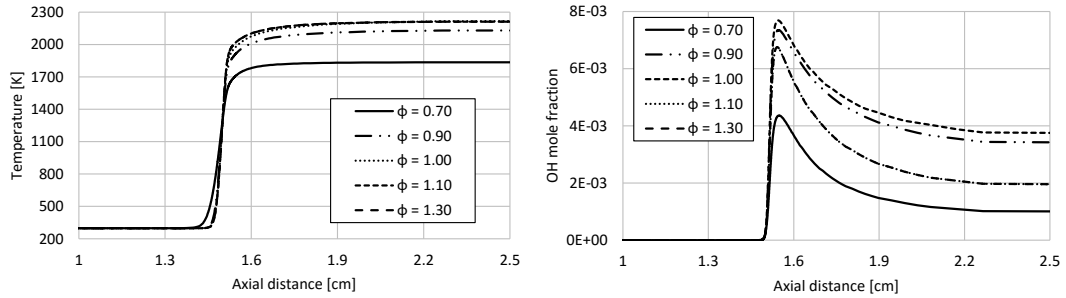

(a) *(b)*

Figure 5.3: Numerical predictions of different profile in axial direction, for different equivalence ratios: a) temperature, b) OH mole fractions.

5.3 H_2/N_2 coflow flames

The coflow flames fed with a mixture of H_2/N_2, experimentally studied by Toro et al [60], constituted a good case for validation of the numerical model due the fact of H_2 chemistry being well known and can be described in relatively small number of species and chemical reactions, saving computational time. As mentioned in Section 3.3, the kinetic mechanism used for H_2 flames was the *POLIMI_H2CO_1412*.

5.3.1 Simulation setup

Figure 5.4a shows a cross-sectional view of the domain in which steady-state combustion takes place using H_2 fuel. The origin is fixed at the center of the fuel inlet plane and x depicts the axial direction of the flow whereas the r represents the radial direction. The nozzle is 10 mm long, has an internal diameter of 9 mm, with a 1 mm width, and is surrounded by an air-coflow annulus, with a diameter of 95 mm. The properties of the flow both inside and outside of the nozzle are calculated, in order to take into account the back diffusion of species into the tube.

The fuel stream is composed by H_2 and N_2, each of them with a mole fraction of 0.5, at ambient temperature and pressure. For this simulation, two different inlet velocities were considered both with a fully developed (FD) velocity profile, with a mean velocity of 27.3 cm/s and 50 cm/s. For each velocity case, two grids with different levels of refinement, containing respectively 1668 and 6672 cells, were tested to better evaluate its influence on the temperature and mass fractions profiles. These validation cases are organised in Table 5.1. The air inlet velocity profile is uniform with magnitude equal to the mean velocity of the fuel inlet velocity profile, for each case.

Table 5.1: Operating conditions for four validation cases

	Case	Grid	Number of cells	Flow speed $[m/s]$
Flame F2	(a.1)	grid 0x	1668	0.27
	(a.2)	grid 1x	6672	
Flame F3	(b.1)	grid 0x	1668	0.50
	(b.2)	grid 1x	6672	

The computational domain is composed by an axisymmetric wedge with 95 mm of internal diameter likewise the experimental set up, and a length of 150 mm. At the axis boundary, the radial velocity is set to zero to simplify the calculations and a zero gradient was attributed to axial velocity, temperature and mass fractions profiles. For the outlet and combustor wall, as well as for the nozzle tube, the boundary conditions were defined by a zero gradient for all previous parameters. A non-slip and slip wall BC is assumed for the nozzle and combustor wall, respectively. The simulations have started with an internal field of the domain at ambient pressure and temperature. Since the flame would be ignited right after the nozzle when contacting with the O_2, it was imposed a finer refinement of the grid in these region to allow a more accurate calculation of flame characteristics. A representation of the computational mesh is shown in Figure 5.4b.

5.3.2 Results and discussion

Figure 5.5 reports the temperature, O_2, H_2O and OH mass fraction field maps for steady-state and the main structure properties of the investigated flames.

Figure 5.6 reports the comparison between the numerical predictions and experimental measurements of the temperature profiles along the centerline, for the two different inlet velocity cases. Furthermore, the continuous line refers to the grid 0x, with 1668 cells, while the dashed line refers to the grid 1x, with 6672 cells. Generally, the agreement between the predictions and measurements are quite satisfactory, especially for cases (b.1) and (b.2), corresponding to Flame F3. It is noticeable that the predictions for the Flame F2 temperature closer to the nozzle are overestimated, which can be happening due to the larger heat transfer from the flame to the nozzle tube that is not being considered numerically, making the temperature more difficult to predict. On the other hand, the numerical results show a very good temperature peak estimation compared with the experiments.

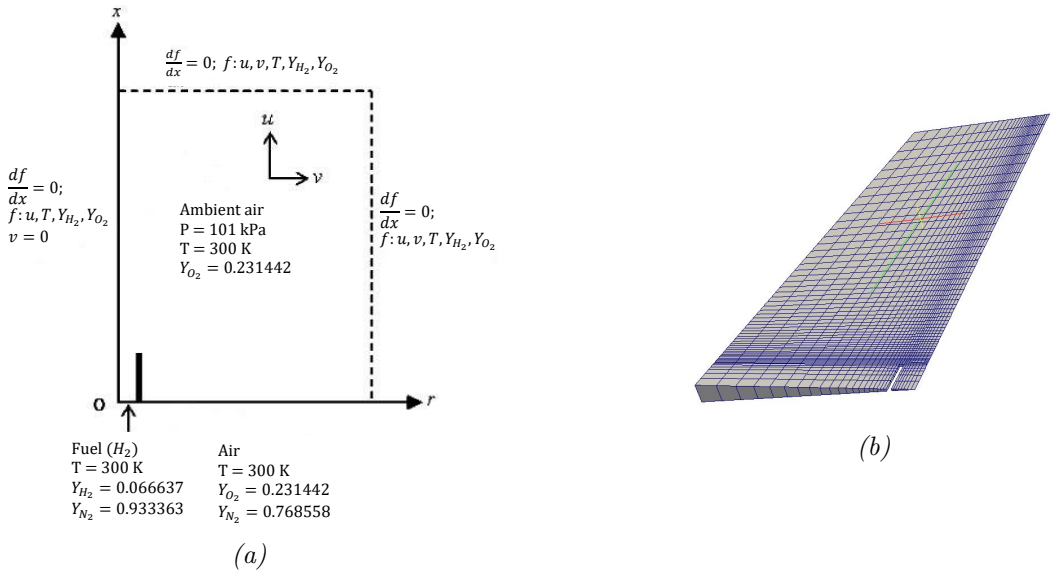

Figure 5.4: a) Schematic ilustration of computational domain coupled with boundary conditions, b) computational mesh, of H_2/N_2 coflow flames. For graphical reasons, it was choosen the representation of grid 0x since is the one with less cells.

Additionally, a comparison between the numerical predictions and experimental results of the species mole fractions in the axial direction along the centerline for the flames F2 and F3, are presented in Figure 5.7a and 5.7b, respectively, both for grids 0x and 1x. The results seem to agree quite well with the experimental ones for both flames. The refinement of the grid does not reflect relevant improvements of the results accuracy in terms of species mole fractions.

The numerical predictions were also compared with the experimental data along the radial direction, here only reported at the axial distance of 10 mm, for the Flame F3 with grid 1x in Figure 5.8. Observing Figure 5.8, the results are in very good agreement with experiment results. The most critical observation to remark could only be the slightly overestimation of O_2 from 7 mm forward, and the underestimation of H_2O in the same region.

As for final remarks, the numerical results for the cases presented here were not difficult to obtain. Particular attention on the location of the spark should be paid, otherwise the flame might not propagate properly and sustain itself. The computational domain was decomposed in four processors to speed up the calculations, taking around 40 CPU hours to obtain the results using the cluster. Pimple code was used with an imposed time step of 10^{-7} s.

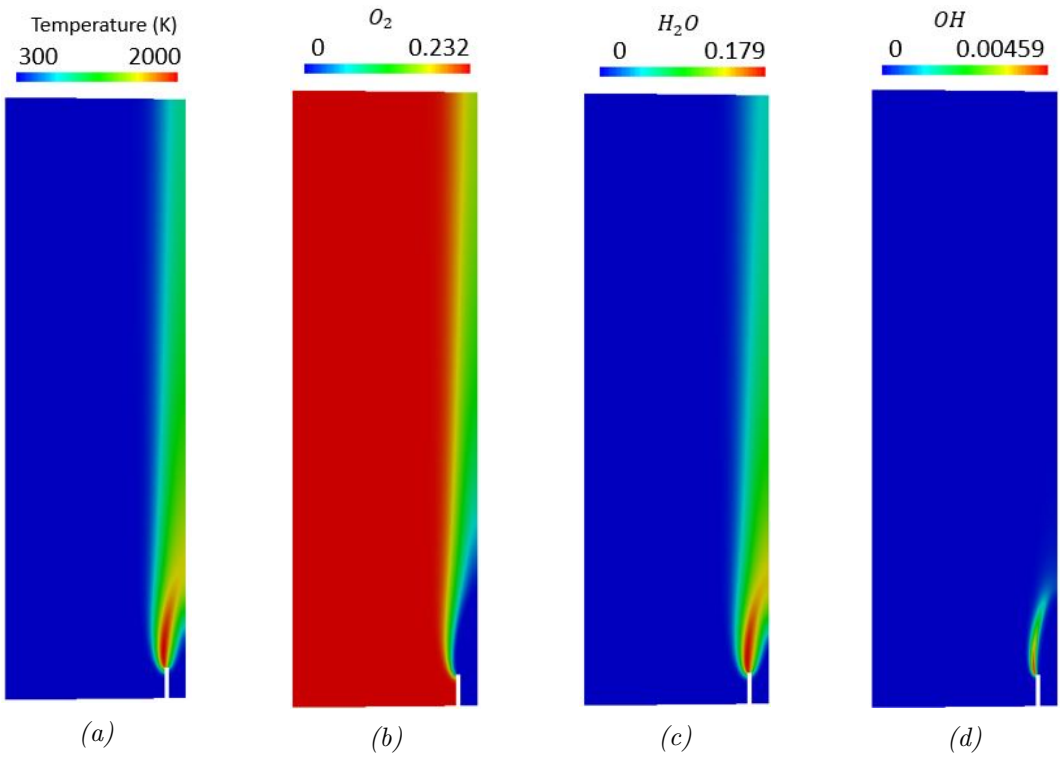

Figure 5.5: Maps of: a) temperature, b) O_2, c) H_2O, d) OH mass fractions, of H_2/N_2 coflow flames.

5.4 CH_4/air coflow flames

The CH_4/air coflow flames experimentally and computationally studied by Bennet el al [61] were also a good case for validation of CH_4 diffusion flames. As mentioned in Section 3.3, the kinetic mechanism used for CH_4 flames was the *POLIMI_C1C3HT_1412*.

5.4.1 Simulation setup

The setup of this simulation is very similar to the H_2/N_2 coflow flames. Figure 5.9a shows a cross-sectional view of the computational domain in which steady-state combustion takes place using CH_4 fuel. The origin is fixed at the center of the fuel inlet plane and x depicts the axial direction of the flow whereas the r represents the radial direction. The fuel stream flows through a 10 mm long nozzle with an inner diameter of 11.1 mm and a width of 0.80 mm, while the surrounding annulus has a diameter of 102 mm. The properties of the flow both inside and outside of the nozzle are calculated, in order to take into account the back diffusion of species into the tube.

The fuel stream is composed by pure CH_4 with a FD velocity profile with a mean velocity equal to 5.67 cm/s while the surrounding flow is composed by regular air with an uniform velocity profile equal to 10.48 cm/s.

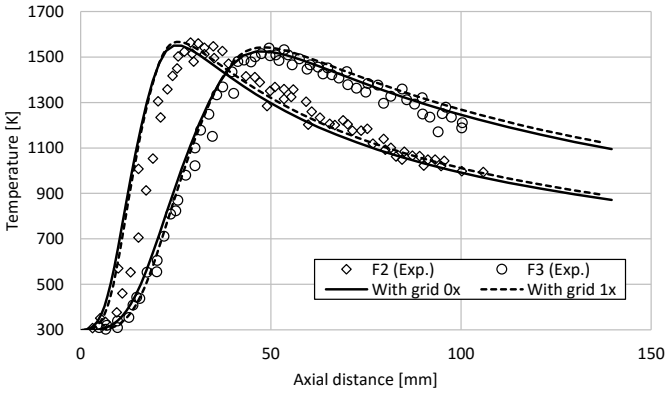

Figure 5.6: Comparison between experimental measurements and numerical predictions of temperature profiles in axial direction of H_2/N_2 coflow flames. Experimental measurements obtained by Toro et al [60].

Both streams enter the domain at ambient temperature, 300 K, and pressure, 101 kPa. The computational domain has a length of 160 mm and the mesh applied to the case was non-equispaced with 7080 cells, and similarly to the H_2/N_2 coflow flames, it was also imposed a finer refinement in the region of ignition and flame stabilisation, immediately after the nozzle. The boundary conditions applied to this case were exactly the same as those applied to the H_2/N_2 coflow flames. A representation of the computational mesh is available in the Figure 5.9b.

5.4.2 Results and discussion

The maps of temperature, OH, H_2O and CO_2 mass fractions and structure properties of the flame are displayed in Figure 5.10.

In Figure 5.11, it is presented the comparison between numerical predictions and experimental results of both temperature profile and main species mole fractions along the centerline. The results of the temperature profile, in Figure 5.11a, are in good agreement with the experimental ones, although the experimentally obtained peak temperature is around 50 K higher than the numerical one. This should be mainly caused by the imposed thermal boundary condition, that neither contemplates the heat loss from the flow to the nozzle tube, nor the consequent pre-heating of the reactants due to the aforementioned heat transport. The difference between the temperature peaks of experimental and numerical results, when compared to the H_2/N_2 coflow flames, is more accentuated in this case because the flow speed and the burning rate of CH_4 are substantially lower than with H_2. Moreover, it can be seen that the height of the numerical flame is around 50 mm, measured by the location of maximum temperature along the centerline, while the experimental one is around 57 mm.

Relatively to the numerically obtained mole fraction profile, as shown in Figures 5.11a-5.11c, it also demonstrates a very good overall agreement with the exper-

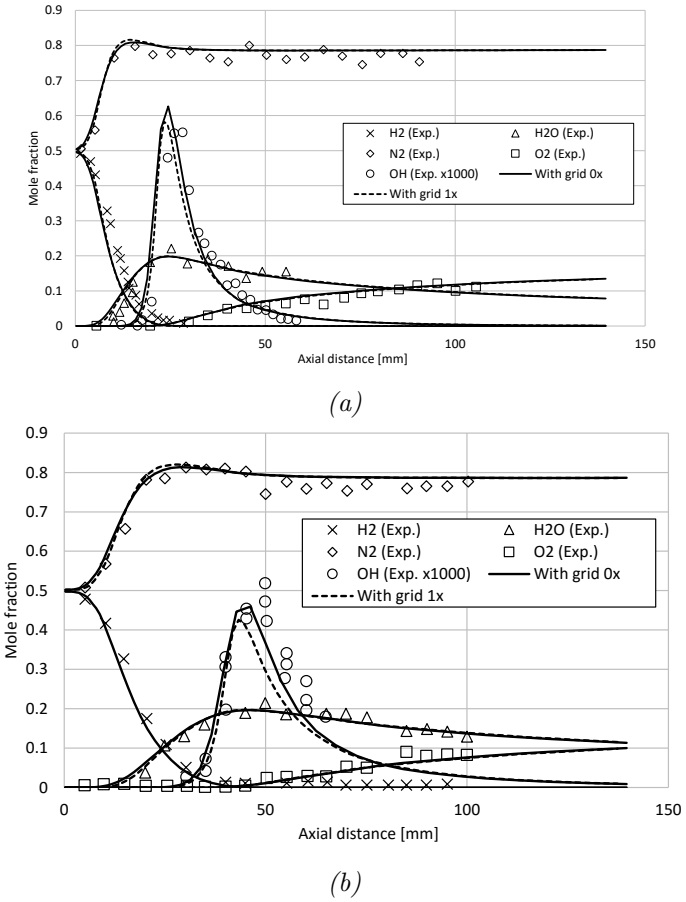

Figure 5.7: Comparison between experimental measurements and numerical predictions of main species mole fractions in axial direction along the centerline of H_2/N_2 coflow flames, a) Flame F2; b) Flame F3. Experimental measurements obtained by Toro et al [60].

imental results. The species mole fractions that deviate more from the experimental values are H_2O and CH_2CO+C_3H_6. Experimentally, these species are particularly difficult to accurately measure as they require way higher precision due to their very low concentrations, so the aforementioned deviation may also come from there.

Finally, it is noted that the computational domain was also decomposed between four processors to save computational time, and took around 120 CPU hours to obtain the results using the cluster. Pimple code was used with an imposed time step of 10^{-8} s. This case took way more time when compared to the H_2 one, not only because of the much lower flame speed, taking more time to reach steady-state, but also due to the fifty times more complex kinetics associated to it.

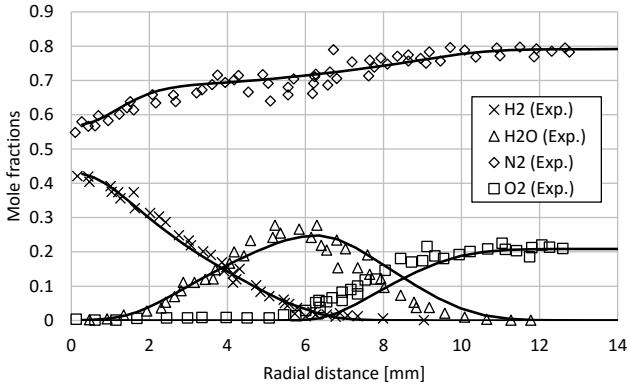

Figure 5.8: Comparison between experimental measurements and numerical predictions of mole fractions in radial direction of H_2/N_2 coflow flames, for Flame F3 at $x = 10mm$. Experimental measurements obtained by Toro et al [60].

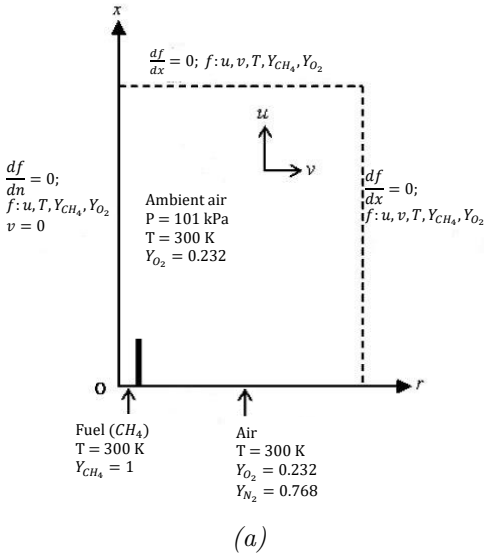

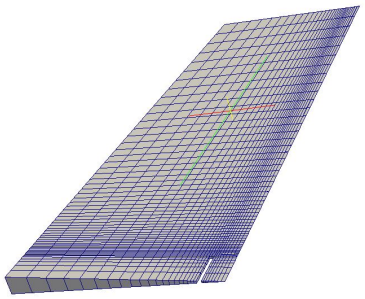

(b)

Figure 5.9: a) Schematic ilustration of computational domain coupled with boundary conditions, b) computational mesh, of CH_4/air coflow flames.

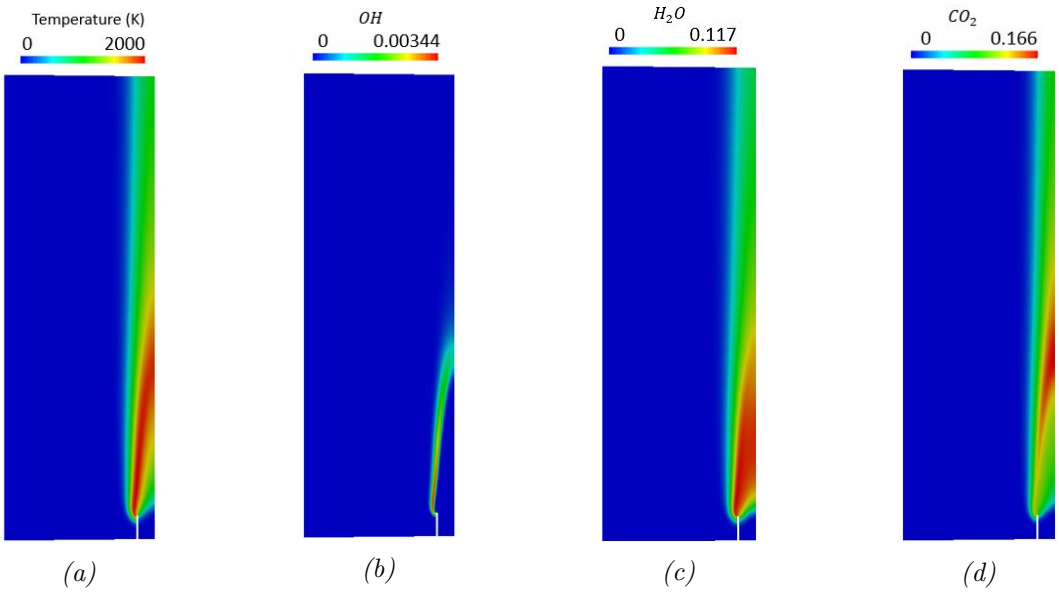

Figure 5.10: Maps of: a) temperature, b) OH, c) H_2O, d) CO_2 mass fractions, of CH_4/air coflow flames.

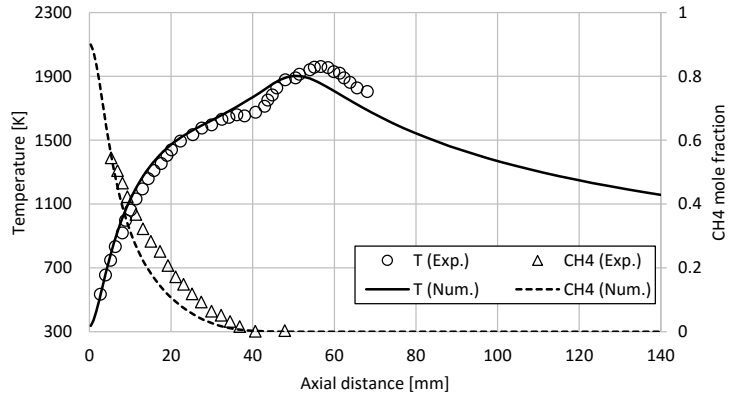

(a)

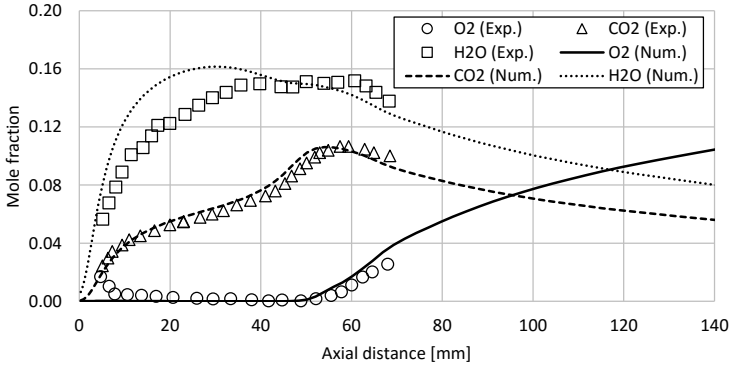

(b)

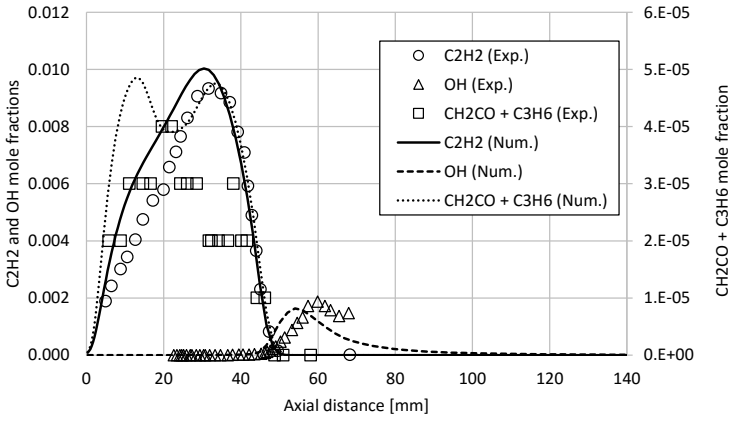

(c)

Figure 5.11: Comparison between experimental measurements and numerical predictions of the temperature profile and main species mole fractions in axial direction along the centerline, of CH_4/air coflow flame. Experimental measurements obtained by Bennet el al [61].

Chapter 6

Numerical studies using gas-phase model

In this chapter several numerical studies on micro-combustion will be presented, using *laminarSMOKE* solver, developed by Politecnico di Milano. Since the physics involved in the flows with diffusion and premixed flames are quite different, these will be divided in different sections. Within them, the different studies will compose different subsections.

6.1 Diffusion flames

6.1.1 Assessment of H_2 micro-jet diffusion flames

In this study, detailed measurements of temperature and major species concentrations were carried out by Cheng et al [34], in laminar micro-jet diffusion flames for different Reynolds numbers. They have also simulated the same cases numerically, using the commercial CFD package CFD-ACE to solve the governing equations, with the input of the molecular transport data from CHEMKIN package.

6.1.1.1 Simulation setup

Table 6.1: Dimensions of the computational domains applied for different Reynolds numbers

	Annulus wall diameter [mm]	Grid resolution	Length [mm]
Re = 330	15	49 x 68	120
Re = 30	20	49 x 74	50

Figure 6.1a shows a cross-sectional view of the experimental setup and computational domain in which steady-state combustion takes place using H_2. The geometry of this study is particularly similar to the H_2/N_2 coflow flames presented in the Section 5.3, but now for micro-scale. The origin is fixed at the center of the inlet plane and x depicts the axial direction of the flow whereas the r represents the radial direction.

The fuel stream comes from a nozzle tube with an inner diameter of 1 mm and a width of 0.17 mm. This nozzle is 10 mm long in the computational domain and it is surrounded by an annulus wall with a variable diameter. The properties of the flow both inside and outside of the nozzle are calculated, in order to take into account the back diffusion of species into the tube. The fuel stream is composed by pure H_2 with a FD velocity profile with two different studied mean velocities: 3.3 m/s and 36 m/s corresponding to a Reynolds number of 30 and 330, respectively, based on the nozzle exit conditions of the fuel. The nozzle introduces the fuel into the quiescent atmospheric air (p = 101 kPa and T = 300 K).

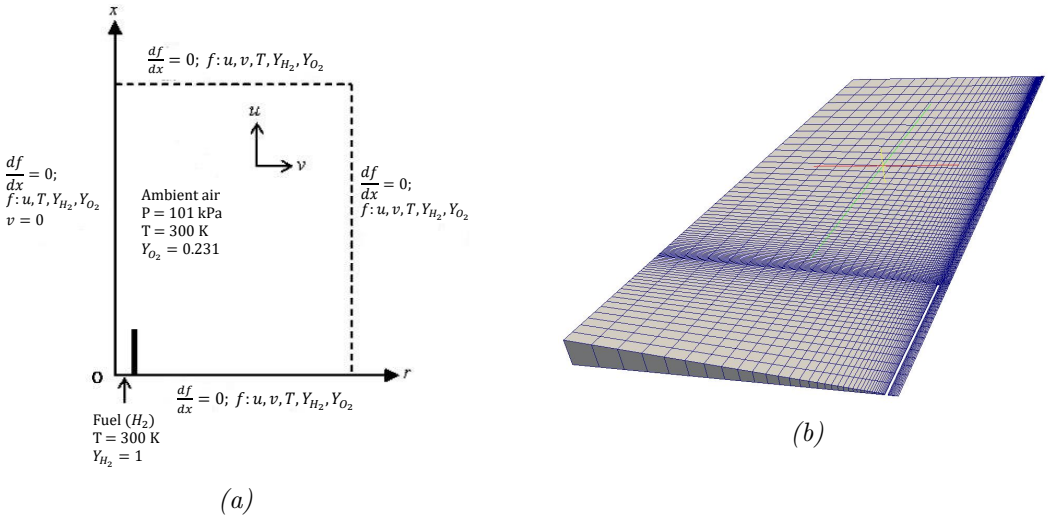

Figure 6.1: a) Schematic ilustration of computational domain coupled with boundary conditions, b) computational mesh, of hydrogen micro-jet diffusion flames.

The computational domain is composed by an axisymmetric and non-uniform staggered-grid. The remaining dimensions, such as the annulus wall diameter and length of the domain, are presented in Table 6.1, as well as the grid resolutions computed for the different Reynolds numbers.

A higher level of refinement is applied around the nozzle exit in both directions, and enlarged cell sizes are set forth forward the outer boundaries. An example of the computational mesh is represented in Figure 6.1b.

Table 6.2: Operating conditions and simulated time (t_{sim}) for five test cases

	Case	Burner wall BC	t_{sim} [s]
Re = 330	(a.1)	Adiabatic	0.05
	(a.2)	Imposed temperature profile A	0.04
Re = 30	(b.1)	Adiabatic	0.05
	(b.2)	Imposed temperature profile B	0.04
	(b.3)	Imposed temperature profile B & Soret Effect neglected	0.04

A non-slip and slip wall BC are assumed for the nozzle and combustor wall,

respectively. At the axis boundary, the radial velocity is set to zero to simplify the calculations. As for the remain boundary conditions, a zero gradient is applied. In order to assess the effect of wall temperature and thermal conduction on the flame structure, and since it is not modelled by the available *laminarSMOKE* solver, different thermal boundary conditions were applied at the wall BC, as presented in Table 6.2. Firstly, in both cases the nozzle tube was assumed to be adiabatic, imposing a zero gradient at these boundaries. Secondly, it was imposed a temperature in the boundary, attempting to make it equal to the experimental value obtained at the top of the nozzle by Cheng et al [34]: for Re = 30, T = 803 K and for Re = 330, T = 703 K. These were the imposed temperatures on the nozzle exit side, whereas on the opposite side T = 300 K was imposed. Naturally, for lower Reynolds numbers the nozzle tube temperature will be higher due to the flame getting closer to its exit. Those exact temperature profiles were obtained by seeing the numerical profiles obtained by Cheng et al [34]. For the Re = 30, a third case was set, with the same imposed temperature profile as the second case, but without accounting for the Soret effect.

6.1.1.2 Results and discussion

Photographs, qualitative LIPF-OH images and computed OH isopleths of the hydrogen jet flames are shown in Figures 6.2 and 6.3.

For the Re = 330, the flame appears as a normal shape of a laminar jet diffusion flame and has a long visible length, in Figure 6.2a. The qualitative single-pulse 2D OH image is shown in Figure 6.2b. As mentioned in Section 2.2.2, OH maximum concentration region can be considered as a sign of the flame position, and the similarities of the shape between the OH imaging and the photograph are evident. Figures 6.2c and 6.2d illustrate the computed OH mass fraction isopleths for the cases (a.1) and (a.2), respectively. For the (a.1) case, the flame is anchored directly in the nozzle, once this wall is defined as adiabatic and the flame is not losing any heat. In the (a.2) case, the flame does not anchor directly in the nozzle but less than a millimetre away. Although the flame structure is different in the case (a.1) when compared with the experiment results, the case (a.2) is already quite similar from a structural point of view.

Reducing the Reynolds number to 30, the visible flame width shortens substantially to a millimetre or two and the flame length to around 3.5 mm. Observing the photograph in Figure 6.3a, it is possible to see an egg shaped flame, and a bright orange color of the nozzle representing a substantial heat loss from the flame to the nozzle. Figure 6.3b shows the single-pulse OH image taken 0.1 mm above the nozzle. The shape of the OH imaging in this case is also quite similar to that one in the photograph. The computed OH mass fraction isopleths for case (b.1) and (b.2) are shown in Figure 6.3c and 6.3d, respectively. The computed OH mass fraction isopleths are not shown because they were very similar and did not contribute much for the discussion. The main difference from the case (b.1) to (b.2) and (b.3) is the same as mentioned above from the case (a.1) to (a.2). Although the flame structure in the case (b.2) is similar to the photograph and single-pulse OH imaging, the

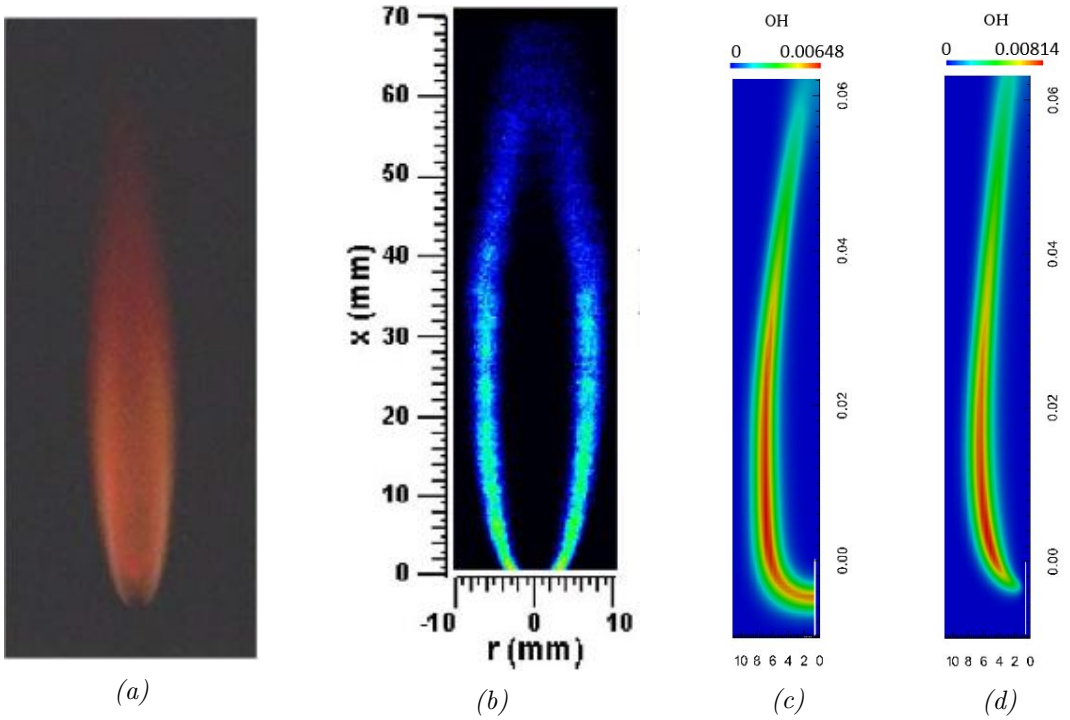

(a) *(b)* *(c)* *(d)*

Figure 6.2: a) Photograph, b) single-pulse LIPF-OH image, c) computed OH isopleths considering the burner wall adiabatic, d) computed OH isopleths imposing estimated real temperature in the burner wall, for hydrogen micro-jet diffusion flames with Re = 330. The axial coordinates in the computed OH isopleths are in metres whereas the radial are in millimetres. Photograph and single-pulse LIPF-OH image obtained by Cheng et al [34].

computed OH concentration peak seems to be in a different region than the one of single-pulse OH imaging - in the computed OH mass fraction isopleths is located in the flame front whereas in the single-pulse OH imaging seems to be located around the nozzle.

Comparisons of the computed and measured temperature and major species mass fractions are made to assess laminar hydrogen diffusion flames. Measurements of temperature and major species mass fractions were made both along the centerline of the flow and in the radial direction for several positions, but here they are only reported for $x = 5$ mm, in the case of Re = 330, and $x = 1$ mm in the case of Re = 30. The experimental data are indicated by different symbols identified in the legend, while the numerical are represented by different types of lines: continuous line are related to the (a.1) and (b.1) cases, dashed lines to the (a.2) and (b.2) cases, and the finer dashed lines to the (b.3) case.

Figures 6.4 and 6.5, respectively, show the comparison between measured and computed axial and radial profiles, of temperature and major species mass fractions, for Re = 330. Figure 6.4a shows that the numerical case (a.2) reproduces relatively well the experimental data, when comparing to the case (a.1), i.e., using adiabatic BC at the nozzle walls. At $x = 66$ mm, the temperature reaches its maximum value, $T = 2011$ K, a bit lower than the experimental maximum $T \approx 2150$ K at $x = 60$

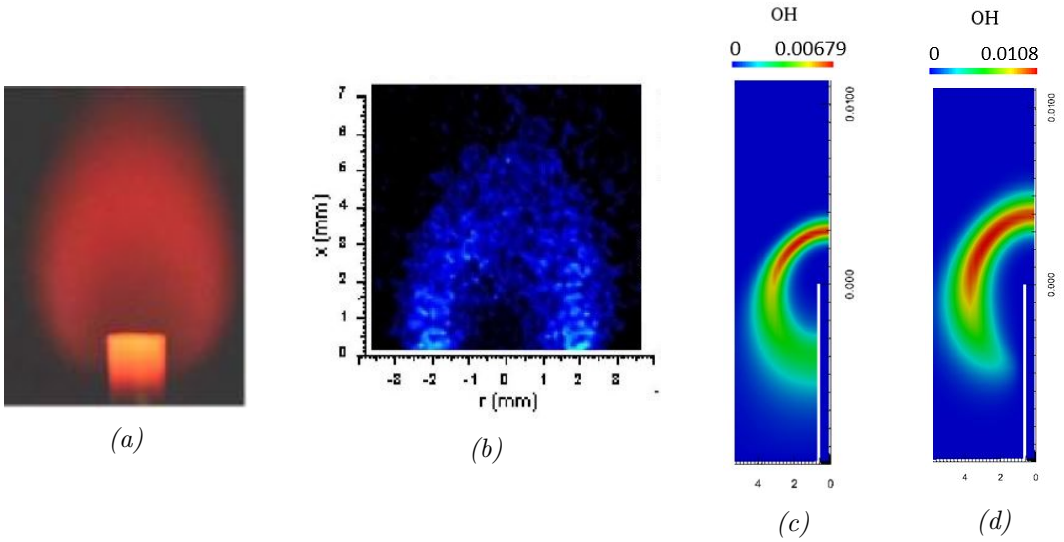

Figure 6.3: a) Photograph, b) single-pulse LIPF-OH image, c) computed OH isopleths considering the burner wall adiabatic, d) computed OH isopleths imposing estimated real temperature in the burner wall, for hydrogen micro-jet diffusion flames with Re = 30. The axial coordinates in the computed OH isopleths are in metres whereas the radial are in millimetres. Photograph and single-pulse LIPF-OH image obtained by Cheng et al [34].

mm. It is possible to see, in the (a.2) case, that the unburned mixture is more preheated than the experimental values, indicating that the imposed temperature to the nozzle BC was too upstream of the flow. On the (a.1), it is possible to see the opposite situation, the unburned mixture is heated more downstream than the previous cases. In the Figure 6.4b, the (a.2) case is closer to the experimental data than (a.1), naturally. The H_2 is totally consumed around 50 mm, which is the location where the experimental maximum water mass fraction is registered.

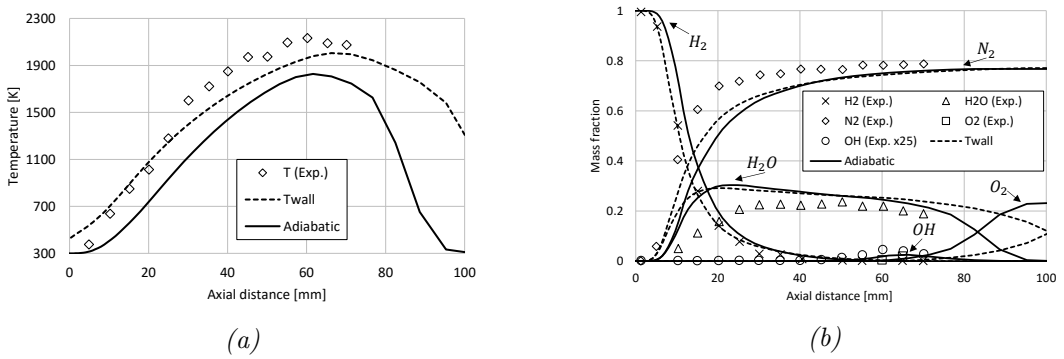

Figure 6.4: Comparison between: a) measured and computed temperature in axial direction along the centerline, b) measured and computed major species mass fractions, for hydrogen micro-jet diffusion flames with Re = 330. Experimental measurements obtained by Cheng et al [34].

Figure 6.5a verifies what was mentioned before, the unburned mixture in (a.2) is preheated earlier than the experimental data. According to (a.2), the flame is

around 3 mm larger than the experimental one, and its temperature peak is over-predicted by around 150 K, when experimentally is nearly 2300 K. For all cases, the temperature raises rapidly from the cool unburned core to around 2300 K. The maximum flame temperature and the OH peak location occurs around the same radial distance, coinciding with the intersection of the H_2O and O_2 mass fraction profiles.

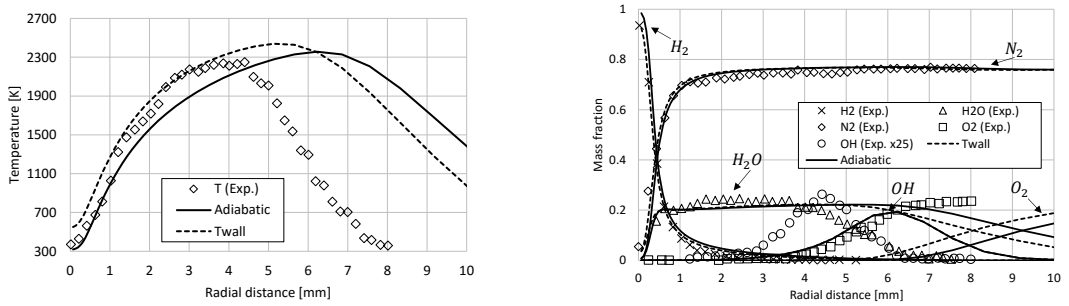

(a) *(b)*

Figure 6.5: Comparison between: a) measured and computed temperature in radial direction, b) measured and computed major species mass fractions, at x = 5 mm, for hydrogen micro-jet diffusion flames with Re = 330. Experimental measurements obtained by Cheng et al [34].

Figures 6.6 and 6.7 show the comparison between measured and computed of axial and radial profiles, respectively, of temperature and major species mass fractions, for Re = 30. In Figure 6.6a, in the axial direction along the centerline, there are not much experimental values to compare with, but it seems that if there were more measured points further downstream, then the cases with imposed temperature profile would be more similar to the experimental values. In Figure 6.7a, it can be seen that all simulated cases resulted in a considerably more wider flame than the one obtained experimentally, even though in the case (b.1) the mixture temperature at the nozzle exit is around 200 K lower than the experimental value, and in the cases (b.2) and (b.3) is nearly 300 K higher.

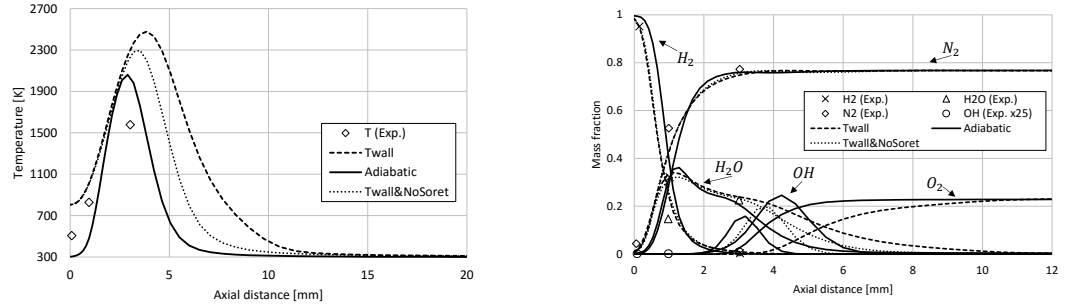

(a) *(b)*

Figure 6.6: Comparison between: a) measured and computed temperature in axial direction along the centerline, b) measured and computed major species mass fractions, for hydrogen micro-jet diffusion flames with Re = 30. Experimental measurements obtained by Cheng et al [34].

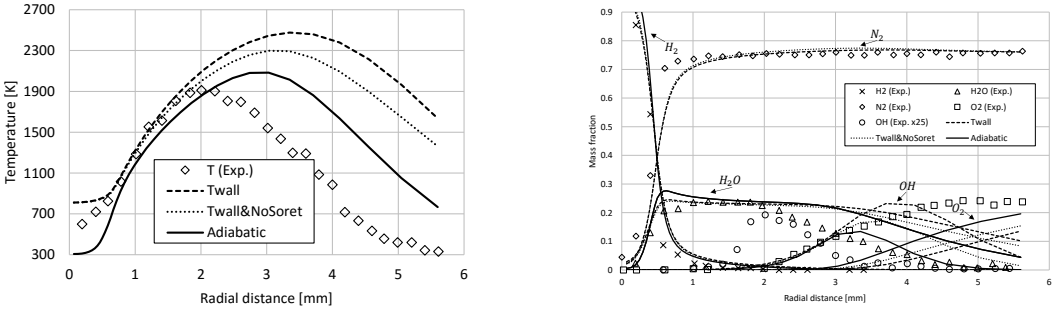

(a) (b)

Figure 6.7: Comparison between: a) measured and computed temperature in radial direction, b) measured and computed major species mass fractions, at $x = 0.1$ mm, for hydrogen micro-jet diffusion flames with $Re = 30$. Experimental measurements obtained by Cheng et al [34].

Should be noted that the numerical simulations for the cases where temperature profiles are imposed, do not reach completely steady-state. Four processors were used to decompose the domains and solve the equations, having taken around 100 CPU hours to obtain the presented results, using the cluster. The imposed time step for all simulations was 10^{-6} seconds using the Pimple code. Although it is possible to see some similarities between the experimental data and the numerical model, the numerical model as it is, is not sufficient to correctly characterise the combustion flow in this micro-jet problem.

6.2 Premixed flames

6.2.1 Investigation on H_2/air premixed flames on a 2D micro-combustor

Rahaghi et al [31] studied numerically the effect on the flame temperature when varying the external convective heat transfer coefficient, inlet mean velocities and micro-combustor heights, on H_2/air premixed flames on a 2D micro-combustor using a home-made transient code.

6.2.1.1 Simulation setup

Figure 6.8a shows a cross-sectional view of the micro-combustor channel - 4 mm long and variable height - where steady-state combustion using premixed H_2/air takes place. The origin is fixed at the center of the inlet plane and x depicts the axial distance while the y represents the normal distance from the centerline of the channel.

The inlet stream is composed by premixed H_2/air with a equivalence ratio equal to 1, at ambient temperature and pressure. For the outlet BC, a zero gradient is applied when it comes to mass fractions, velocity components and temperature. Both top and bottom boundaries are set as walls and therefore a zero gradient is also applied to all previous parameters, except for temperature, which cannot have

a zero gradient if it is intended to simulate the combustor heat loss. Considering the heat flux transversal to the combustor centerline coming from the fluid, across its wall and transferred to the environment, based on the conservation of energy:

$$\lambda_{fluid}\frac{\partial T}{\partial n} = \lambda_{solid}\frac{\partial T}{\partial n} = h(T_{wall} - T_{\infty}) \tag{6.1}$$

Note that the radiation heat flux was not accounted here since it was also neglected by Rahaghi et al [31]. Based on these equalities, the following temperature gradient normal to the combustor centerline and unidirectional, was imposed as thermal boundary condition:

$$\frac{\partial T}{\partial n} = -\frac{h(T_{wall} - T_{\infty})}{\lambda_{fluid}} \tag{6.2}$$

A high temperature, 1500 K, is imposed on the entire computational domain as an initial guess, because it is important to be high enough to make sure the mixture will ignite. No spark was used in this study.

The computational grid for this case is equispaced with a resolution of 16 by 80. The grid is represented in Figure 6.8b.

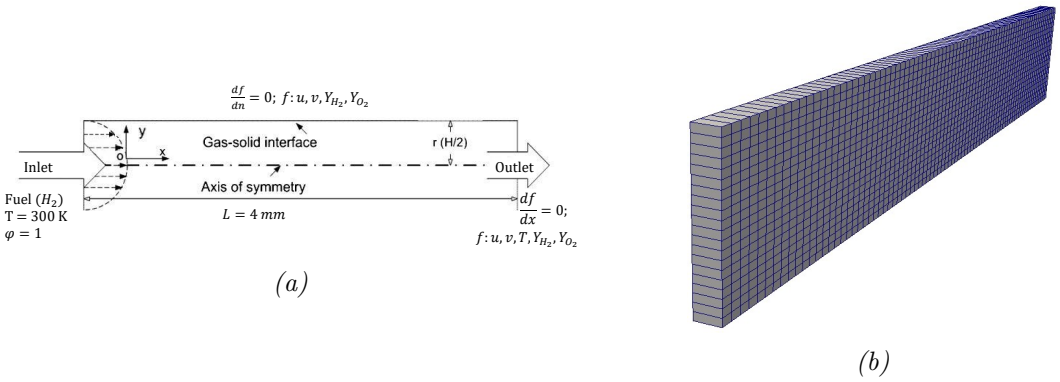

Figure 6.8: a) Schematic ilustration of computational domain coupled with boundary conditions, b) computational mesh, of H_2/air premixed flames in a 2D channel.

The convection heat transfer coefficient will vary among 0, 10 and 20 W/m^{2}K; even though all cases assume a fully developed profile, its mean velocity will vary among 0.3, 0.4 and 0.5 m/s and the micro-combustor height between 0.4 and 0.6 mm, as it is organised in Table 6.3. These variations will allow analysing their effects on the flame temperature, as intended by this study.

Table 6.3: Operating conditions for six test cases

	Case	h $[W/m^2K]$	u $[m/s]$
0.6 by 4 mm channel	(a.1)	10	0.4
	(a.2)	0	0.4
	(a.3)	20	0.4
	(a.4)	10	0.5
	(a.5)	10	0.3
0.4 by 4 mm channel	(b.1)	10	0.4

6.2.1.2 Results and discussion

Figures 6.9a and 6.9b show the temperature and OH mass fraction profiles, respectively, along the centerline of the micro-combustor, for different convective heat transfer coefficients. As expected, it is possible to see that the case that generates higher flame temperature is when $h = 0$ W/m^{2}K, which means considering there is no heat loss and therefore the wall is adiabatic. In this case, the flame temperature gets hotter in the end of the combustor, with a maximum value around 1620 K. The higher the convective heat transfer coefficient, the higher the wall heat losses will be and consequently the lower is the flame temperature inside the combustor. In the three cases, the temperature rapidly rises in the first 0.5 mm of the combustor. This, associated with the fact that the Figure 6.9b shows OH mass fraction maximum values for the previous location, there should be located the flame. Comparing the values obtained here with those obtained by Rahaghi et al [31], it is possible to see that they are relatively lower, which indicates that the used thermal boundary condition does not suit well the case here, which can be expected since it does not account for the wall thickness. However, the results obtained here seem to be quite similar qualitatively, so this is where the attention should be paid.

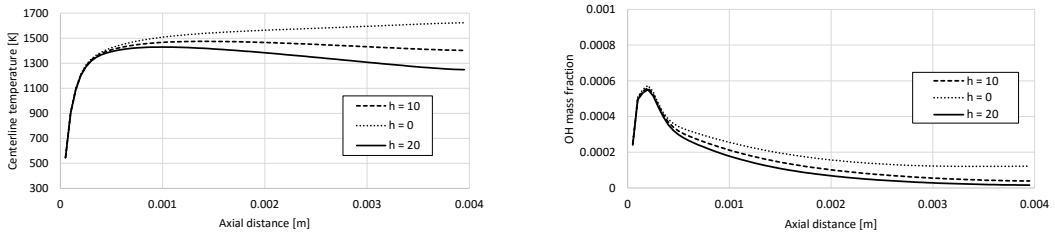

(a) *(b)*

Figure 6.9: Profiles in axial direction along the centerline: a) temperature, b) OH mass fraction, for different convective heat transfer coefficients.

Figure 6.10 depicts the cross-section temperature profile at $x = 0.5$ mm, for the same three convective heat transfer coefficients. It can be seen that the trend of the temperature profile changes drastically with the different convective heat transfer coefficients with the surroundings. At $x = 0.5$ mm, in the adiabatic case, the maximum temperature is located next to the wall while the minimum in the centerline. As the convective heat transfer coefficient increases, the difference between the temperature next to the wall and at the centerline becomes smaller, and eventually

the maximum temperature will be located in the centerline, since next to the wall there is a higher heat loss due to the higher convective heat transfer coefficient.

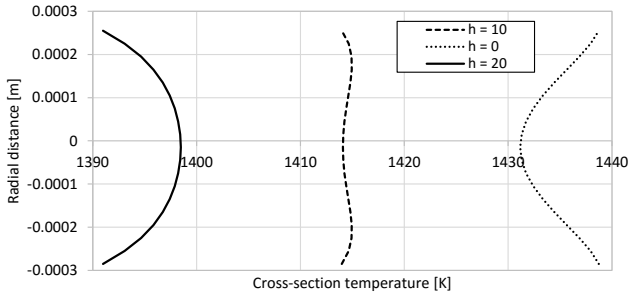

Figure 6.10: Cross-section temperature profile comparison for different convective heat transfer coefficients at $x = 0.5$ mm.

Figure 6.11a and 6.11b show the temperature and OH mass fraction profiles along the centerline, for different inlet mean velocities. Observing the temperature profile, it is seen that the higher is the inlet velocity, the higher will be the flame temperature by 70-80 K. Relatively to the OH mass fraction profile, it can be seen that there is a small trend for the flame to be anchored further downstream with the increase of the inlet mean velocity. The variations of the temperature and OH mass fraction show a proportional behaviour to each other.

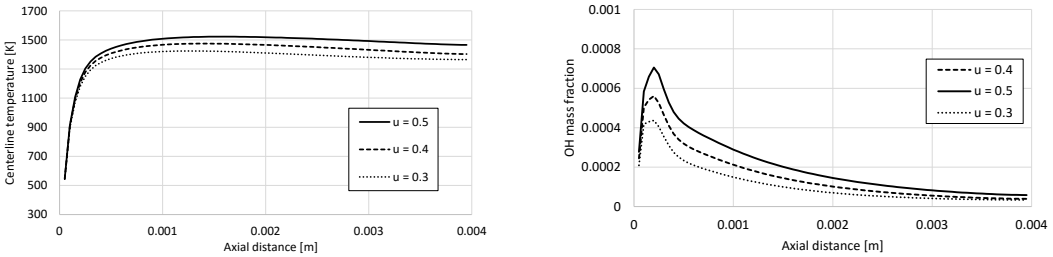

(a) *(b)*

Figure 6.11: Profiles in axial direction along the centerline: a) temperature, b) OH mass fraction, for different inlet mean velocities.

Figure 6.12 depicts the cross-section temperature profile at $x = 0.5$ mm, for the same three inlet mean velocities. At this coordinate, judging by the temperature profile, the flame is not completely formed in general, but the higher the inlet mean velocity, the further away the flame is from being completely formed, due to the competition of flow velocity and flame speed.

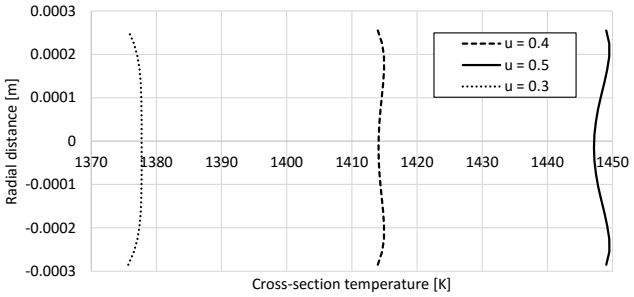

Figure 6.12: Cross-section temperature profile comparison for different inlet mean velocities at x = 0.5 mm.

In Figures 6.13a and 6.13b are depicted the temperature and OH mass fraction profiles for two different micro-combustor heights. The flame temperature along the combustor decreases more for lower combustor heights. This is expected to happen, since in this case, the surface to volume ratio decreases substantially, meaning the smaller combustor will be more exposed to heat loss through its walls. This reduction in size against the lower flame temperature and higher heat loss represents one of the main concerns when it comes to combustion in micro-scale.

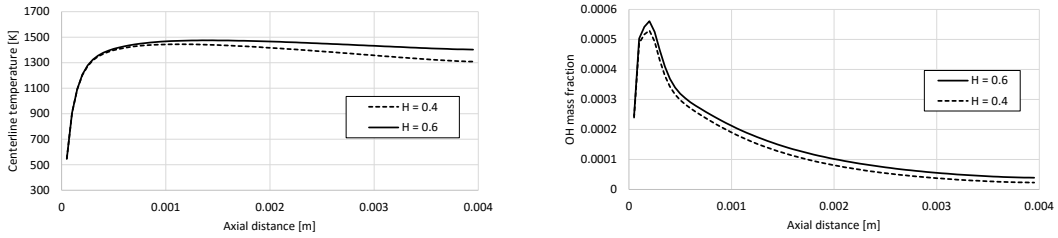

(a) *(b)*

Figure 6.13: Profiles in axial direction along the centerline: a) temperature, b) OH mass fraction, for different micro-combustor heights.

Figure 6.14 shows the cross-section temperature profile at $x = 0.5$ mm, for two different micro-combustor heights. At this location, in both cases the flames are practically already formed although the temperature differences are not significant yet, since at this point there was not enough length in the domain for the heat loss to be felt.

As mentioned earlier in this section, the obtained results here should only be analysed in a qualitatively way. This is due to the fact that the imposed gradient does not account for the micro-combustor wall thickness as well as the axial thermal conduction in the solid, that would allow the incoming unburned mixture to be pre-heated (although Rahaghi et al [31] also neglected it in this study). However, it was possible to see one the main consequences of reducing a combustor size to micro-scale, like the surface to volume ratio. Such is very well demonstrated in this case with the variation of the convective heat transfer coefficients and micro-combustor heights, resulting in a more accentuated heat loss to the exterior.

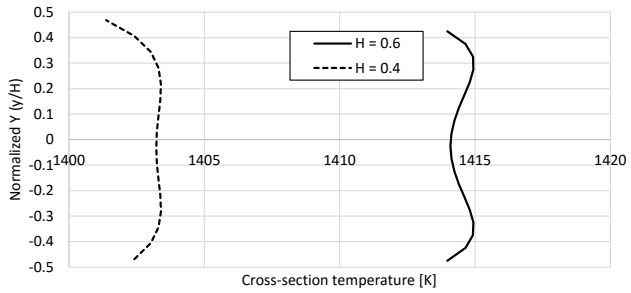

Figure 6.14: Comparison between cross-section temperature profiles for different micro-combustor heights at $x = 0.5$ mm.

Generally, all cases reported here took around 30 CPU hours to be simulated using four processors of the cluster. It was just needed a few microseconds to be run using Pimple code, and then the last obtained time instant would be sufficient to reach relatively fast steaty-state conditions using Simple code. When using the Pimple code, the imposed time step for all simulations was 10^{-6} seconds.

Several other simulations were performed in order to obtain results closer to those obtained by Rahaghi et al [31]. In fact, he spread the computational length to 6 mm, intending to overcome the problem of the flow not reaching fully developed state. This was also tried for case (a.1) in OpenFOAM and the results obtained were pretty similar to the ones obtained without the latter 2 mm. Furthermore, also for the case (a.1), instead of assuming a FD velocity profile, it was assumed an uniform velocity profile, and the results were also very similar.

6.2.2 Investigation on H_2/air premixed flames on micro-combustors with different physical and boundary conditions

Li et al [29] also studied numerically H_2/air premixed flames on micro-combustors varying physical and boundary conditions, using Fluent® Release 6.1.

6.2.2.1 Simulation setup

This study is similar to the previous one on H_2/N_2 premixed flames in the Section 6.2.1. Figure 6.15a shows a cross-sectional view of the micro-combustor - cylindrical tube with an inner diameter of 0.8 mm and 8 mm long - where steady-state combustion using premixed H_2/air takes place. The origin is fixed at the center of the inlet plane and x depicts the axial distance while the r represents the radial distance from the centerline of the cylindrical tube. To save computational time, the computational domain used for the case was axisymmetric.

The inlet stream is composed by premixed H_2/air with an equivalence ratio equal to 0.5, at ambient temperature and pressure, flowing in a fully developed velocity profile, with a mean velocity of 4 m/s. The swirl velocity in all domain is

assumed zero. A non-slip and slip wall BC are assumed for the nozzle and combustor wall, respectively. For the outlet BC, a zero gradient is applied when it comes to mass fractions, velocity components and temperature. The same boundary conditions are applied to the outer wall, with exception of the temperature field, where a profile is imposed. According to the results obtained by Li et al [29], two simulations were performed. For the first case, an uniform temperature of 1050 K is assumed, while in the second case the function of the external wall temperature obtained by Li et al [29] was extrapolated from his article, and used as a profile - both cases are organised in Table 6.4. The function is the following:

$$T(x) = 1041.8 + 41.583 * x - 22.854 * x^2 + 4.7878 * x^3 - 0.4683 * x^4 + (1.8e-2) * x^5 - (1e-5) * x^6 \quad (6.3)$$

A high temperature, 1600 K, is imposed on the entire computational domain as an initial guess, because it is important to be high enough to make sure the mixture will ignite. No spark is used in this study.

The computational grid resolution is 25 by 80 and a slightly higher level of refinement is used upstream. An example of the computational mesh is represented in Figure 6.15b.

Table 6.4: Operating conditions for two test cases

	Case	Wall surface temperature [K]
d = 1 mm	(a.1)	1050
	(a.2)	Extrapolated profile, in Eq. 6.3

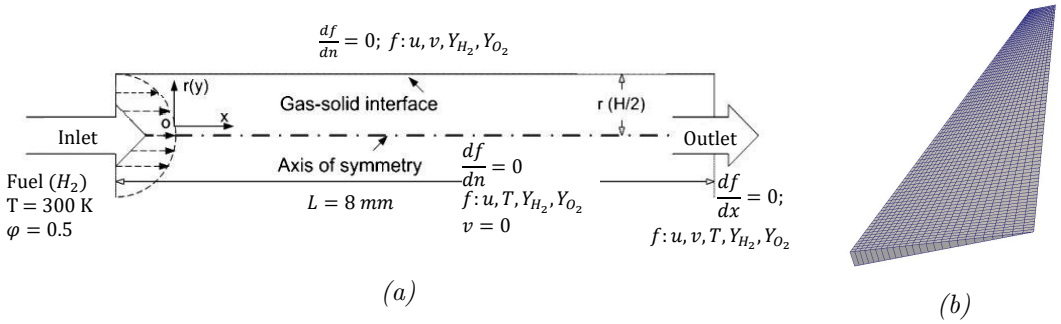

Figure 6.15: a) Schematic ilustration of computational domain coupled with boundary conditions, b) computational mesh, of hydrogen premixed flames in an axysymmetric pipe.

6.2.2.2 Results and discussion

Figure 6.16 illustrates the computed isopleths for H_2 mass fraction, axial velocity and temperature obtained by Li et al [29] using Fluent® and by using *laminarSMOKE*. Figure 6.16a presents the computed contours of H_2 mass fraction, from Fluent®, for the case (a.1) and for the case (a.2), respectively. The H_2 is mostly consumed within a thin layer of reacting gases while both temperature and velocity profile were being

developed along the micro-combustor, as shown in Figure 6.16b, that presents the computed contours of axial velocity, from Fluent®, for the case (a.1) and for the case (a.2), respectively, and in Figure 6.16c, that presents the computed contours of temperature, for the same cases as above. Note that in Figure 6.16c, Fluent shows temperature contours both for solid and gas phases. As in all cases, the temperature of the wall, in the case of Fluent, or the wall BC, in (a.1) and (a.2) cases, these temperatures are higher than the unburned incoming mixture, there will be a heat transfer from the wall to the gases and it will preheat the mixture in the pre-flame zone, which is a crucial phenomena to sustain the flame in micro-combustion.

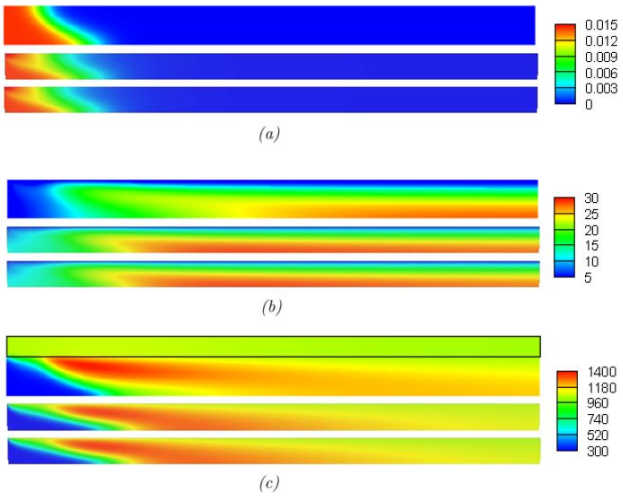

Figure 6.16: Computed isopleths, upper using Fluent, in the middle for case (a.1), lower for case (a.2): a) hydrogen mass fraction, b) axial velocity, c) temperature, of hydrogen premixed flames in an axysymmetric pipe. Fluent isopleths obtained by Li et al [29].

In Figure 6.17 are presented the temperature profiles along the micro-combustor centreline, obtained for both cases (a.1) and (a.2). It can be seen that the profiles are coincident, however, comparing them with the one obtained by Li et al [29], they overpredict the peak temperature in around 100 K and located it 3 mm before. Actually, the results of both cases are more similar, not with the cylindrical tube, but with the 2D parallel plate also studied by Li et al [29].

The computational domain was decomposed in four processors, taking around 120 CPU hours to finish, using the cluster. Similarly to the H_2/air premixed flames studied by Rahaghi et al [31], in the present study several microseconds were also initially simulated using Pimple code, and then Simple code was applied to reach steady-state. A time step of 10^{-8} seconds was imposed when using Pimple code.

Several other thermal boundary conditions at the wall were tried, in order to obtain results as closer as possible to those obtained by Li et al [29], or even to obtain a sustainable flame within the micro-combustor. One of those attempts involved imposing at the wall a similar gradient to the Equation 6.2, but that included the

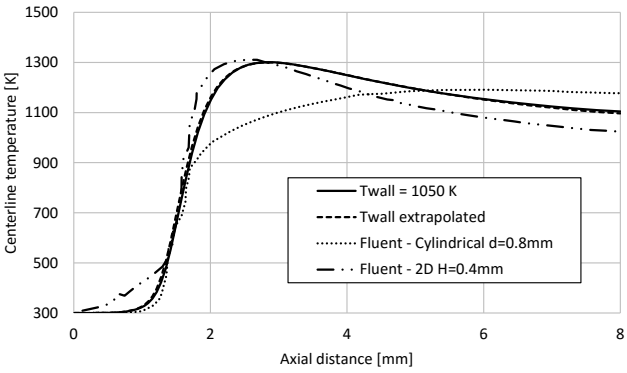

Figure 6.17: Temperature profiles at centerline when imposing a temperature of 1050 K, and when imposing an extrapolated wall temperature function at the wall, in the axial direction of the flow, along the centerline. Comparison of the computed profiles with the Fluent curves obtained by Li et al [29].

radiative heat flux, as in the following:

$$\frac{\partial T}{\partial n} = -\frac{h(T_{wall} - T_\infty) + \epsilon\sigma(T_{wall}^4 - T_\infty^4)}{\lambda_{fluid}} \tag{6.4}$$

where T_{wall} represents the temperature function expressed in Equation 6.3. Applying this combined thermal BC, the micro-combustor looses too much heat, decreasing the bulk temperature and the blow off phenomena is verified for steady-state.

As mentioned in Section 6.2.2, among some insufficiencies, the gradient in Equation 6.4 does not account for axial heat conduction at the wall (only transversal), which is particularly important to preheat the incoming burning mixture. Li et al [29] concluded that for an inlet velocity equal to 1 m/s, there was not much difference in the temperature field with or without disabled axial heat conduction. Having this in mind, it was tried the same imposed gradient combined with the extrapolated temperature function, and the obtained temperature profile is represented in the dashed line in Figure 6.18. Comparing this temperature profile with the one obtained from Li et al [29], it can be seen an over-prediction of the temperature peak by about 500 K. Since the temperature is imposed using the extrapolated function, the increase of the heat gradient at the wall imposes higher centerline temperatures, as shown in Figure 6.18.

Another thermal boundary condition was tried. In order to understand the effects of thermal boundary conditions in OpenFOAM, a similar expression to the one presented in Equation 6.4 was used. The only difference between the previous equation and Equation 6.5 is that no temperature profile was imposed at the wall BC. Instead, $T_{cell,f}$ is considered to be the wall temperature and is equal to the mean temperature of the cell (in the fluid domain) immediately next transversally to the boundary.

$$\frac{\partial T}{\partial n} = -\frac{h(T_{cell,f} - T_\infty) + \epsilon\sigma(T_{cell,f}^4 - T_\infty^4)}{\lambda_{fluid}} \tag{6.5}$$

In Figure 6.18, it is represented in a continuous line the temperature profile at the centerline when imposing the gradient presented in Equation 6.5, for an incoming mixture with a FD velocity profile with a mean velocity of 1 m/s. The temperature rapidly rises to its peak, 1835 K, within the first millimetre of the combustor and then it decreases all the way until exiting the combustor, at 805 K. The heat loss is much higher in this case since the cell temperature, which is part of the combustion flow, is being used to define the gradient, therefore the large heat loss. This flame can only be sustained due its low inlet velocity, where the importance of the axial heat conduction to preheat the mixture can be neglected. A mean velocity of 4 m/s was also tried, but the blow off phenomena occurred.

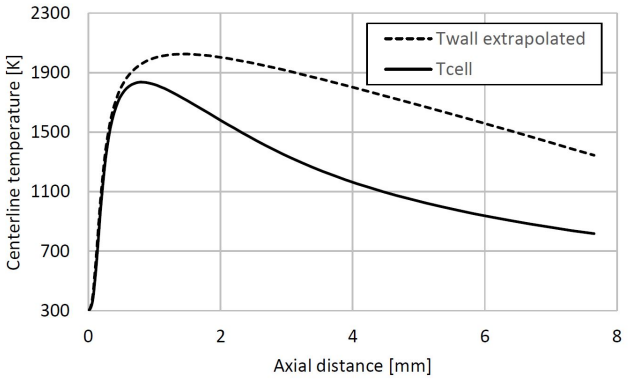

Figure 6.18: Temperature profile at the centerline when imposing the wall temperature profile from Equation 6.3 and the temperature gradient from the Equation 6.4, and when assuming the wall temperature equal to the temperature of the cell transversally next to the wall BC, for which case the heat loss is represented by the gradient in Equation 6.5, both cases for the flow speed equal to 1 m/s.

6.2.3 Investigation on CH_4/air premixed flames on micro-combustors with different physical and boundary conditions

Li et al [27] also studied numerically CH_4/air premixed flames on micro-combustor varying physical and boundary conditions, using Fluent® Release 6.3.

6.2.3.1 Simulation setup

Figure 6.19a shows a cross-sectional view of the micro-combustor - cylindrical tube with a variable inner diameter and 12 mm long - where steady-state combustion using premixed CH_4/air takes place. The origin is fixed at the center of the inlet plane and x depicts the axial distance while the r represents the radial distance from the centerline of the cylindrical tube. Again, to save computational time, the computational domain used for this case was axisymmetric.

The inlet stream is composed by premixed CH_4/air with a equivalence ratio equal to 0.9, at ambient temperature and pressure, flowing in a fully developed velocity profile, with a mean velocity of 0.5 m/s. The swirl velocity in all domain is

assumed zero. For the outlet BC, a zero gradient is applied when it comes to mass fractions, velocity components and temperature. The same BC's are applied to the outer wall, with exception of the temperature field, where a profile is imposed. For the four cases simulated, different uniform temperature profiles are assumed, as presented in Table 6.5, depending on the results obtained by Li et al [27].

A high temperature, 1600 K, is imposed on the entire computational domain as an initial guess, because it is important to be high enough to make sure the mixture will ignite. No spark was used in these simulations.

The computational grid is equispaced and has a resolution of 25 by 240. The boundary and initial conditions as well as the computational mesh are represented in Figure 6.19.

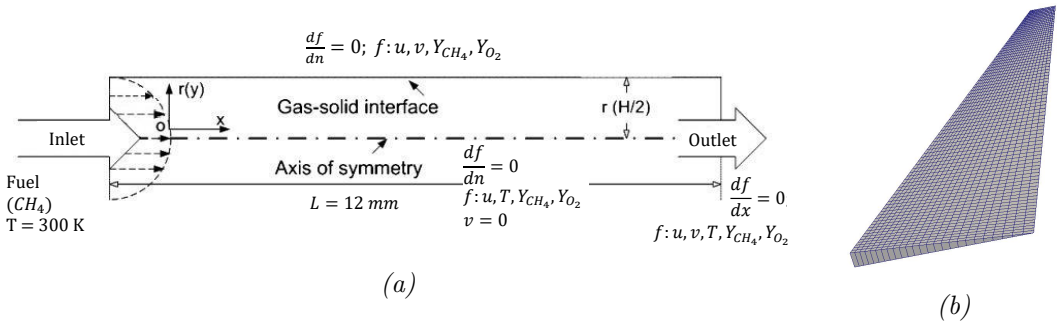

Figure 6.19: a) Schematic ilustration of computational domain coupled with boundary conditions, b) computational mesh, of methane premixed flames in an axysymmetric channel.

Table 6.5: Operating conditions for four test cases

	Case	Wall surface temperature [K]
d = 1 mm	(a.1)	1200
	(a.2)	1450
d = 2 mm	(b.1)	1650
	(b.2)	1750

6.2.3.2 Results and discussion

Figure 6.20 shows the computed isopleths for CH_4 mass fraction, axial velocity and temperature obtained by Li et al [27] using Fluent® and by using *laminarSMOKE*. Figure 6.20a illustrates the computed contours of CH_4 from Fluent, for case (a.1) and (a.2), respectively, for steady-state. It can be the seen that while CH_4 is being consumed for the Fluent and (a.2) case, the same is not verified in (a.1) case, which shows that CH_4 is flowing through the micro-combustor all the way until the outlet without any concentration variation. In Figure 6.20b is presented the computed contours of axial velocity, from Fluent®, for the case (a.1) and (a.2), respectively, and Figure 6.20c presents the computed contours of temperature, for the same cases as above. Note that Fluent shows temperature contours both for solid and gas phases.

Again, as explained in the previous section with H_2 flames, the fact that the wall and wall BC temperatures are higher than the unburned mixture will result in its preheating, making the flame possible to sustain. It can be seen that in the (a.2) case the flame is anchored more upstream than in the Fluent case, probably because the imposed temperature of 1450 K is too high for the upstream side wall, compared with Fluent, which causes an earlier ignition. Apart from this aspect, the 2 profiles seem to be identical. The reason why the (a.1) case shows these contours for steady-state is because the flame cannot sustain itself. Even though the initial internal field temperature was 1500 K that should be high enough to ignite the mixture. The fact that the wall temperature, 1200 K, strongly influences the flame temperature, seems to be insufficient to sustain the flame, which makes it eventually extinguishing.

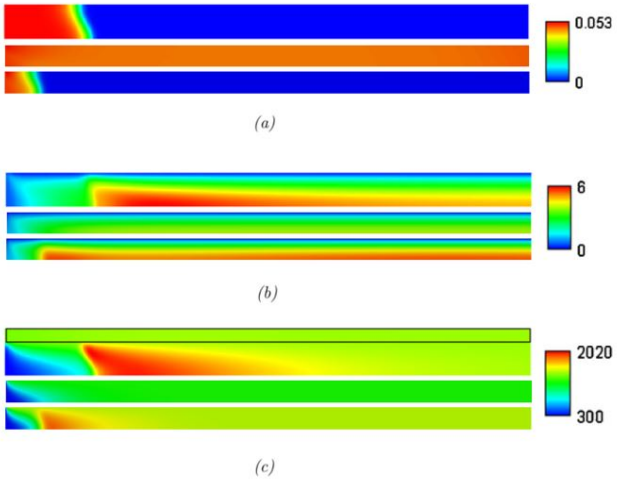

Figure 6.20: Computed isopleths, upper using Fluent, in the middle for case (a.1), lower for case (a.2): a) hydrogen mass fractio, b) axial velocity, c) temperature, of methane premixed flames in an axysymmetric channel with d = 1 mm. Fluent isopleths obtained by Li et al [27].

Figure 6.21 shows the temperatures profiles for CH_4 premixed flames along the centerline, for a cylindrical tube of $d = 1$ mm and $d = 2$ mm, imposing different temperatures at wall. It can be observed a rapid temperature jump to 1900 K around 1 mm after entering the micro-combustor for all cases, with the exception of (a.1), that only seems to be heated up relatively slowly until reaching 1200 K due to the wall temperature and nothing else happens. The confirmation that the wall temperature strongly determines the flow temperature can also be verified in the same figure. It can be also seen that for the (a.2) case, comparing with the $d = 2$ mm cases, the mixture is ignited more upstream since it is preheated faster due to the smaller distance from the centerline to the wall, related to the surface to volume ratio increase.

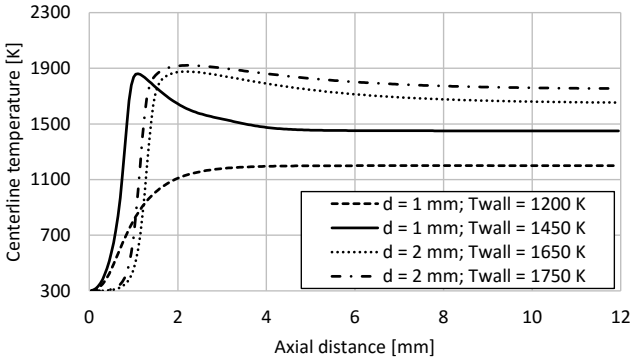

Figure 6.21: Temperature profiles at centerline when imposing different temperatures at the wall, in the axial direction of the flow, of methane premixed flames in an axysymmetric channel with d = 1 mm and d = 2 mm.

Comparing the premixed H_2/air and CH_4/air flames, it is possible to see that H_2 flame speed is larger than for CH_4. Furthermore, in H_2 cases, observing Figure 6.16c, it indicates that the high temperature zone is next to the wall, in contrast to what happens in the CH_4 flames, where the high temperature zone occupies a wider region of the radial section, demonstrated in Figure 6.20c. These distinctions of the flame structure are mainly attributed to the differences in terms of flow velocity and radial mass diffusivity of the two fuels.

The presented results were reached using eight parallel processors to obtain sufficient microseconds of the flow in which it is possible to see some stabilisation, using the transient version, Pimple code. Afterwards, the simulation is run using Simple code with four parallel processors, to reach steady-state. Overall, it took around 120 CPU hours to obtain the results.

Similarly to the previous H_2/air premixed flames studied by Li et al [29], the thermal boundary condition expressed in Equation 6.5, was also tried. Using this thermal BC, it was not possible to reach steady-state with a sustained flame. This is probably because the inlet velocity imposed in this case was too high to let it happen, unlike when the same BC was applied to H_2/air mixture and a sustainable flame was obtain, due to a lower inlet velocity employed. It is foreseen that if a sufficiently low inlet velocity was employed in this case, it would be also possible to obtain a sustainable flame.

6.2.4 Investigation on CH_4/air premixed flame dynamics on narrow 2D channels

Ayoobi [6] applied the *laminarSMOKE* solver to the study of flame dynamics in narrow 2D channels, having observed the symmetric and asymmetric oscillating flames, and Flame with Repetitive Extinction and Ignition (FREI) in one case. In the present section, it is intended to reproduce the study.

6.2.4.1 Simulation setup

Table 6.6: Operating conditions and simulated time (t_{sim}) for four test cases

	Case	ϕ	t_{sim} [s]
2 by 80 mm channel	(a.1)	0.53	0.129
	(a.2)	0.7	0.121
5 by 80 mm channel	(b.1)	0.53	0.215
	(b.2)	0.7	0.250

Channels with a length of 80 mm and two different heights, 2 mm and 5 mm, are tested, as presented in Table 6.6. The 2-mm channel is selected to be of the order of the flame thickness, whereas the 5-mm channel allows the appearance of asymmetric flame dynamics, as documented in [66][67][68]. For the inlet, two different equivalence ratios for each simulated channel height are used for the premixed CH_4/air, 0.53 and 0.7, composing four different cases. The inlet velocity profile is assumed fully developed with a mean velocity of 0.4 m/s, common in every case. It should be noted that this velocity is higher than the laminar flame speed at standard temperature and pressure. For the outlet BC, a zero gradient is applied when it comes to mass fractions, velocity components and temperature. The same is applied for the upper and lower wall, excepting the temperature field. A non-slip wall BC is applied in all cases. A linear temperature ramp profile is imposed on both sides: at the inlet, the wall temperature is set to 300 K, increasing linearly until 1900 K at the outlet, resulting in a gradually higher heating of the incoming unburned mixture. All simulations start with an internal field composed only by air at 300 K and ambient pressure.

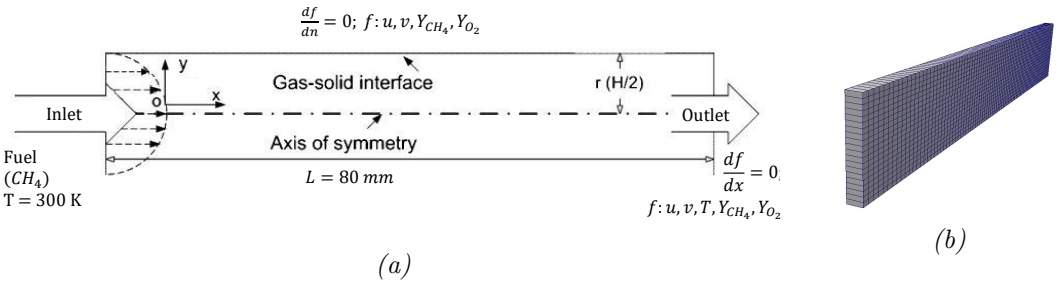

Figure 6.22: a) Schematic ilustration of computational domain coupled with boundary conditions, b) computational mesh, of CH_4 premixed flames on an narrow 2D channel.

An equispaced grid with a resolution of 15 by 350 for the 2 mm channel height is used, while for the 5 mm channel height 27 by 350 was set. The boundary and initial conditions as well as a computational mesh for one of the cases, are represented in Figure 6.22.

For the cases with stationary reaction fronts, simulations are continued for about one flow-through times after ignition. For the cases with non-stationary reaction fronts, simulations are continued until data for at least two limit cycles or

ignition-extinction events are obtained.

6.2.4.2 Results and discussion

Figures 6.23 and 6.24, 6.25 and 6.26 illustrate the formation of stationary and symetric flames for $\phi = 0.53$ and $\phi = 0.7$, respectively, for the cases (a.1) and (a.2). In Figures 6.23 and 6.25, the total heat release is shown as a function of time. For both equivalence ratios, the unburned mixture is gradually more heated up, as the wall temperature also rises along the channel, and further downstream, when gases temperatures are sufficiently high, the mixtures auto-ignite. Figures 6.24 and 6.26 present the heat release fields during ignition and flame stabilisation for the cases (a.1) and (a.2), for different time instants. As it is possible to see, after ignition, at $x = 50$ mm for both $\phi = 0.53$ and $\phi = 0.7$, the flame propagates upstream until it becomes stationary. When the flame is propagating upstream, that is when the heat release peaks are registered, as show in Figures 6.23 and 6.25. Observing the heat release contours for the different time instants, it can be seen that, initially, at $t = 60$ ms, for both equivalence ratios, the flame front curve faces downstream, and in the following instants until they stabilise, the flame front curve faces upstream.

As expected, in the leaner case ($\phi = 0.53$), the stationary flame anchors more downstream, in the hotter region, when compared with the richer case ($\phi = 0.7$), as it releases less chemical energy, even though both cases have equal inlet velocities. To burn at the same velocity, the peak temperatures have to be similar, which according to the numerical results for the flame front: $T = 1738.8$ K for $\phi = 0.53$, while $T = 1837.4$ K for $\phi = 0.7$.

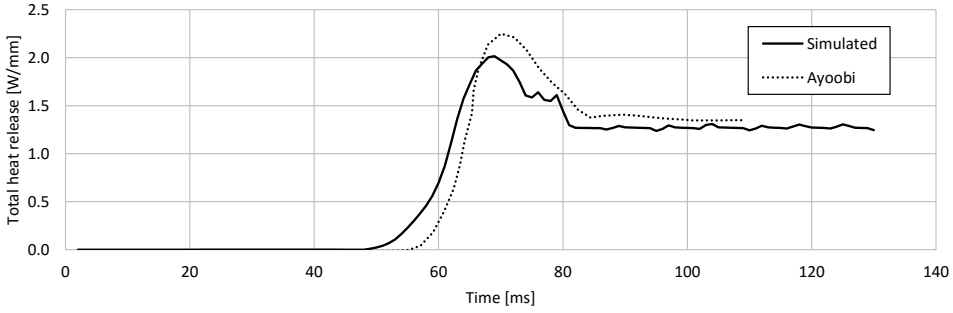

Figure 6.23: Total heat release as a function of time in a 2 by 80 mm-channel at $\phi = 0.53$. Ayoobi curve obtained in [6].

The increasing of the channel height from 2 to 5 mm changes the flame dynamics drastically, as shown in Figures 6.27 - 6.31, that illustrate flame behaviours for the (b.1) and (b.2) cases. In theses cases, the flame no longer stabilises, instead it forms limit cycles. In Figures 6.27 and 6.30, the total heat release is shown as a function of time. The flame continues to be ignited further downstream where the wall temperature is higher. After an initial total heat release peak, the flame looses its symmetry and its position oscillates.

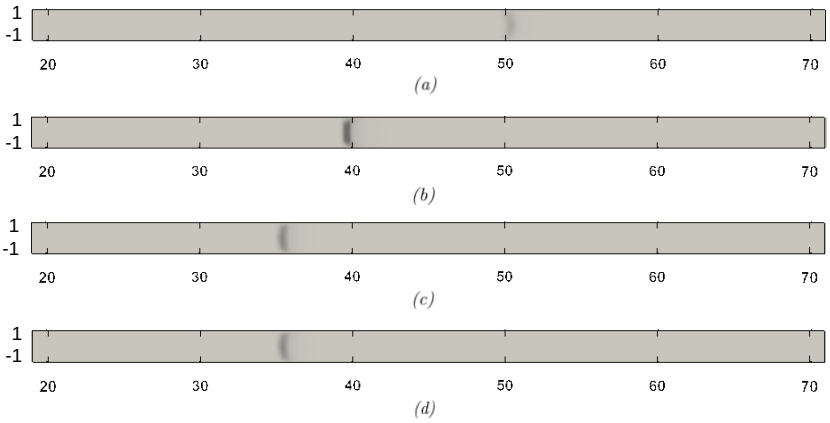

Figure 6.24: Heat release fields during ignition and flame stabilization in a 2 by 80 mm-channel at $\phi = 0.53$, at the specific following time instants: a) t = 60 ms, b) t = 70 ms, c) t = 80 ms, d) t = 90 ms. A symmetric flame stabilizes after initial behaviour. The field maps are scaled from zero (grey) to 4 W/mm^3 (black).

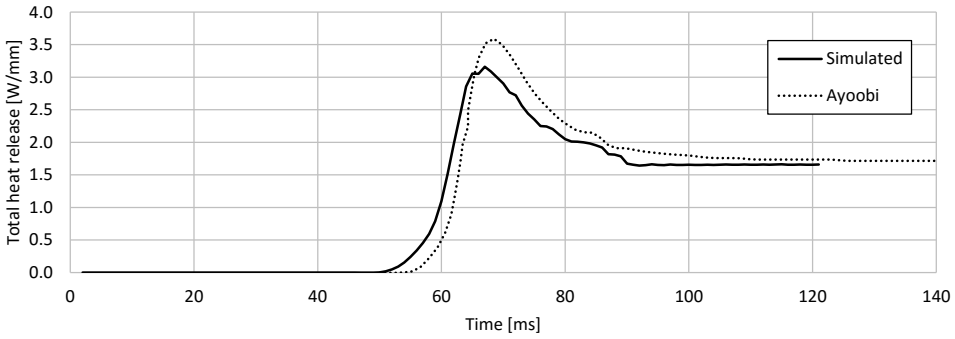

Figure 6.25: Total heat release as a function of time in a 2 by 80 mm-channel at $\phi = 0.7$. Ayoobi curve obtained in [6].

Figures 6.28 presents the heat release fields during ignition for the cases (b.1), and Figures 6.29 and 6.31 present the heat release fields during the periodically flopping of the flame, for the cases (b.1) and (b.2), all for different time instants. During ignition, the elongated symmetric flame is shorten and moved upstream, as observed in Figure 6.28. For $\phi = 0.7$, the ignition processes very similarly to the previous case. After the ignition, the symmetry is lost, resulting in limit cycles substantially different for each equivalence ratio, as show in Figures 6.29 and 6.31.

For the leaner case, $\phi = 0.53$, the limit cycle involves an asymmetric flame front which ends oscillate back and forth. One end advances in the combustor while the other is receding, originating variations of total heat release, well described in Figure 6.27.

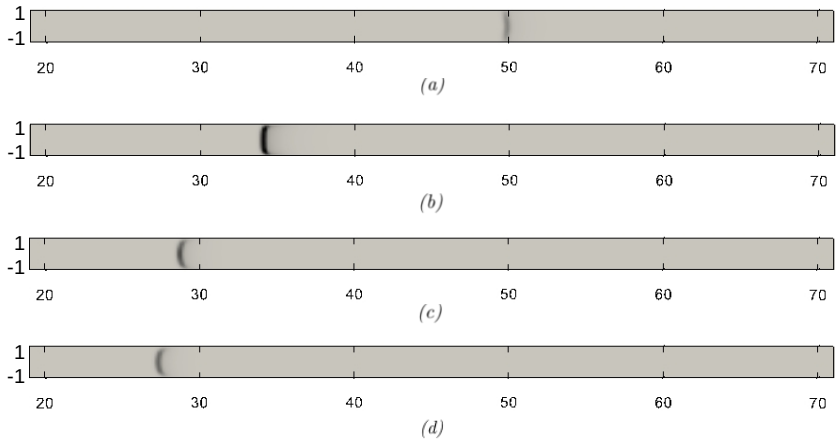

Figure 6.26: Heat release fields during ignition and flame stabilization in a 2 *by* 80 *mm-channel at* $\phi = 0.7$*, at the specific following time instants: a)* $t = 60$ *ms, b)* $t = 70$ *ms, c)* $t = 80$ *ms, d)* $t = 90$ *ms. A symmetric flame stabilizes after initial behaviour. The field maps are scaled from zero (grey) to 3* W/mm^3 *(black).*

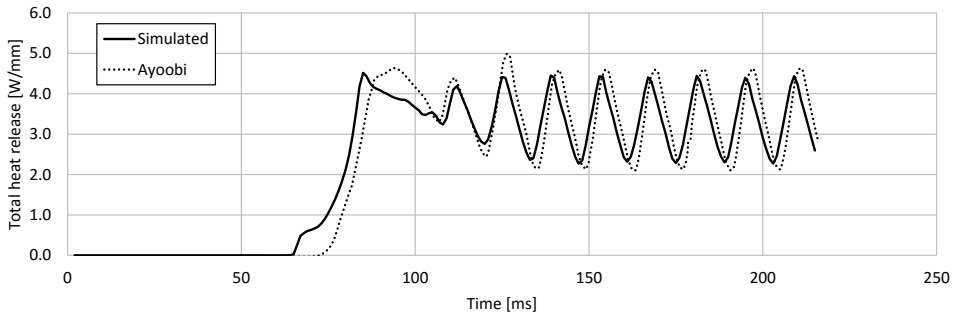

Figure 6.27: Total heat release as a function of time in a 5 *by* 80 *mm-channel at* $\phi = 0.53$*. Ayoobi curve obtained in [6].*

For the richer case, $\phi = 0.7$, it was expected and intended to observe flames with repetitive extinction and ignition (FREI). However, most likely due to an insufficient level of refinement of the used computational mesh, it was not possible to obtain, according to Figure 6.30.

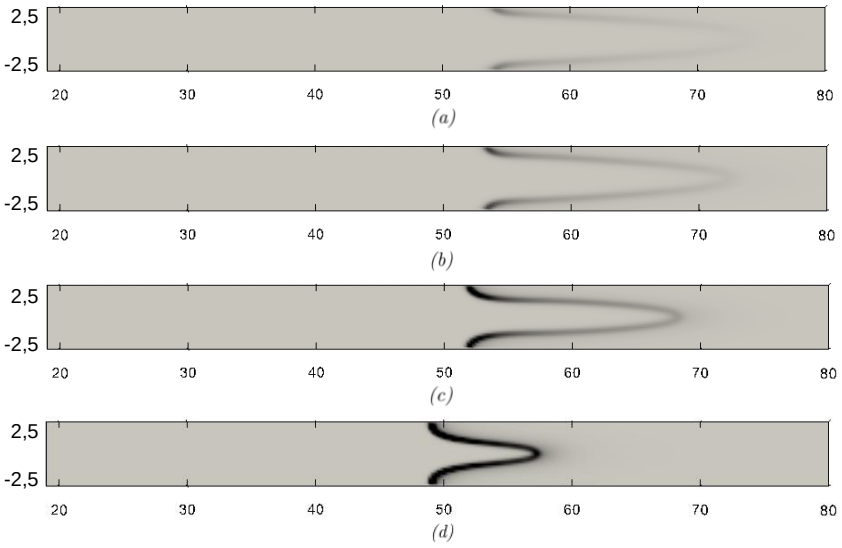

Figure 6.28: Heat release fields during ignition in a 5 *by* 80 *mm-channel at* $\phi = 0.53$*, at the specific following time instants: a) t = 74 ms, b) t = 78 ms, c) t = 82 ms, d) t = 86 ms. The flame is symmetric during ignition. The field maps are scaled from zero (grey) to 1.3* W/mm^3 *(black).*

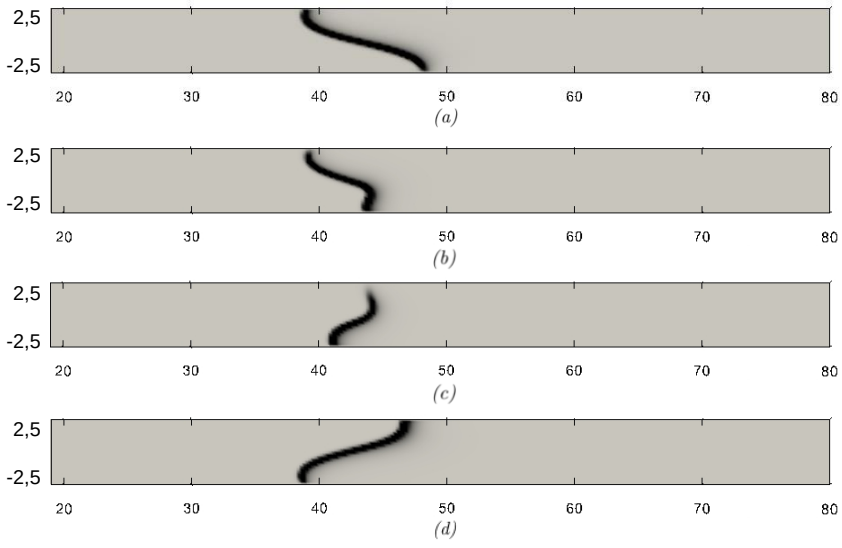

Figure 6.29: Heat release fields during for half of a limit cycle in a 5 *by* 80 *mm-channel at* $\phi = 0.53$*, at the specific following time instants: a) t = 180 ms, b) t = 190 ms, c) t = 200 ms, d) t = 210 ms. An asymmetric flame flops periodically. The field maps are scaled from zero (grey) to 1.3* W/mm^3 *(black).*

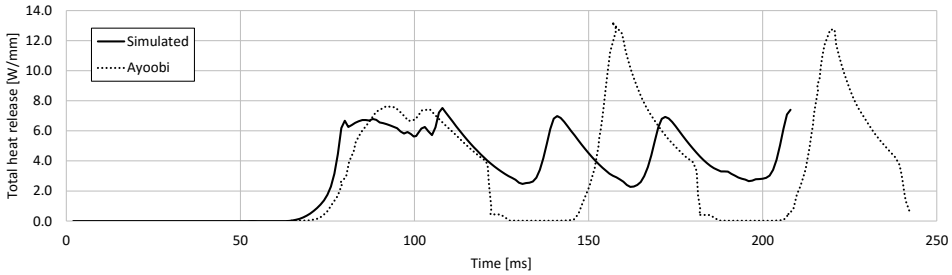

Figure 6.30: Total heat release as a function of time in a 5 by 80 mm-channel at $\phi = 0.7$. Ayoobi curve obtained in [6].

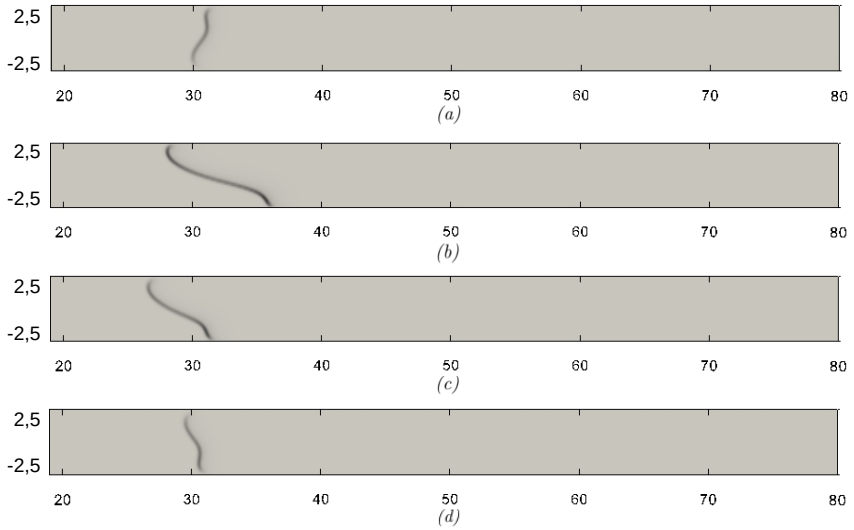

Figure 6.31: Heat release fields during for half of a limit cycle in a 5 by 80 mm-channel at $\phi = 0.7$, at the specific following time instants: a) t = 130 ms, b) t = 140 ms, c) t = 150 ms, d) t = 160 ms. An asymmetric flame flops periodically. The field maps are scaled from zero (grey) to 4 W/mm^3 (black).

Overall, the obtained results clearly showed that symmetric flame behaviour is only observed in the narrower 2 mm channel. For the wider channel height, the ignition was followed by asymmetric limit cycles behaviour.

Comparing the obtained results here, with those obtained by Ayoobi et al [6], for the 2 mm channel height cases, the ignition occurs a few milliseconds earlier and until the flame finally stabilises, the delay becomes smaller, which is expected to happen as the resolution of the used grid is pratically three times less refined, according to [6].

6.3 Diffusion flames with inserted porous media

6.3.1 Investigation on H_2 diffusion flames with inserted porous media

This investigation was carried out in order to accomplish one of the three main objectives of this work, which was to study the effect of inserting a porous media within a combustion chamber at micro and meso-scale, on the emission of pollutant gases.

6.3.1.1 Simulation setup

In this study it is intended to simulate a 2D planar combustion chamber. Figure 6.32a shows a cross-sectional view of the computational domain in which steady-state combustion takes place using H_2 fuel with a porous media inserted within a 150 mm long by 95 mm high combustion chamber. The origin is fixed at the center of the fuel inlet plane and x depicts the axial direction of the flow whereas the y represents the vertical direction. The nozzle is 8 mm long and 9 mm high, with a 1 mm width, and is surrounded by an air-coflow quadrangular annulus. The properties of the flow both inside and outside of the nozzle are calculated, in order to take into account the back diffusion of species into the tube.

The fuel stream is composed by H_2 and N_2, each of them with a mole fraction of 0.5, at ambient temperature and pressure, fed with a FD profile with a mean velocity of 25 cm/s. For the outlet and combustor top and bottom walls, as well as for the nozzle tube, the boundary conditions were defined by a zero gradient for the velocity, temperature, species mass fractions and pressure profiles. The porous surfaces were set as walls and a zero gradient for the boundary conditions was imposed for all the previous parameters, excepting for the thermal BC. A non-slip BC is assumed for the porous surfaces and nozzle whereas for the combustor walls was assumed slippery. The simulations started with an internal field of the domain at ambient pressure and temperature. Since the flame would be ignited right after the nozzle when contacting with the O_2, it was imposed a finer refinement of the grid in these region as well as in the area involving the porous media. This computational mesh was designed using both *blockMesh* and *snappyHexMesh* utilities and a representation is shown in Figure 6.32b.

Fourteen different cases were simulated, which can be divided in three different geometries: (a) a porous media placed in the middle of the combustion chamber 30 mm distanced from the top and bottom walls, which computational mesh is represented in Figure 6.32b; (b) a porous media placed in the middle of the combustion chamber confined between the top and bottom walls, which mesh in shown in Figure 6.33a; (c) a compressed porous media placed in the middle of the combustion chamber confined between the top and bottom walls, 8 mm downstream of the nozzle exit, which mesh in shown in Figure 6.33b. The height of the meso-scale combustor in cases (b) and (c) is 35 mm. The previous cases were chosen to analyse the effect of the combustor walls next to or further away from porous media, as well as the effect of reducing the porous sizes. For each geometry, different thermal boundary

conditions were employed to the porous surfaces, as in the following: (0) no porous media inserted in the combustor; (1) surface considered adiabatic; (2) surface at a temperature of 1000 K; (3) surface at a temperature of 1250 K; (4) surface at a temperature of 1500 K. All presented cases are organised in Table 6.7. In this table there is no (c.0) case since it is the same as (b.0).

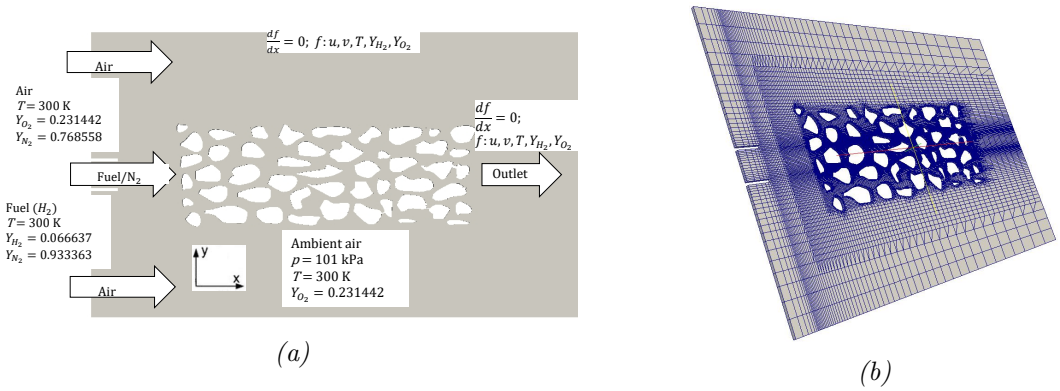

Figure 6.32: a) Schematic ilustration of computational domain coupled with boundary conditions, b) computational mesh, of H_2/N_2 coflow flames with a porous media inserted within the combustion chamber.

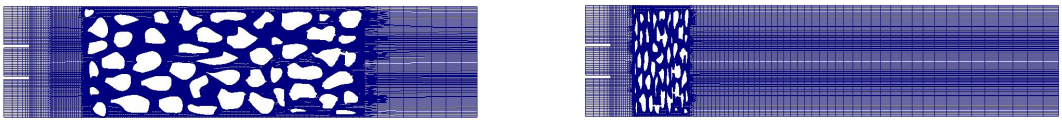

Figure 6.33: Computational meshes applied for the cases: a) (b.0) to (b.4), b) (c.1) to (c.4).

Table 6.7: Operating conditions and simulated time (t_{sim}) for fourteen test cases

Case	Porous thermal BC	t_{sim} [s]
(a.0)	Without porous	0.50
(a.1)	Adiabatic	1.26
(a.2)	T = 1000 K	0.80
(a.3)	T = 1250 K	0.80
(a.4)	T = 1500 K	0.80
(b.0)	Without porous	0.50
(b.1)	Adiabatic	0.26
(b.2)	T = 1000 K	0.50
(b.3)	T = 1250 K	0.44
(b.4)	T = 1500 K	0.25
(c.1)	Adiabatic	-
(c.2)	T = 1000 K	0.38
(c.3)	T = 1250 K	-
(c.4)	T = 1500 K	0.225

6.3.1.2 Results and discussion

Figures 6.34, 6.36 and 6.38 show the map of NO_x mass flow rate for different thermal boundary conditions of the porous surfaces, for the cases (a), (b) and (c), respectively. In Figures 6.35, 6.37 and 6.39, it is show the NO_x mass flow rate at the outlet, for different thermal boundary conditions of the porous surfaces, for the cases (a), (b), and (c), respectively.

Relatively to the cases (a), it can be seen that in Figures 6.34 and 6.35 there are practically no differences between the different thermal boundary conditions applied to the porous surface. This happened because, observing the map of NO_x mass flow rate, it is possible to see that the porous inserted does not influence much the NO_x formation, because it goes around it. Anyway, it can be noticed that in the case without the porous inserted, the NO_x mass flow rate at the outlet is much higher comparing to the remaining cases.

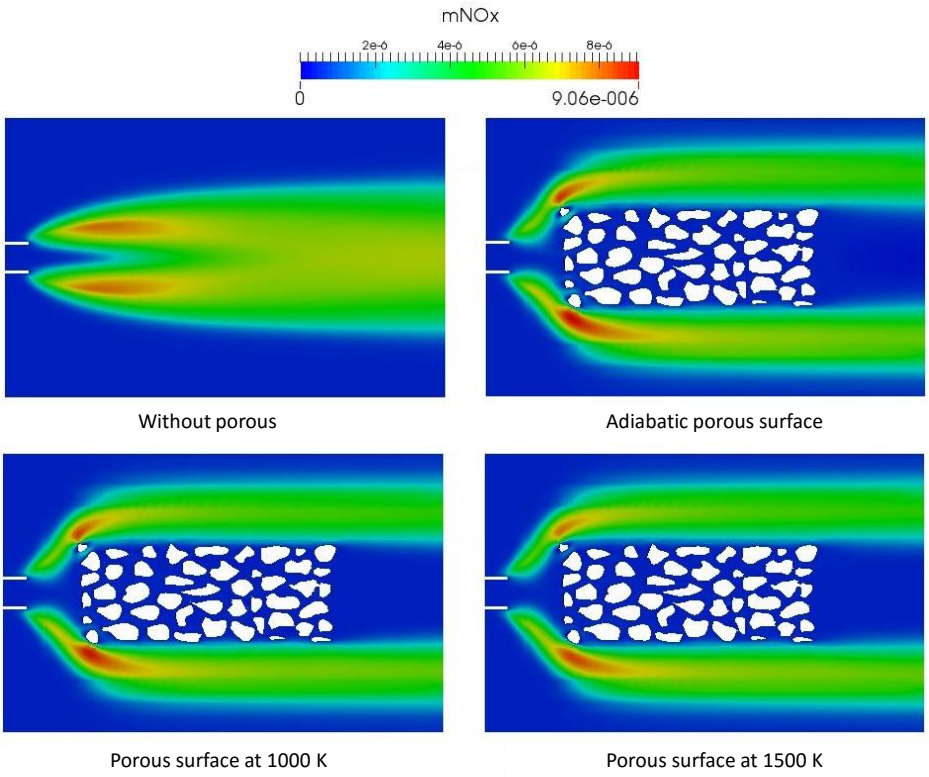

Figure 6.34: Map of mass flow rate of NO_x for different thermal BC at the porous surface, of H_2/N_2 coflow flames for the cases (a).

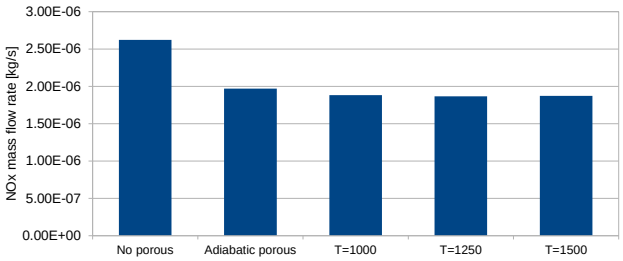

Figure 6.35: Mass flow rate of NO_x for different thermal BC at the porous surface, at the outlet of the combustor, of H_2/N_2 coflow flames for the cases (a).

Relatively to the cases (b), represented in Figures 6.36 and 6.37, it is already possible to see some differences. The combustion flow already propagates through the porous media and is already influenced by their boundary conditions. The cases without porous and with adiabatic porous surface are those that produce more NO_x, since the temperature is higher. The source for NO_x here is the thermal NO_x formation. Note that thermal NO_x refers to the NO_x formed through high temperature oxidation of the N_2 found in the combustion air. Its formation rate depends on the temperature and residence time of N_2 at that temperature. At high temperatures, molecular N_2 and O_2 in the combustion air dissociate into their atomic states and participate into a series of reversible reactions.

However, when a temperature lower than the flame temperature is imposed to the porous surface, the thermal NO_x is reduced, as it can be observed in the comparison of the results for the adiabatic wall and T = 1250 K, presented in Figure 6.37. Increasing the porous wall temperature up to 1500 K, increases the thermal NO_x formation, as expected.

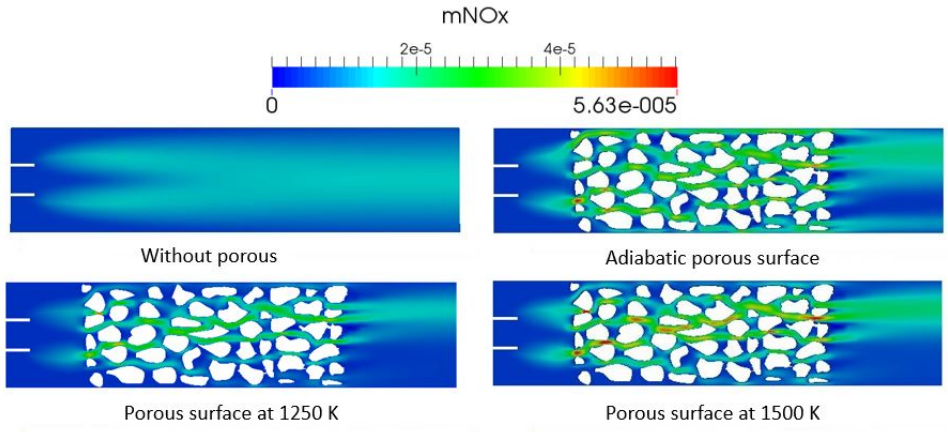

Figure 6.36: Map of mass flow rate of NO_x for different thermal BC at the porous surface, of H_2/N_2 coflow flames for the cases (b).

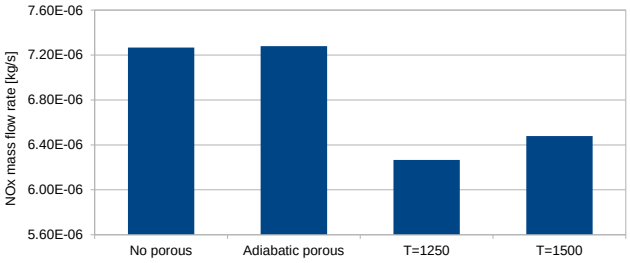

Figure 6.37: Mass flow rate of NO_x for different thermal BC at the porous surface, at the outlet of the combustor, of H_2/N_2 coflow flames for the cases (b).

Relatively to the cases (c), shown in Figures 6.38 and 6.39, the same conclusions can be taken as for the cases (b). The case without porous and with adiabatic porous surface produce the more NO_x, whereas the lower temperature profile imposed to the porous surface produces the lower value of NO_x. Furthermore, the effect of the porous compression from the cases (b) to (c) made the combustion flow go through the smaller porous holes, contacting closer to the porous surface, resulting in a less production of NO_x. This means the combustion flow will have higher velocities to go through the smaller porous, therefore the residence time is lower, which also results in lower NO_x formation.

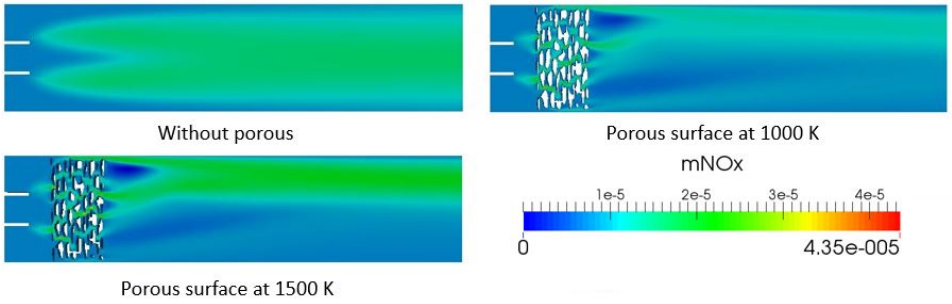

Figure 6.38: Map of mass flow rate of NO_x for different thermal BC at the porous surface, of H_2/N_2 coflow flames for the cases (c).

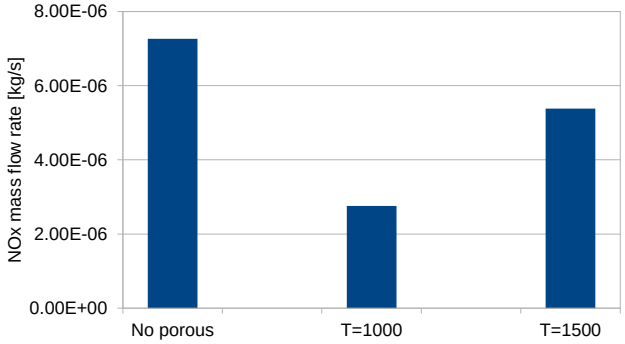

Figure 6.39: Mass flow rate of NO_x for different thermal BC at the porous surface, at the outlet of the combustor, of H_2/N_2 coflow flames for the cases (c).

In Appendix B, it is possible to see the evolution in time of the average temperature, heat released, and OH, NO_x, CO and CO_2 mass fractions per cubic metre, for the different simulated cases.

All presented cases were run in the cluster using only Pimple code due to the complexity of the flow, and a time step of 10^{-8} s. Eight processors were used to simulate each case, having taken between 2500 and 3500 CPU hours each, with the exception of cases without a porous, which were considerably faster. The complexity of the simulations were due to the complex kinetic mechanisms, that accounted for NO_x species and more, and due to the much higher level of refinement around and among the porous media. It was intended to use more CPU's, but the cluster was frequently busy.

6.4 Chapter summary

Throughout all cases in this chapter, it is indeed possible to conclude that *laminarSMOKE* solver can simulate a combustion flow at micro-scale in simple and complex geometries, for steady-state and unsteady conditions, although with an arguable accuracy. Furthermore, this solver presents some limitations that cannot be neglected. It can only obtain a sustainable flame in the mentioned cases if it is imposed a certain temperature profile as the thermal boundary condition in the micro-combustor walls. On the cases in which the inlet velocity is below a certain level and the axial heat conduction in the wall does not make much difference in preheating the mixture, it is also possible to obtain a sustainable flame, however, with values quite different from the real ones.

The deviation caused by using the gas phase model from macro and mesoscale to micro-scale combustors is that the surface to volume ratio increases substantially, resulting in a combustor heat loss that can no longer be neglected and that turns out to be crucial in sustaining the flame, as seen in most of the cases studied in this chapter.

Summing up, it is not likely that the *laminarSMOKE* is able to study combustion flows autonomously, without using information from another studies to reach steady-state, like the temperature profiles the homologous studies obtained for the wall, as it was used in this chapter.

Chapter 7

Solid and gas phases modelling

Given the great increase of the surface to volume ratio, the combustor heat loss through its walls can no longer be neglected. So, in order to make it possible to use the *laminarSMOKE* solver to simulate reacting flows under stationary or unsteady conditions in simple and complex geometries, at micro-scale, in an autonomous way and independent from third party information, the heat transfer in the wall should be properly defined and taken into account during the gas phase calculations. This could be done by solving the energy equations both for the solid and gas phase domains simultaneously, a phenomena which is named Conjugate Heat Transfer (CHT) problem.

The Conjugate Heat Transfer problem can be defined as the interaction between the thermal conduction in the solid domain and the convection occurring in the fluid domain in contact with the solid.

There are mainly two numerical approaches to solve CHT problems, known as Conjugate Approach and Coupled Approach, which will be briefly explained in the following sections.

7.1 CHT Governing Equations

The governing equations for the fluid and solid domains are presented below. For the fluid domain, they are the same as presented in Section 3.1, with the energy equation reproduced in the following:

$$\rho C_P \frac{\partial T}{\partial t} + \rho C_P \mathrm{v} \nabla T = -\nabla \mathrm{q} - \rho \sum_{k=1}^{NC} C_{P,k} \omega_k \mathrm{V}_k - \sum_{k=1}^{NC} h_k \dot{\Omega}_k \tag{7.1}$$

For the solid domain, the energy equation is:

$$\rho_s C_{P,s} \frac{\partial T_s}{\partial t} = Q_s - \nabla(\lambda_s \nabla T_s) \tag{7.2}$$

where ρ_s is the density of the solid $\left[kg/m^3\right]$, $C_{P,s}$ is the specific heat of the solid $\left[J/kgK\right]$, T_s is the temperature of the solid $\left[K\right]$, Q_s is the heat source inside the solid $\left[W/m^3\right]$, λ_s is the thermal conductivity of the solid $\left[W/mK\right]$ and t is time.

Note that in CHT problems it should be guaranteed the continuity of temperature and heat flux at the common interface, as shown in the Equations 7.3 and 7.4:

$$T_f = T_s \tag{7.3}$$

$$\lambda_f \frac{\partial T_f}{\partial n} = -\lambda_s \frac{\partial T_s}{\partial n} \tag{7.4}$$

7.2 Modelling

7.2.1 Computational approaches

Some possible different ways to solve CHT problems, as well as some advantages and downsides related to them, will be briefly presented here. As mentioned in the beginning of this chapter, it is possible to use either the Conjugate or Coupled Approach.

The Conjugate Approach is characterized by the use of an unique solver, usually based on Finite Volume Method, for both fluid and solid domains. This approach is the most common in commercial and open-source codes. One way to use this approach would be by simply setting the velocity to zero and the density of the solid as a constant in the solid domain, in this way there would be only left the energy equation when dealing with this domain. Another way would be to use an expression representative of both Equations 7.1 and 7.2, and the fluid or solid properties would be used in the expression, depending on the position in the total domain. One of the advantages of using this approach is the absence of interpolation of the solution at the fluid and solid interface, which reduces computational time. On the opposite side, it does not allow the use of different numerical methods for each domain, that would be particularly useful due to the much higher time constant typical in the solid.

On the other hand, the Coupled Approach is characterised by the use of a different solver for each domain. In fact, the Finite Element Method is usually preferred to be used on the solid domain, while the Finite Volume Method continues to be used in the fluid domain. These different methods of calculus implies the exchange of information at the interface of the coupled domains. The advantages of using such approach are: (1) the possibility of using already existing codes, extensively validated; (2) using two different solvers, the different time constant in the solid and fluid domain can be taken into account, adopting a proper technique for each of them; (3) the higher time constant in the solid allows the use of steady-state FEM, that converges the solution rapidly. While in the Conjugate Approach the solid domain was solved for every single time step, with this approach it is only solved after several time steps, when the update of the interface boundary conditions is needed. Regarding the downsides, the following should be considered: (1) for transient simulations, the iterative procedure of transferring information between the domains is complicated; (2) for non-matching meshes between the two domains, interpolation of information at the interface can take much more time, which can decrease the advantage of saving computational time due to the use of different solvers for each domain. The coupling algorithms currently used are distinguished according to the type of information they exchange in the interface, normally taking the fluid as a

reference for naming the different methods. They are:

- Flux Forward Temperature Back (FFTB) - the heat flux obtained on the fluid side of the interface is imposed on the solid domain, whereas the temperature distribution obtained in the solid side is sent to the fluid domain, demonstrated in Figure 7.1. This method is stable if Bi < 1.

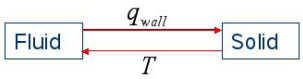

Figure 7.1: FFTB algotrithm [69].

Note that the Biot number, is a dimensionless number, that represents the ratio between the conductive resistance (L/λ_s) and the convective resistance in the flow boundary surface $(1/h)$, as expressed in Equation 7.5.

$$Bi = \frac{hL}{\lambda_s} \tag{7.5}$$

- Temperature Forward Flux Back (TFFB) - is the opposite case of previous algorithm, the temperature distribution obtained in the fluid side is imposed on the solid domain, while the heat flux obtained in the solid side is sent to the fluid domain, demonstrated in Figure 7.2. This method is stable if Bi > 1.

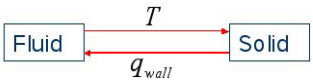

Figure 7.2: TFFB algotrithm [69].

For the previous two cases, convergence is reached when both temperature and heat flux are equal on both sides of the interface. There are cases where lies a need of a relaxation factor during the iterative process, useful to increase the stability range. In such cases, the following two algorithms represent the alternative where the convective heat flux coefficient h plays a relaxation role, by means of a Robin boundary condition applied on the solid:

- Heat Transfer Coefficient Forward Temperature Back (hFTB) - the Robin BC employed here consists in a combination of Neumann and Dirichlet conditions represented by the heat transfer:

$$q_{wall} = h(T_{wall} - T_{fluid}) \tag{7.6}$$

Then the solution is computed and the temperature distribution is imposed on the fluid domain, as represented in Figure 7.3.

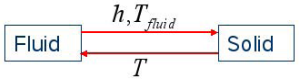

Figure 7.3: hFTB algotrithm [69].

- Heat Transfer Coefficient Forward Flux Back (hFFB) - this algorithm is practically the same as the previous one, the only difference is that the heat flux is imposed on the fluid domain instead of the temperature distribution.

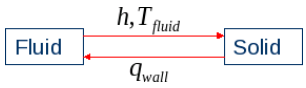

Figure 7.4: hFFB algotrithm [69].

Further information on these algorithms can be checked in [69].

7.2.2 Solid and gas phases modelling

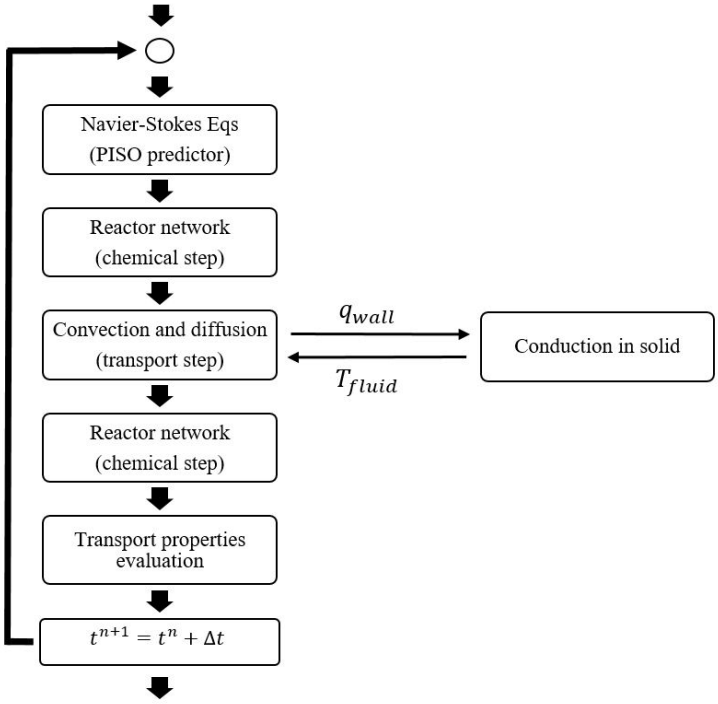

Figure 7.5: Numerical procedure adopted in chtlaminarSMOKE. In the left side is addressed to the fluid domain, whereas the right side to the solid domain.

In the present thesis, a Coupled Approach using the FFTB algorithm between the solid and fluid domains was modelled. This algorithm was choosen for the type of cases presented in this thesis, since the problems to be dealt with involved Bi < 1. For the transient forced convection, the laminar Navier-Stokes equations were solved in the fluid region, while the Laplace equations were solved in the solid region, according to [70].

Note that the continuity of temperature and heat flux, represented in Equations 7.3 and 7.4, at the common interface have to be guaranteed. So the loop flux

forward and temperature back will be iterated until the temperature and heat flux differences at the two domains common interfaces are below the desirable numerical error. Once the convergence is reached, then the physical time step is incremented, demonstrated in Equations 7.7 and 7.8.

$$-\lambda_s \frac{\partial T_s}{\partial n}^{n+1} = \lambda_f \frac{\partial T_f}{\partial n}^{n} \tag{7.7}$$

$$T_f^{n+1} = T_s^n \tag{7.8}$$

The created solver was named *chtlaminarSMOKE*, since it is a version of *laminarSMOKE* adapted to solve CHT problems. The numerical procedure adopted in the new solver can be seen in Figure 7.5. The *Policy_cht* file, main file of the solver that defines the interface for interacting with OpenFOAM and its data types, can be seen in Appendix C.1.

7.2.3 New file structure and features

To run properly a simulation using the *chtlaminarSMOKE* solver, the case folder should be organised has shown in Figure 7.6.

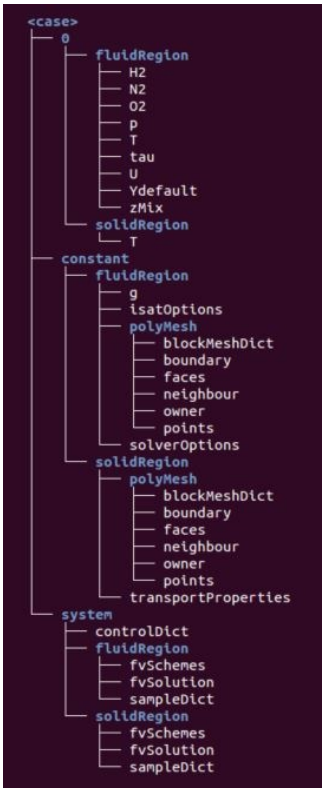

Figure 7.6: Case file structure ready to run chtlaminarSMOKE solver.

There are some notes to point out which the user of this solver should be aware of. The computational mesh is built exactly the same way as for the Finite Volume Method. The way the solver's code was programmed, both fluid and solid meshes have to be built in separate case folders, as if each one constituted a different case.

Once the *blockMesh* utility is run for both fluid and solid separate cases, then *polyMesh* folder should be copied to *fluidRegion* and *solidRegion* folders, respectively, within *constant* folder of the CHT case. Furthermore, within the *blockMeshDict* file for the fluid and solid domains, the boundaries of the common interface should be set as a *wall* and named exactly "fluid_interface" and "solid_interface", respectively. By doing so, the code will automatically calculate the temperature gradient from the fluid domain to the solid and vice versa, independently of the imposed thermal BC at the common interface of both domains.

Properties of the solid, such as the thermal conductivity, density, specific heat and thermal diffusivity are to be set in *transportProperties* file located in the folder *constant/solidRegion*. An example of the file is available in Appendix C.2. In order to solve the energy equation on the solid side, *chtlaminarSMOKE* requires as input either the thermal conductivity or the thermal diffusivity, depending on which compiled version it is being used. In Equation 7.9 it is presented λ_s, the thermal conductivity tensor. Depending on which directions the conduction is intended to be studied associated with the dimension of the geometry in question, the tensor should be filled accordingly.

$$\lambda_s = \begin{bmatrix} \lambda_{xx} & 0 & 0 \\ 0 & \lambda_{yy} & 0 \\ 0 & 0 & \lambda_{zz} \end{bmatrix} \tag{7.9}$$

For example, if is intended to study a 2D CHT problem in x and y cartesian coordinates, using a solid material with a thermal conductivity equal to 20 W/mK, then the previous matrix should be filled as exemplified in Equation 7.10. If the thermal diffusivity is used as an input, the exactly same analogy from the thermal conductivity case is applied.

$$\lambda_s = \begin{bmatrix} 20 & 0 & 0 \\ 0 & 20 & 0 \\ 0 & 0 & 0 \end{bmatrix} \tag{7.10}$$

Finally, a case can be run in a pseudo-transient way, by setting a value to the variable s_0 in the *transportProperties* file. This variable will multiply the transient term in the solid energy equation, shown in Equation 7.11, this way increasing the time step, and will allow getting a faster solution in the solid domain, that typically has much higher time constants comparing with the fluid domain.

$$s_0 \rho_s C_{P,s} \frac{\partial T_s}{\partial t} = -\nabla(\lambda_s \nabla T_s) \tag{7.11}$$

7.2.4 Final remarks

Should be noted that it is not possible to decompose neither the fluid nor the solid domain into different processors, that could reduce the computational time substantially.

7.3 Validation of solid and gas phases model

The numerical validation performed followed the procedure adopted by Panara et al [70], that validated the code against analytical results of unsteady forced convection

in a laminar flow [71].

7.3.1 Simulation setup and results

The geometry of the forced convection laminar flow is a pipe with inner radius of R_1. The pipe wall has a width of R_2. The origin is fixed at the center of the inlet plane and x depicts the axial distance while the r represents the radial direction. The computational grid is composed of 15 by 100 cells in the fluid domain and 7 by 100 in the solid domain.

The pipe and the fluid simulated have a heat conductivity ($K_r = \frac{K_s}{K_f}$) and heat diffusivity ratio ($\alpha = \frac{\alpha_s}{\alpha_f}$) of 10 and 1. The fluid enters the pipe at the axial coordinate $x = 0$ with an inlet temperature T_i. At the first time instant, $t = 0$, the flow and the solid wall are considered to be at thermal equilibrium, both with temperature T_i. At time > 0, it is suddenly employed a different temperature to the outer pipe wall, $T_w < T_i$.

The non-dimensional temperature distribution in the fluid and solid pipe wall region is shown at two different time steps ($\tau = \frac{v_f t}{R_i^2}$, where v_f is fluid kinematic viscosity and R_i is the pipe inner radius). Figure 7.7 shows the hydraulically fully developed and the thermally developing flow along the pipe, referring to non-dimensional axial coordinate $X = 0.7$, for two time steps.

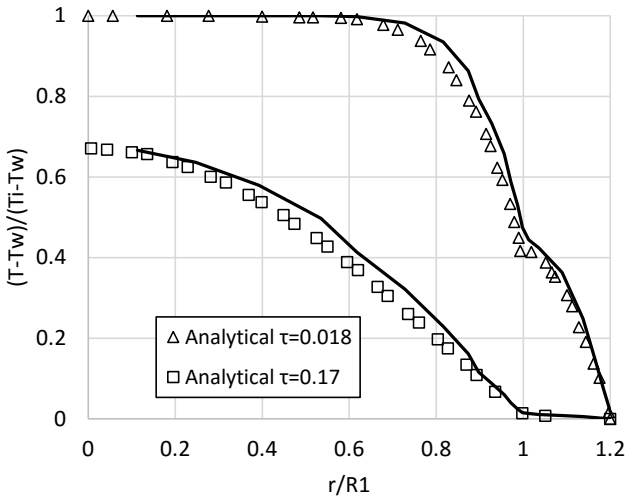

Figure 7.7: Temperature distribution of conjugate laminar pipe flow, at the non-dimensional axial coordinate $X = 0.7$. Teoretical values to compare with were obtained by Ozisik [71].

The obtained results in the previous figure seem to be in agreement with the obtained analytical solution by Ozisik [71]. This was mainly why no more numerical validations were performed and it was preferred to simulate some of the already studied cases.

Chapter 8

Numerical studies using solid and gas phases model

In this chapter, two studies will be carried out using the new solid and gas phases model created in Chapter 7, the *chtlaminarSMOKE* solver. These studies already took place in Chapter 6 using only the gas phase model, so in this chapter it is intended to obtain more accurate results since the heat transfer in the solid domain is being taken into consideration.

8.1 Diffusion flames

8.1.1 Assessment of H_2 micro-jet diffusion flames

As mentioned in Section 6.1.1, Cheng et al [34] carried out detailed measurements of temperature and major species concentrations, in laminar micro-jet diffusion flames for different Reynolds numbers. They have also simulated the same cases numerically, using the commercial CFD package CFD-ACE to solve the governing equations, with the input of the molecular transport data from CHEMKIN package.

8.1.1.1 Simulation setup

All parameters presented in Section 6.1.1 for the fluid domain are the same used in this study, with the exception of the boundary conditions at the common interface with the solid domain. The initial temperature of the fluid BC in this interface is set to be 300 K.

The dimensions of the solid domain are such that fit perfectly into the empty space not occupied by the fluid domain, as shown in Figure 8.1. The thermal BC of the face of the solid domain turned outside was considered to be adiabatic. According to Cheng et al [34], the nozzle tube is made of stainless-steel (AISI 304), which has the following properties: thermal conductivity is 16.2 W/mK, density is 8000 kg/m^3, the specific heat is 500 J/kgK and the emissivity is 0.5. Two simulations with different Reynolds numbers were performed: Re = 30 and Re = 330. For Re = 30, the grid is composed of 66 by 100 cells in the fluid domain and 7 by 35 in the solid domain. For Re = 330, the grid is composed of 63 by 66 cells in the fluid domain and 7 by 26 in the solid domain. Both grids are more refined

near the nozzle exit and an enlarged grid is set forth toward the boundaries. The grid used for Re = 30 is more refined since it is expected more influence of the nozzle tube (solid domain) in sustaining the flame. Pimple code was used in both simulations, although setting s_0 to 10^{-5} to speed up the solution in the solid domain.

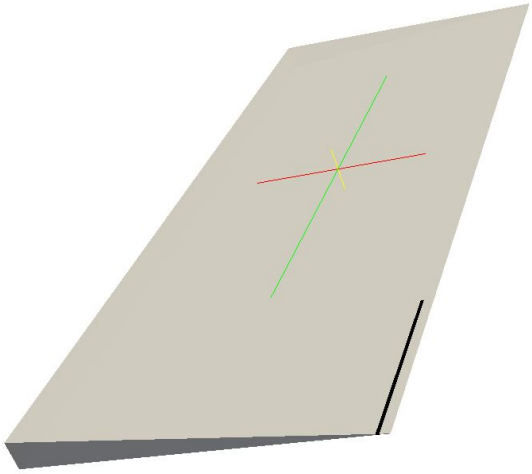

Figure 8.1: Computational mesh of hydrogen jet diffusion flames.

In order to better understand the effects of the nozzle wall boundary conditions on the flame structure of the Re = 30 case, one additional simulation was performed, in which the nozzle wall is assumed to have an infinite thermal conductivity ($\lambda_s = 10^{12}$ W/mK). The rest of the simulation parameters remained the same.

8.1.1.2 Results and discussion

Figures 8.2 and 8.3 show the photographs, single-pulse LIPF-OH images and computed OH isopleths using the solid and gas phases model, of hydrogen jet flames.

Figures 8.2a and 8.2b, already shown in Section 6.1.1, are again presented here to compare the flame more easier with the newly computed OH isopleths using the solid and gas phases model in Figure 8.2c. In this figure, it is already possible to see clear improvements and similarities on the flame shape, compared with the photograph and experimental values. Similarly to the single-pulse LIPF image, the computed OH isopleths also show a higher concentration of this specie in the lower part of the flame. According to the computed results obtained by Cheng et al [34], the OH concentration peak corresponded to 0.0105 whereas the obtained peak here is 0.00992, which is much closer than the obtained results using only the gas phase model. However, it should be noted that the flame is anchored 1 mm away from the nozzle exit and around 2 mm away from where the flame in the photograph and single-pulse image anchors. Furthermore, it can be seen that the flame is also thinner than that of single-pulse image.

Figures 8.3a and 8.3b, also already shown in Section 6.1.1, are presented here to compare the flame more easier with the newly computed OH isopleths using the

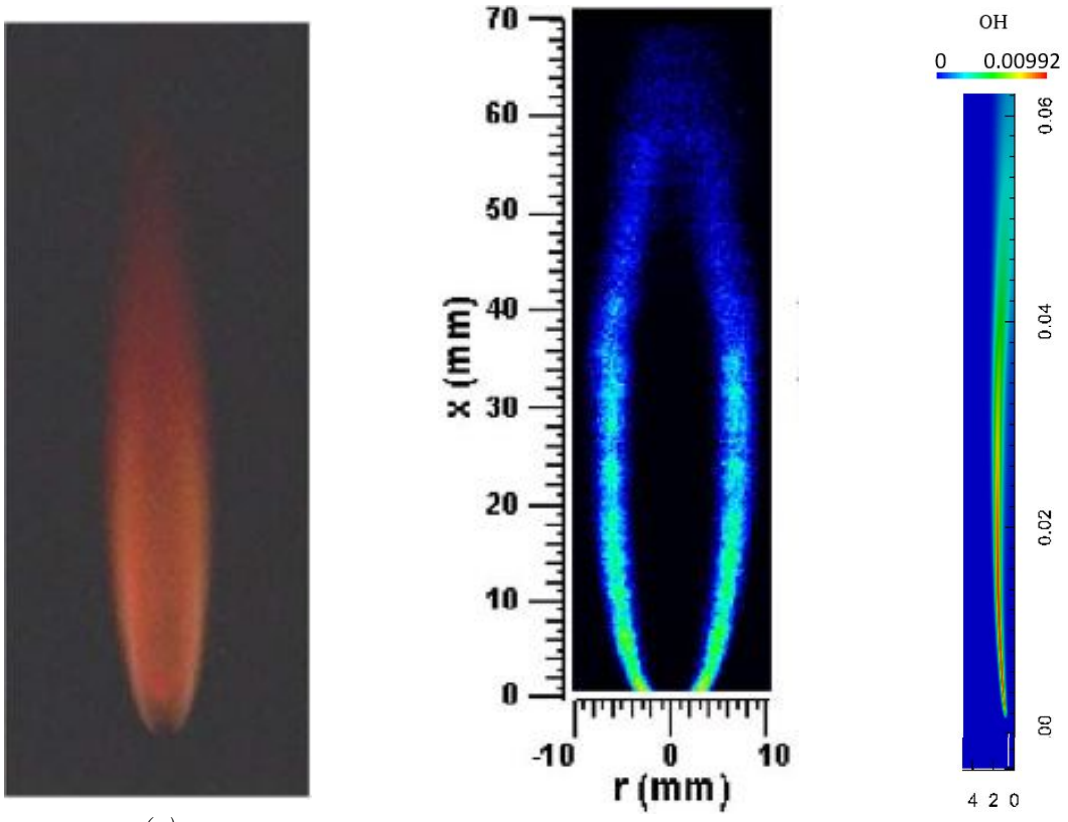

(a) (b) (c)

Figure 8.2: a) Photograph, b) single-pulse LIPF-OH image, c) computed OH isopleths using the solid and gas phase model, for hydrogen jet diffusion flames with Re = 330. The axial coordinates in the computed OH isopleths are in metres. Photograph and single-pulse LIPF-OH image obtained by Cheng et al [34].

solid and gas phases model in Figure 8.3c. In this figure, on the opposite of using only the gas phase model, it is already possible to see substantial improvements on the flame shape, compared with the photograph and experimental values. Similarly to the single-pulse LIPF-OH image, that seems to have a higher concentration of this specie in the lower part of the flame, the computed OH isopleths share a very similar concentration map. According to the computed results obtained by Cheng et al [34], the OH concentration peak corresponded to 0.0074 whereas the obtained peak here is 0.0091, which is also much closer than the obtained results using the *laminarSMOKE* solver. The relative error between the OH concentration peaks is higher for Re = 30 than that for Re = 330, because the wall effect is higher for flows with lower velocities. Although the obtained flame seems to have the approximately the same length, it can be seen that the flame is a bit thinner than that of single-pulse image.

In Figure 8.4 is shown the comparison between measured temperature, major species and OH mass fractions with the computed results using the solid and gas phases model, along the centerline of the flow. It is already possible to see that a considerably good agreement between the obtained computed results and exper-

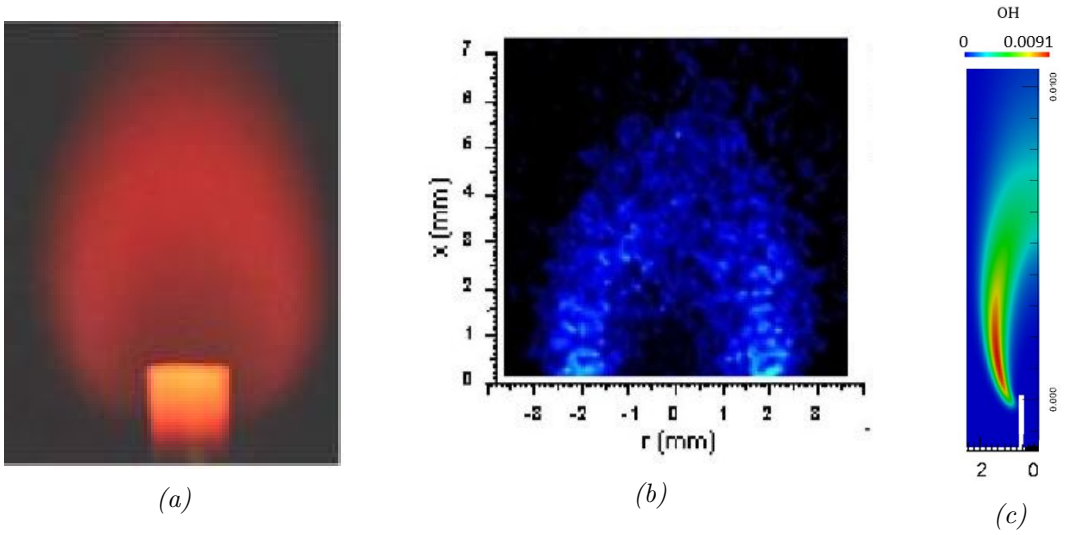

Figure 8.3: a) Photograph, b) single-pulse LIPF-OH image, c) computed OH isopleths using the solid and gas phase model, for hydrogen jet diffusion flames with Re = 30. The axial coordinates in the computed OH isopleths are in metres whereas the radial are in millimetres. Photograph and single-pulse LIPF-OH image obtained by Cheng et al [34].

imental values. The bigger deviation corresponds to experimental and computed H_2O mass fraction between the 10 and 25 mm after the nozzle exit.

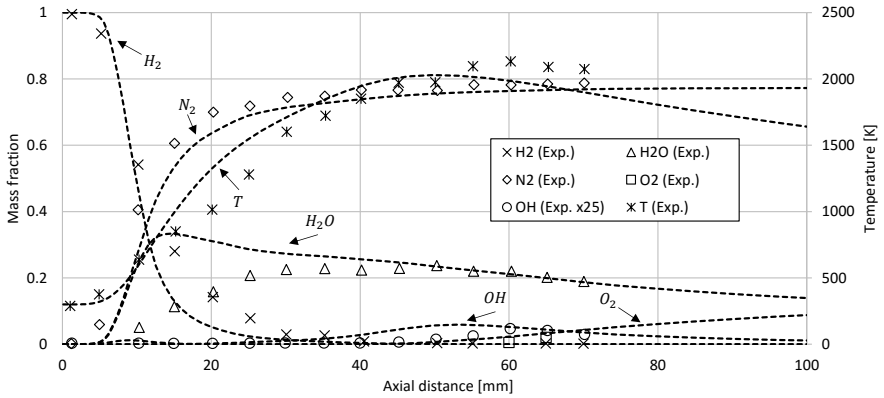

Figure 8.4: Comparison between measured temperature, major species and OH mass fractions, with computed results in axial direction, for hydrogen jet diffusion flames with Re = 330. Experimental measurements obtained by Cheng et al [34].

In Figure 8.5 is shown the comparison between measured temperature, major species and OH mass fractions with the computed results using the solid and gas phases model, in the radial direction, when $x = 5$ mm. In this figure, it can be easily seen some consequent effects of the flame being anchored around 2 mm further downstream compared with the experimental values. At $x = 5$ mm, which is an axial coordinate where experimental values have been collected, the computed flame did not have the much space yet to develop itself, and this is the main reason

behind the major deviations in the mentioned figure. At this point, the majority of profiles seem to be underdeveloped compared with the experimental values. It should be expected better agreements between the computed results at $x = 7$ mm and experimental values at $x = 5$ mm. In Figure 8.6 it is presented the computed results at $x = 7$ mm. According to this figure, it can be seen that the generally the different profiles get closer to the experimental values. The position of the profiles differ that much as the computed flame is considerably narrower than the one obtained experimentally.

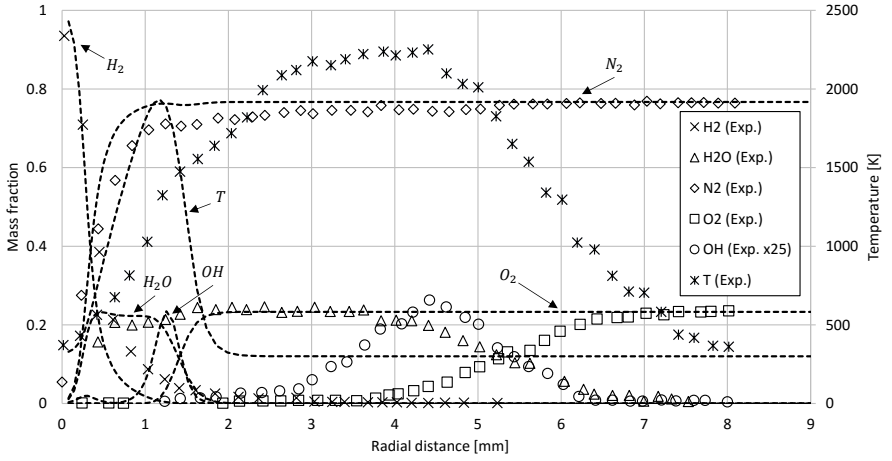

Figure 8.5: Comparison between measured temperature, major species and OH mass fractions, with computed results in radial direction, at x = 5 mm, for hydrogen jet diffusion flames with Re = 330. Experimental measurements obtained by Cheng et al [34].

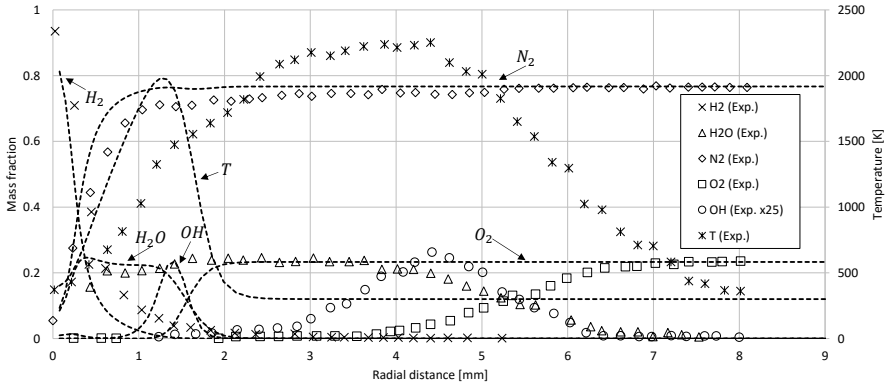

Figure 8.6: Comparison between measured temperature, major species and OH mass fractions at x = 5 mm in the radial direction, with computed results, at x = 7 mm, for hydrogen jet diffusion flames with Re = 330. Experimental measurements obtained by Cheng et al [34].

In Figure 8.7 is shown the comparison between measured temperature, major species and OH mass fractions with the computed results using the solid and gas phases model, along the centerline of the flow. There are not many experimental values available to compare with, but the ones that exist show very good agreement

with the computed results.

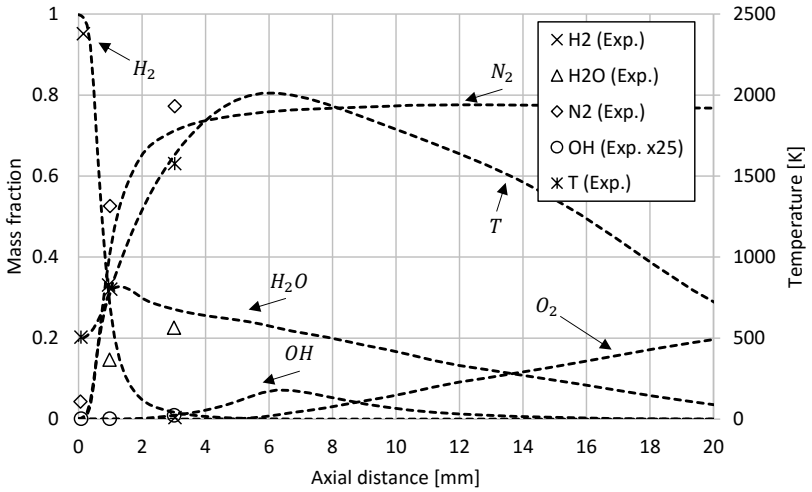

Figure 8.7: Comparison between measured temperature, major species and OH mass fractions, with computed results in axial direction, for hydrogen jet diffusion flames with Re = 30. Experimental measurements obtained by Cheng et al [34].

In Figure 8.8 is shown the comparison between measured temperature, major species and OH mass fractions with the computed results using the solid and gas phases model, in the radial direction, at $x = 0.1$ mm. As it can be seen, most of the differences between the computed and experimental results are a reflex of a thinner flame. Radially, from the centerline out, most of the computed profiles seem to follow considerably close the experimental values, although, between 1 and 2 mm which is the widest span of the flame, it changes. For instance, the temperature profile decreases rapidly, and when it comes to mass fractions: the OH has its peak at around 1.2 mm - in agreement with the fact the flame is very narrow - and then decreases; the water decreases and the O_2 increases rapidly and stabilise.

Figures 8.9 and 8.10 present the comparison between measured and computed axial and radial profiles, respectively, of temperature, major species and OH mass fraction. The computed profiles differed on the thermal boundary condition applied to the nozzle wall: the continuous line corresponds to the case that assumes the wall to have an infinite thermal conductivity whereas the dashed line corresponds to the standard case, where the wall temperature is variable. Observing both figures, it can be said that the assumption of variable wall temperature leads to better agreement with the experimental results in axial direction along the centerline, as depicted in Figure 8.9. On the other hand, the assumption of infinite wall thermal conductivity leads to better agreement with the experimental values in core of the fluid, better exemplified in Figure 8.10. This happens due to the fact that, with infinite wall thermal conductivity, the heat inside the nozzle is easily transferred through the nozzle wall.

For all the cases presented here, the fact that different kinetic mechanisms

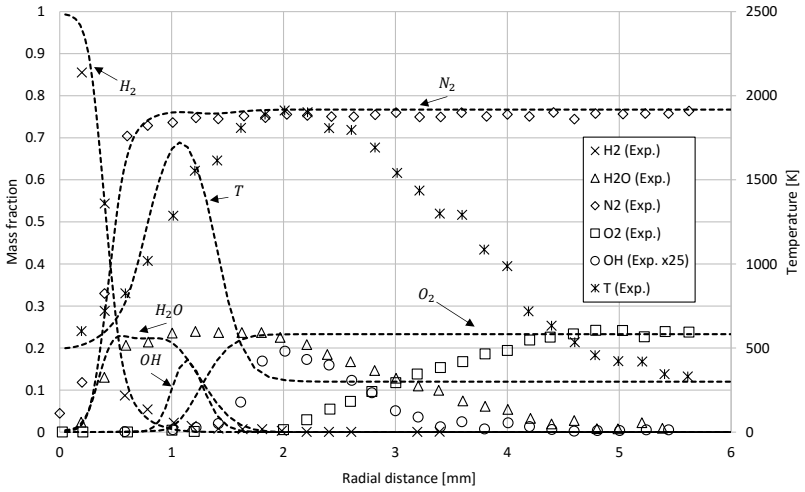

Figure 8.8: Comparison between measured temperature, major species and OH mass fractions, with computed results in radial direction, x = 0.1 mm, for hydrogen jet diffusion flames with Re = 30. Experimental measurements obtained by Cheng et al [34].

were used between the *chtlaminarSMOKE* and Fluent simulations, also partially contributes to a general deviation of the results.

As final remarks, the presented results were simulated during 170 CPU hours using only processor in the cluster, although should be noted that steady-state was not fully reached in both cases. The time step set for these simulations was 10^{-7} s.

8.2 Premixed flames

8.2.1 Investigation on H_2/air premixed flames on 2D micro-combustor with different physical and boundary conditions

As mentioned in Section 6.2.2, Li et al [29] studied numerically H_2/air premixed flames on micro-combustors varying physical and boundary conditions, using Fluent® Release 6.1.

8.2.1.1 Simulation setup

All parameters presented in Section 6.2.2 for the fluid domain are the same used in this study, with the exception of the boundary conditions at the common interface with the solid domain. The initial temperature of the fluid BC in this interface is set to be 300 K.

The combustor wall is 8 mm long, as the combustion chamber, and has a width of 0.2 mm, as shown in Figure 8.11a. The thermal boundary conditions of the faces of the solid domain turned outside up and downstream were considered to be adiabatic. On the outer face of the combustor wall was imposed the temperature

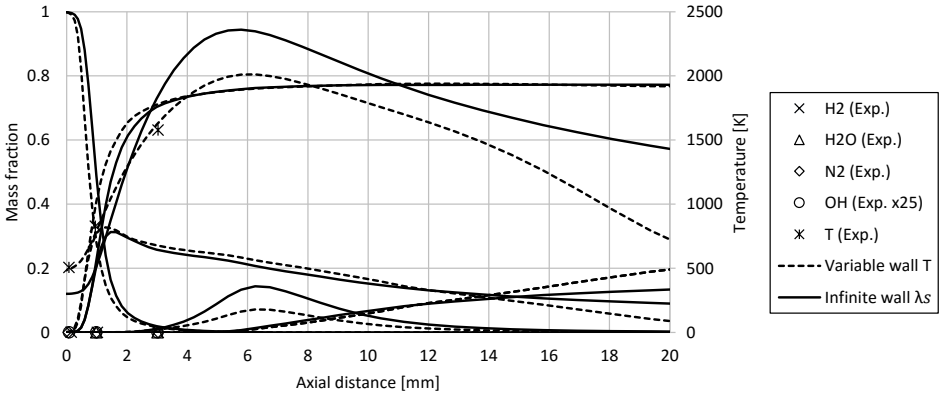

Figure 8.9: Comparison of measured and computed axial profiles of temperature, major species and OH mass fractions, with different thermal boundary conditions on the solid domain, for hydrogen jet diffusion flames with Re = 30. Experimental measurements obtained by Cheng et al [34].

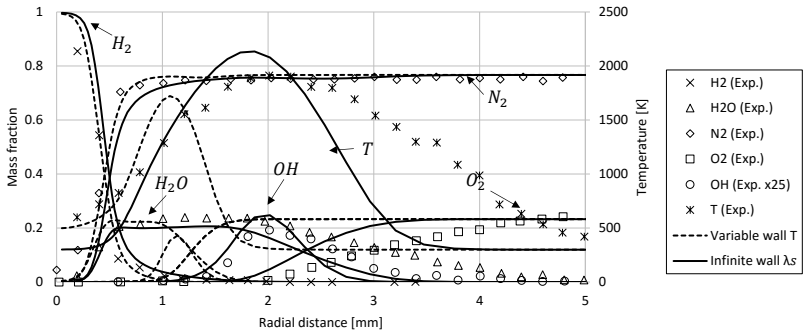

Figure 8.10: Comparison of measured and computed radial profiles of temperature, major species and OH mass fractions, at x = 0.1 mm, with different thermal boundary conditions on the solid domin, for hydrogen jet diffusion flames with Re = 30. Experimental measurements obtained by Cheng et al [34].

gradient expressed in Equation 8.1:

$$\frac{\partial T}{\partial n} = -\frac{h(T_{cell,s} - T_\infty) + \epsilon\sigma(T_{cell,s}^4 - T_\infty^4)}{\lambda_{solid}} \tag{8.1}$$

where h is the heat transfer coefficient, 10 W/m^{2}K; $T_{cell,s}$ is considered to be equal to the mean temperature of the cell in the solid domain immediately next transversally to the boundary at each time instant; ϵ is the wall material emissivity; T_∞ is the ambient temperature, 300 K; λ_{solid} is the wall thermal conductivity. According to Li et al [29], the micro-combustor wall is made of stainless-steel, with the following properties: thermal conductivity is 20 W/mK, density is 8000 kg/m^3, the specific heat is 450 J/kgK and the emissivity is 0.5. Two cases are simulated, the first one just composed by a wedge and the second one is 3D. The grid used for these cases is very similar, it is composed of 25 by 80 cells in the fluid domain and 5 by 80 in the solid domain. The difference is that the 3D case has more than just one line of cells radially, contrarily to the wedge case. Both of them are represented in Figures 8.11b and 8.11c, respectively.

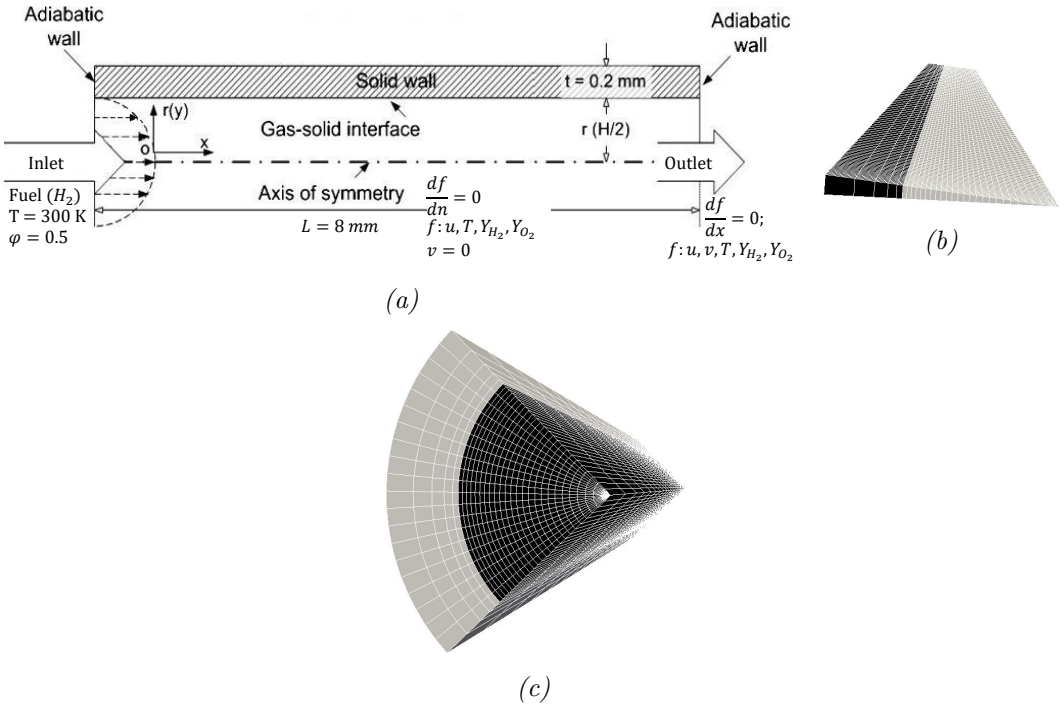

Figure 8.11: a) Schematic ilustration of computational domain coupled with boundary conditions, b) computational mesh, of hydrogen premixed flames in an axysymmetric channel.

8.2.1.2 Results and discussion

Figure 8.12 shows the comparison between the computed isopleths of hydrogen mass fraction, axial velociy and temperature, respectively, obtained by Li et al [29] using Fluent and using *chtlaminarSMOKE* in OpenFOAM, for the two simulated cases. In Figure 8.12a it is possible to see very similar isopleths, although when using *chtlaminarSMOKE* for the 3D case the H_2 is totally consumed a bit earlier than when using Fluent, and the opposite for the wedge case. In the three cases, it happened when the reacting gases were under development, as it can be seen in Figure 8.12b. The axial velocity profiles show overall a similar development of the flow, although it seems using *chtlaminarSMOKE* the flow reaches a FD profile further upstream when comparing with Fluent. These differences may come from the fact that an uniform profile was employed along with the *chtlaminarSMOKE* simulation. Figure 8.12c shows the temperature isopleths both in the fluid and solid domain with a overall very good agreement between each other. It seems that the wedge case is more similar with Fluent than the 3D case, as it is possible to verify in Figure 8.14. It can be noticed that there is a higher temperature of the upstream wall for the 3D when comparing with Fluent and the wedge case.

Figure 8.13 and 8.14 show the comparison between obtained temperatures profiles at the centerline and outer surface of the wall, respectively, both for *chlaminarSMOKE* cases and Fluent. As evident in Figure 8.13, the obtained profiles for the *chlaminarSMOKE* cases seems to be more alike the obtained profile by Fluent for a 2D channel with $H = 0.4$ mm, which was unexpected to see. In Figure 8.14,

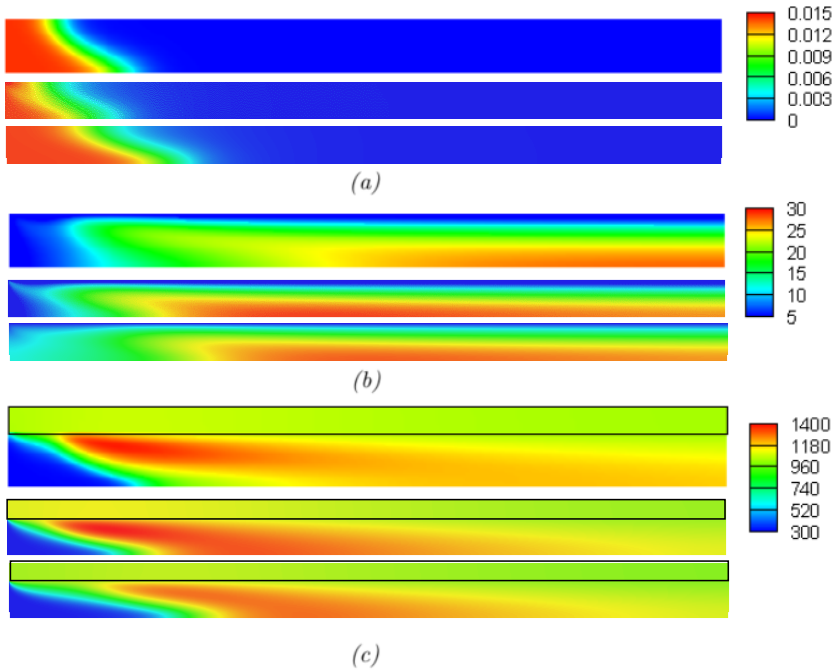

Figure 8.12: Comparion between computed isopleths, upper using Fluent, middle using chtlaminarSMOKE 3D and lower using chtlaminarSMOKE wedge in OpenFOAM: a) hydrogen mass fraction, b) axial velocity, c) temperature. Fluent isopleths obtained by Li et al [29].

it possible to see that the profiles have a similar behaviour, both presenting wall temperature peak at nearly the same axial distance and then decreasing relatively slowly until the end of the micro-combustor. The peak temperature for Fluent and for the wedge case are relatively similar, for the first is around 1065 K and the second is 1060 K, whereas for the 3D case is around 1120 K.

Finally, to be noted that these simulation took around 300 CPU hours using the cluster.

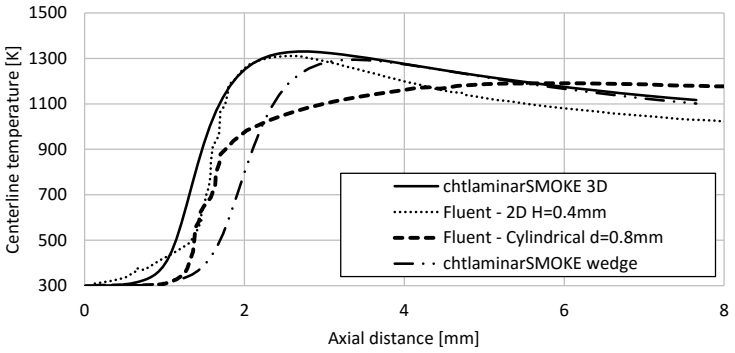

Figure 8.13: Temperature profiles at centerline using chtlaminarSMOKE and Fluent. Fluent curves obtained by Li et al [29].

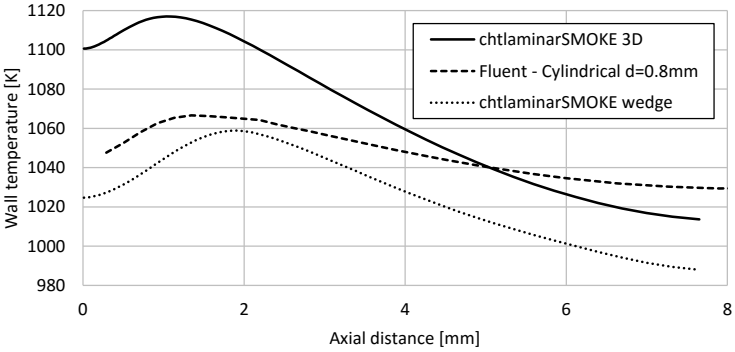

Figure 8.14: Temperature profiles at outer surface of the combustor wall in the axial direction, using chtlaminarSMOKE and Fluent. Fluent curve obtained by Li et al [29].

Chapter 9

Conclusion and Future Work

9.1 Conclusion

There were mainly three objectives for this thesis. The first one was to validate the gas phase model, *laminarSMOKE*, developed by Politecnico di Milano by applying it to mesoscale combustors. Four different studies were performed in order to do so. Firstly, premixed flames in 1D using H_2 as fuel were simulated, in *OpenSMOKE* framework. Afterwards, the same simulation was made using CH_4 as fuel instead of H_2, for different equivalence ratios. Thirdly, a simulation of coflow diffusion flames fed with a mixture of H_2/N_2 was performed. Finally, and similarly to the last one, a simulation of coflow diffusion flames fed a mixture of CH_4 was made. The first study, that had no experimental data at hand to compare with, showed a very good agreement with computed results obtained by [48]. In the remaining cases, all obtained results had overall a very good agreement with the experimental values available in each due section. This proves that *laminarSMOKE* code is suitable for simulations at macro and meso-scale combustion.

The second objective was to execute numerical simulations using the gas phase model applied to micro-scale combustion flows and analyse its capability to correctly describe these type of flows. Several types of micro-combustion chambers and flows were simulated in order to better analyse the versatility of the gas phase model in these situations. It was concluded that *laminarSMOKE* is not capable of simulating a combustion flow in a micro-chamber autonomously, due to the fact that the surface to volume ratio increases deeply from macro to micro-scale and the heat loss through the combustor walls can no longer be neglected. To overcome this limitation, several thermal boundary conditions were employed in the computational domain attempting to simulate the existence of walls. The thermal BC that allowed to obtain results in better agreement with other CFD softwares and experimental values was the imposition of temperature profiles obtained in the homologous studies. Without these, employing temperature gradients based on the energy conservation equation transversally and unidirectionally through the combustor walls lead to either sustainable flames with temperature and mass fraction profiles considerably different from the results obtained by homologous studies, or no sustainable flames at all.

Due to the previous adversities, a new version of the *laminarSMOKE* code was developed, named *chtlaminarSMOKE*, one that included the possibility of sim-

ulating combustor walls represented by an additional solid domain in which only the energy equation is solved through a coupled approach with the fluid domain. This code was validated against analytical results in a case of transient heat transfer in a forced convection in laminar flow. Two numerical studies were then performed: laminar hydrogen micro-jet diffusion flames and hydrogen premixed flames in a cylindrical micro-tube. In both studies, the results obtained were substantially in better agreements than the ones obtained when neglecting the wall effects.

The third and last objective was to perform a numerical simulation on coflow diffusion flames fed with a mixture of H_2/N_2 to study the effect of inserting a porous media within the combustion chamber, on the emission of pollutant gases, at meso-scale, using *laminarSMOKE*. It was observed that the decrease of the temperature imposed at the porous surface also decreased the NO_x formation. Furthermore, reducing the size of the porous media, and consequently the porous holes that the combustion flow has to go through, results in higher velocities of the flow and therefore lower residence times, which leads to lower NO_x formation.

Overall, with the current tools and applications available for the OpenFOAM framework, it is not possible to use this software autonomously to study combustion flows at micro-scale. However, the obtained results in Chapter 8 using the new *chtlaminarSMOKE* code version served as a proof that it can be a step forward towards that, enabling the usage of this open source to study the micro-combustion phenomena. A few suggestions on the next steps to take, are to be made in the next section.

9.2 Future Work

Both the *laminarSMOKE* code developed by Politecnico di Milano that enables the simulation of the gas phase and the *chtlaminarSMOKE* code developed in this thesis to include the heat transport at the walls in the simulation, demonstrated great potential to allow the study of combustion at micro-scale channels. However, there is still plenty to be done until managing to get the proper credibility of results.

Firstly, the code of *chtlaminarSMOKE* should be developed to allow performing simulations using parallel processing. This would enable obtaining results much faster whatever the level of refinement of the grid or the fuel considered, which otherwise in certain cases could easily take years to simulate.

Secondly, much more numerical simulations either on diffusion or premixed flames using different fuels have to be performed using the *chtlaminarSMOKE* code, ideally with the parallel processing feature mentioned above already included in the code. Particular attention should be paid on the type of boundary conditions predefined in the computational domain, whether it is imposed empty, cyclic, wedge, symmetryPlane, to understand their influence in the results, as well as the assumption of adiabatic conditions in some cases.

Thirdly, once the code is mature enough, a next step on the study of combustion flows at micro-scale can be taken and study more complex cases, such as the

Heat Recirculating Reactor or the swiss-roll, that involve heat transfer from exhaust to unburned gases through the combustor walls. Combustion flows at micro-scale involving catalytic reactions would be another type of study to be made.

Finally, technological efforts should be made in order to develop experimental procedures and techniques capable of measuring accurately the variables involved in micro-combustion, in this way allowing to have credible values to compare with when obtaining results from numerical simulations.

Overall, it can be said that these steps would increase deeply the potential to use the open source framework OpenFOAM to perform simulations on combustion flows at micro-scale, with a free cost and assured credibility.

Bibliography

[1] S. K. Chou, W. M. Yang, K. J. Chua, J. Li, and K. L. Zhang. Development of micro power generators - A review. Applied Energy, 88(1):1–16, 2011.

[2] Y. Ju and K. Maruta. Microscale combustion: Technology development and fundamental research. Progress in Energy and Combustion Science, 37(6):669–715, 2011.

[3] D. C. Walther and J. Ahn. Advances and challenges in the development of power-generation systems at small scales. Progress in Energy and Combustion Science, 37(5):583–610, 2011.

[4] N. S. Kaisare and D. G. Vlachos. A review on microcombustion: Fundamentals, devices and applications. Progress in Energy and Combustion Science, 38(3):321–359, 2012.

[5] F. J. Weinberg. The first halfmillion years of combustion research and today's burning problems. Plenary Lecture, 15th (Int.) Symposium on Combustion, Tokyo, Japan, 1974.

[6] M. Ayoobi. Chemical structures and dynamics in laminar flame propagation. Faculty of the Louisiana State University and Agricultural and Mechanical College, December 2015.

[7] C. Pinho. Sistemas Térmicos. Departamento de Engenharia Mecânica, Faculdade de Engenharia da Universidade do Porto, February 2014.

[8] J. A. Barnard and J. N. Bradley. Flame and combustion. London ; New York : Chapman and Hall, 2nd ed edition, 1985.

[9] V. K. Khanna. A Study of the Dynamics of Laminar and Turbulent Fully and Partially Premixed Flames. PhD thesis, Virginia Polytechnic Institute and State University, 2001.

[10] K. K. Kuo. Principles of combustion. A Wiley-Interscience publication. Wiley, 1986.

[11] S. Kikui, H. Nakamura, T. Tezuka, S. Hasegawa, and K. Maruta. Study on combustion and ignition characteristics of ethylene, propylene, 1-butene and 1-pentene in a micro flow reactor with a controlled temperature profile. Combustion and Flame, 163(April 2016):209–219, 2016.

[12] A. N. Gutkowski and T. Parra-Santos. Quenching Distance and Quenching Diameter Ratio for Flames Propagating In Propane / Air Mixtures. V(36):1–7, 2014.

[13] A. Epstein, S. Senturia, O. Al-Midani, G. Anathasuresh, A. A. Ayon, K. Breuer, K. S. Chen, F. Ehrich, E. Esteve, L. Frechette, and et al. Micro-heat engines, gas turbines, and rocket engines - The MIT microengine project. Fluid Dynamics and Co-located Conferences. American Institute of Aeronautics and Astronautics, 1980.

[14] A. Mehra and I. A. Waitz. Development of a hydrogen combustor for a microfabricated gas turbine engine. Solid-State Sensor and Actuator Workshop at Hilton, pages 35–40, 1998.

[15] S. Tanaka, K. Hikichi, S. Togo, M. Murayama, Y. Hirose, and T. Sakurai. World's smallest gas turbine establishing Brayton cycle. The 7th International Workshop on Micro and Nanotechnology for Power Generation and Energy Conversion Applications, pages 359–62, 2007.

[16] K. Fu, A. J. Knobloch, F. C. Martinez, D. C. Walther, C. Fernandez-Pello, A. I. P. Pisano, and D. Liepmann. Design and experimental results of small-scale rotary engines. Proceedings of 2001 ASME International Mechanical Engineering Congress and Exposition, 2001.

[17] H. T. Aichlmayr, D. B. Kittelson, and M. R. Zachariah. Micro-HCCI combustion: Experimental characterization and development of a detailed chemical kinetic model with coupled piston motion. Combustion and Flame, 135(3):227–248, 2003.

[18] S. A. Lloyd and F. J. Weinberg. A burner for mixtures of very low heat content. Nature, 251(5470):47–49, 1974.

[19] F. J. Weinberg. Combustion temperatures: the future? Nature, 233:239–241, 1971.

[20] C. M. Spadaccini, J. Lee, S. Lukachko, I. A. Waitz, A. Mehra, and X. Zhang. High Power Density Silicon Combustion Systems for Micro Gas Turbine Engines. Volume 1: Turbo Expo 2002, 1(June):469–481, 2002.

[21] S. Raimondeau, D. G. Norton, D. G. Vlachos, and R. I. Masel. Modeling of high-temperature microburners. Proceedings of the Combustion Institute, 29(1):901–907, 2002.

[22] D. G. Norton and D. G. Vlachos. Combustion characteristics and flame stability at the microscale: A CFD study of premixed methane/air mixtures. Chemical Engineering Science, 58(21):4871–4882, 2003.

[23] J. Hua, M. Wu, and K. Kumar. Numerical simulation of the combustion of hydrogen-air mixture in micro-scaled chambers. Part I: Fundamental study. Chemical Engineering Science, 60(13):3497–3506, 2005.

[24] J. Hua, M. Wu, and K. Kumar. Numerical simulation of the combustion of hydrogen-air mixture in micro-scaled chambers Part II: CFD analysis for a micro-combustor. Chemical Engineering Science, 60(13):3507–3515, 2005.

[25] J. A. Federici and D. G. Vlachos. A computational fluid dynamics study of propane/air microflame stability in a heat recirculation reactor. Combustion and Flame, 153(1-2):258–269, 2008.

[26] N. S. Kaisare and D. G. Vlachos. Extending the region of stable homogeneous micro-combustion through forced unsteady operation. Proceedings of the Combustion Institute, 31 II:3293–3300, 2007.

[27] J. Li, S. K. Chou, W. M. Yang, and Z. W. Li. A numerical study on premixed micro-combustion of CH4-air mixture: Effects of combustor size, geometry and boundary conditions on flame temperature. Chemical Engineering Journal, 150(1):213–222, 2009.

[28] T. Aikun, P. Jianfeng, S. Xia, and X. Hong. Numerical Simulation Study of Premixed Hydrogen-Oxygen Combustion Process in Micro-scale Rectangular Channel. 2011 International Conference on Computer Distributed Control and Intelligent Environmental Monitoring, pages 520–524, 2011.

[29] J. Li, S. K. Chou, Z. W. Li, and W. M. Yang. A comparative study of H2-air premixed flame in micro combustors with different physical and boundary conditions. Combustion Theory and Modelling, 12(2):325–347, 2008.

[30] D. G. Norton and D. G. Vlachos. A CFD study of propane/air microflame stability. Combustion and Flame, 138(1-2):97–107, 2004.

[31] A. I. Rahaghi, M.S. Saidi, M. H. Saidi and M. B. Shafii. Two-Dimensional Numerical Investigation of a Micro Combustor. Scientia Iranica, 6(6):433–442, 2011.

[32] J. Li, Y. Wang, J. Shi, and X. Liu. Dynamic behaviors of premixed hydrogen-air flames in a planar micro-combustor filled with porous medium. Fuel, 145:70–78, 2015.

[33] A. A. Mohamad. Combustion in porous media: fundamentals and applications. In D.B. Ingham and I. Pop, editors, Transport Phenomena in Porous Media III, pages 287 – 304. Pergamon, Oxford, – edition, 2005.

[34] T. S. Cheng, C. Y. Wu, C. P. Chen, Y. H. Li, Y. C. Chao, T. Yuan, and T. S. Leu. Detailed measurement and assessment of laminar hydrogen jet diffusion flames. Combustion and Flame, 146(1-2):268–282, 2006.

[35] A. Hossain and Y. Nakamura. Thermal and chemical structures formed in the micro burner of miniaturized hydrogen-air jet flames. Proceedings of the Combustion Institute, 35(3):3413–3420, 2015.

[36] C. Fernandez-Pello. Micropower generation using combustion: Issues and approaches. Proceedings of the Combustion Institute, 29(1):883 – 899, 2002. Proceedings of the Combustion Institute.

[37] F. J. Weinberg, D. M. Rowe, G. Min, and P. D. Ronney. On thermoelectric power conversion from heat recirculating combustion systems. Proceedings of the Combustion Institute, 29(1):941 – 947, 2002. Proceedings of the Combustion Institute.

[38] J. A. Federici, D. G. Norton, T. Brüggemann, K. W. Voit, E. D. Wetzel, and D. G. Vlachos. Catalytic microcombustors with integrated thermoelectric elements for portable power production. Journal of Power Sources, 161(2):1469 – 1478, 2006.

[39] J. Vican, B. F. Gajdeczko, F. L. Dryer, D. L. Milius, I. A. Aksay, and R. A. Yetter. Development of a microreactor as a thermal source for microelectromechanical systems power generation. Proceedings of the Combustion Institute, 29(1):909 – 916, 2002. Proceedings of the Combustion Institute.

[40] K. Bijjula, E. D. Wetzel, and D. G. Vlachos. Optimization of Integrated Thermoelectric / Microcombustor Devices. pages 558–561, 2009.

[41] K. H. Lee and O. C. Kwon. Studies on a heat-recirculating microemitter for a micro thermophotovoltaic system. Combustion and Flame, 153(1–2):161 – 172, 2008.

[42] Y. Li, H. Li, D. Dunn-Rankin, and Y. Chao. Enhancing thermal, electrical efficiencies of a miniature combustion-driven thermophotovoltaic system. Progress in Photovoltaics: Research and Applications, 17(7):502–512, 2009.

[43] Y. Wenming, C. Siawkiang, S. Chang, X. Hong, and L. Zhiwang. Effect of wall thickness of micro-combustor on the performance of micro-thermophotovoltaic power generators. Sensors and Actuators A: Physical, 119(2):441 – 445, 2005.

[44] W. Ming-Hsun, Y. Richard, and Y. Vigor. Development and Characterization of Ceramic Micro Chemical Propulsion and Combustion Systems, book section –, pages 0 – 1. Aerospace Sciences Meetings. American Institute of Aeronautics and Astronautics, 2008.

[45] D. H. Lewis Jr., S. W. Janson, R. B. Cohen, and E. K. Antonsson. Digital micropropulsion. Sensors and Actuators A: Physical, 80(2):143 – 154, 2000.

[46] A. P. London, A. A. Ayon, A. H. Epstein, S. M. Spearing, T. Harrison, Y. Peles, and J. L. Kerrebrock. Microfabrication of a high pressure bipropellant rocket engine. Sensors and Actuators A: Physical, 92(1):351–357, 2001.

[47] A. Cuoci, A. Frassoldati, T. Faravelli, and E. Ranzi. A computational tool for the detailed kinetic modeling of laminar flames: Application to C2H4/CH4 coflow flames. Combustion and Flame, 160(5):870–886, 2013.

[48] A. Cuoci, A. Frassoldati, T. Faravelli, and E. Ranzi. Numerical modeling of laminar flames with detailed kinetics based on the operator-splitting method. Energy and Fuels, 27(12):7730–7753, 2013.

[49] T.P. Coffee and J. M. Heimerl. Transport algorithms for premixed, laminar steady-state flames. Combustion and Flame, 43:273 – 289, 1981.

[50] R. J. Hall. The radiative source term for plane-parallel layers of reacting combustion gases. Journal of Quantitative Spectroscopy and Radiative Transfer, 49(5):517 – 523, 1993.

[51] G. Strang. On the construction and comparison of difference schemes. SIAM Journal on Numerical Analysis, 5(3):506–517, 1968.

[52] R. I. Issa. Solution of the implicitly discretised fluid flow equations by operator-splitting. Journal of Computational Physics, 62:40–65, January 1986.

[53] E. Ranzi, A. Frassoldati, R. Grana, A. Cuoci, T. Faravelli, A. P. Kelley, and C. K. Law. Hierarchical and comparative kinetic modeling of laminar flame speeds of hydrocarbon and oxygenated fuels. Progress in Energy and Combustion Science, 38(4):468 – 501, 2012.

[54] E. Ranzi, A. Frassoldati, S. Granata, and T. Faravelli. Wide-range kinetic modeling study of the pyrolysis, partial oxidation, and combustion of heavy n-alkanes. Industrial & engineering chemistry research, 44(14):5170–5183, 2005.

[55] Detailed mechanism of the pyrolysis, partial oxidation and combustion of hydrocarbon fuels up to 3 c atoms. http://creckmodeling.chem.polimi.it/images/site/kinetic_mechanisms/version1412/POLIMI_C1C3_LT_1412.CKI. Accessed: 2016-07-04.

[56] OpenFOAM Foundation. OpenFOAM ® - The Open Source Computational Fluid Dynamics (CFD) Toolbox, openfoam ® –, pages 0–1. OpenFOAM ®. American Institute of Aeronautics and Astronautics, December 2015.

[57] P. Krysl. A pragmatic introduction to the finite element method for thermal and stress analysis. Personal Communication, 2005.

[58] The incomplete swak4foam reference. https://openfoamwiki.net/images/d/db/Swak4FoamReference.pdf. Accessed: 2016-07-04.

[59] The paraview tutorial. http://myweb.clemson.edu/~eduffy/sc09_tutorials/docs/tut102/ParaViewTutorial36.pdf. Accessed: 2016-07-04.

[60] V. V. Toro, A. V. Mokhov, H. B. Levinsky, and M. D. Smooke. Combined experimental and computational study of laminar, axisymmetric hydrogen-air diffusion flames. Proceedings of the Combustion Institute, 30:485–492, 2005. Cited By (since 1996): 7.

[61] B. A. V. Bennett, C. S. McEnally, L. D. Pfefferle, and M. D. Smooke. Computational and experimental study of axisymmetric coflow partially premixed methane/air flames. Combustion and Flame, 123(4):522–546, 2000.

[62] K. J. Bosschaart and L. P. H. de Goey. The laminar burning velocity of flames propagating in mixtures of hydrocarbons and air measured with the heat flux method. Combustion and Flame, 136(3):261 – 269, 2004.

[63] X. J. Gu, M. Z. Haq, M. Lawes, and R. Woolley. Laminar burning velocity and markstein lengths of methane–air mixtures. Combustion and Flame, 121(1–2):41 – 58, 2000.

[64] F. Halter, T. Tahtouh, and C. Mounaïm-Rousselle. Nonlinear effects of stretch on the flame front propagation. Combustion and Flame, 157(10):1825 – 1832, 2010.

[65] O. Park, P. S. Veloo, N. Liu, and F. N. Egolfopoulos. Combustion characteristics of alternative gaseous fuels. Proceedings of the Combustion Institute, 33(1):887 – 894, 2011.

[66] J. Gibson, M. Ayoobi, and I. Schoegl. Behavior of preheated premixed flames at rich conditions. Proceedings of the Combustion Institute, 34(1):997–1005, 2013.

[67] I. Schoegl. Natural parameterizations of flame structure and heat release in lean premixed ch4/air combustion. Combustion and Flame, 161(7):1735–1743, 2014.

[68] M. Ayoobi and I. Schoegl. Dominant chemical source and reaction modes in lean premixed h2/air flames. Proceedings of the Combustion Institute, 35(1):787–794, 2015.

[69] L. Nettis. Conjugate Heat Transfer: Strategies and Applications. PhD thesis, Politecnico di Bari, 2011.

[70] D. Panara and B. E. Noll. A coupled solver for the solution of the unsteady conjugate heat transfer problem. Int. Conf. on Computational Methods for Coupled Problems in Science and Engineering, pages 1–4, 2007.

[71] M. N. Ozisik. Heat Conduction, pages 303–307. Wiley-Interscience. New York, 1997.

Appendix A

Kinetic mechanisms

A.1 POLIMI-H2CO-1412

CHEMICAL REACTIONS

Units: [kmol, m3, s], [-] and [cal/mol]

---

1. O2 + H = O + OH
   k: 9.600000e+11 -0.20 16625.00
2. H2 + O = H + OH
   k: 4.330000e+10 0.00 10000.00
3. O2 + H (+M) = HO2 (+M)
   Fall-off (Troe)
   k0: 8.400000e+11 -0.80 0.00
   kInf: 5.580000e+09 0.40 0.00
   Troe Parameters
   a 5.00e-01
   T*** 1.00e-30
   T* 1.00e+30
   T** 0.00e+00
   H2O enhanced by 18.000
   H2 enhanced by 2.500
   N2 enhanced by 1.260
   AR enhanced by 0.800
   HE enhanced by 0.800
   CO enhanced by 1.200
   CO2 enhanced by 2.400
4. OH + HO2 = O2 + H2O
   k: 5.000000e+10 0.00 1000.00
5. H + HO2 = 2OH
   k: 2.500000e+11 0.00 1900.00
6. O + HO2 = O2 + OH
   k: 3.250000e+10 0.00 0.00
7. 2OH = H2O + O
   k: 3.570000e+01 2.40 -2110.00
8. H2 +M = 2H +M
   k: 1.115000e+11 0.00 96081.00
   H2 enhanced by 2.500
   H2O enhanced by 12.000
   AR enhanced by 0.500
   CO enhanced by 1.900
   CO2 enhanced by 3.800
9. O2 +M = 2O +M
   k: 1.550000e+11 0.00 115120.00
   H2 enhanced by 2.500
   H2O enhanced by 12.000
   AR enhanced by 0.200
   HE enhanced by 0.200
   CO enhanced by 1.900
   CO2 enhanced by 3.800
10. H + OH +M = H2O +M
    k: 4.500000e+16 -2.00 0.00
    H2O enhanced by 16.000
    H2 enhanced by 2.000
    CO2 enhanced by 1.900
11. H + HO2 = O2 + H2
    k: 2.500000e+10 0.00 700.00
12. 2HO2 = O2 + H2O2
    k: 2.110000e+09 0.00 0.00
13. 2OH (+M) = H2O2 (+M)
    Fall-off (Troe)
    k0: 1.300000e+12 -0.90 -1700.00
    kInf: 7.400000e+10 -0.37 0.00
    Troe Parameters
    a 7.35e-01
    T*** 9.40e+01
    T* 1.76e+03
    T** 5.18e+03
    H2 enhanced by 2.000
    H2O enhanced by 6.000
    CO enhanced by 1.500
    CO2 enhanced by 2.000
    AR enhanced by 0.700
    HE enhanced by 0.700
    N2 enhanced by 0.900
14. O + OH +M = HO2 +M
    k: 1.000000e+10 0.00 0.00
15. O2 + CO = CO2 + O
    k: 2.530000e+09 0.00 47700.00
16. O2 + HCO = CO + HO2
    k: 3.000000e+09 0.00 0.00
17. CO + O (+M) = CO2 (+M)
    Fall-off (Lindemann)
    k0: 2.070000e+20 -3.34 7610.00
    kInf: 9.640000e+07 0.00 3800.00
    H2O enhanced by 12.000
    H2 enhanced by 2.000
    CO enhanced by 1.500
    CO2 enhanced by 2.000
    AR enhanced by 0.500
18. CO + OH = CO2 + H
    k: 9.600000e+08 0.14 7352.00
19. CO + OH = CO2 + H
    k: 7.320000e+07 0.03 -16.00
20. CO + HO2 = CO2 + OH
    k: 3.000000e+10 0.00 23000.00
21. H2O + CO = H2 + CO2
    k: 2.000000e+08 0.00 38000.00
22. HCO +M = CO + H +M
    k: 1.200000e+14 -1.00 17000.00
    H2O enhanced by 5.000
    CO2 enhanced by 3.000
    H2 enhanced by 1.900

CO enhanced by 1.900

23. O + HCO = CO2 + H
k: 3.000000e+10 0.00 0.00

24. H + HCO = H2 + CO
k: 5.000000e+10 0.00 0.00

25. OH + HCO = H2O + CO
k: 5.000000e+10 0.00 0.00

26. HO2 + HCO = H2O2 + CO
k: 4.000000e+08 0.00 0.00

27. HO2 + HCO => CO2 + H + OH
k: 3.000000e+10 0.00 0.00

28. H2O + H = H2 + OH
k: 4.800000e+07 1.00 19000.00

29. H2O2 + H = H2O + OH
k: 2.410000e+10 0.00 3970.00

30. H2O2 + H = H2 + HO2
k: 6.025000e+10 0.00 7950.00

31. H2O + HO2 => H2O2 + OH
k: 5.388000e+02 2.00 28780.05

32. H2O2 + OH => H2O + HO2
k: 3.195000e+02 2.00 -4169.95

33. H2O2 + O => OH + HO2
k: 1.083000e+03 2.00 -1657.32

A.2 POLIMI-H2CO-NOX-1412

CHEMICAL REACTIONS

Units: [kmol, m3, s], [-] and [cal/mol]

---

1. O2 + H = O + OH
   k: 9.600000e+11 -0.20 16625.00
2. H2 + O = H + OH
   k: 4.330000e+10 0.00 10000.00
3. O2 + H (+M) = HO2 (+M)
   Fall-off (Troe)
   k0: 8.400000e+11 -0.80 0.00
   kInf: 5.580000e+09 0.40 0.00
   Troe Parameters
   a 5.00e-01
   T*** 1.00e-30
   T* 1.00e+30
   T** 0.00e+00
   H2O enhanced by 18.000
   H2 enhanced by 2.500
   N2 enhanced by 1.260
   AR enhanced by 0.800
   HE enhanced by 0.800
   CO enhanced by 1.200
   CO2 enhanced by 2.400
4. OH + HO2 = O2 + H2O
   k: 5.000000e+10 0.00 1000.00
5. H + HO2 = 2OH
   k: 2.500000e+11 0.00 1900.00
6. O + HO2 = O2 + OH
   k: 3.250000e+10 0.00 0.00
7. 2OH = H2O + O
   k: 3.570000e+01 2.40 -2110.00
8. H2 +M = 2H +M
   k: 1.115000e+11 0.00 96081.00
   H2 enhanced by 2.500
   H2O enhanced by 12.000
   AR enhanced by 0.500
   CO enhanced by 1.900
   CO2 enhanced by 3.800
9. O2 +M = 2O +M
   k: 1.550000e+11 0.00 115120.00
   H2 enhanced by 2.500
   H2O enhanced by 12.000
   AR enhanced by 0.200
   HE enhanced by 0.200
   CO enhanced by 1.900
   CO2 enhanced by 3.800
10. H + OH +M = H2O +M
    k: 4.500000e+16 -2.00 0.00
    H2O enhanced by 16.000
    H2 enhanced by 2.000
    CO2 enhanced by 1.900
11. H + HO2 = O2 + H2
    k: 2.500000e+10 0.00 700.00
12. 2HO2 = O2 + H2O2
    k: 2.110000e+09 0.00 0.00
13. 2OH (+M) = H2O2 (+M)
    Fall-off (Troe)
    k0: 1.300000e+12 -0.90 -1700.00
    kInf: 7.400000e+10 -0.37 0.00
    Troe Parameters
    a 7.35e-01
    T*** 9.40e+01
    T* 1.76e+03
    T** 5.18e+03
    H2 enhanced by 2.000
    H2O enhanced by 6.000
    CO enhanced by 1.500
    CO2 enhanced by 2.000
    AR enhanced by 0.700
    HE enhanced by 0.700
    N2 enhanced by 0.900
14. O + OH +M = HO2 +M
    k: 1.000000e+10 0.00 0.00
15. O2 + CO = CO2 + O
    k: 2.530000e+09 0.00 47700.00
16. O2 + HCO = CO + HO2
    k: 3.000000e+09 0.00 0.00
17. CO + O (+M) = CO2 (+M)
    Fall-off (Lindemann)
    k0: 2.070000e+20 -3.34 7610.00
    kInf: 9.640000e+07 0.00 3800.00
    H2O enhanced by 12.000
    H2 enhanced by 2.000
    CO enhanced by 1.500
    CO2 enhanced by 2.000
    AR enhanced by 0.500
18. CO + OH = CO2 + H
    k: 9.600000e+08 0.14 7352.00
19. CO + OH = CO2 + H
    k: 7.320000e+07 0.03 -16.00
20. CO + HO2 = CO2 + OH
    k: 3.000000e+10 0.00 23000.00
21. H2O + CO = H2 + CO2
    k: 2.000000e+08 0.00 38000.00
22. HCO +M = CO + H +M
    k: 1.200000e+14 -1.00 17000.00
    H2O enhanced by 5.000
    CO2 enhanced by 3.000
    H2 enhanced by 1.900

CO enhanced by 1.900
23. O + HCO = CO2 + H
k: 3.000000e+10 0.00 0.00
24. H + HCO = H2 + CO
k: 5.000000e+10 0.00 0.00
25. OH + HCO = H2O + CO
k: 5.000000e+10 0.00 0.00
26. HO2 + HCO = H2O2 + CO
k: 4.000000e+08 0.00 0.00
27. HO2 + HCO => CO2 + H + OH
k: 3.000000e+10 0.00 0.00
28. H2O + H = H2 + OH
k: 4.800000e+07 1.00 19000.00
29. H2O2 + H = H2O + OH
k: 2.410000e+10 0.00 3970.00
30. H2O2 + H = H2 + HO2
k: 6.025000e+10 0.00 7950.00
31. NH3 +M = H + NH2 +M
k: 2.200000e+13 0.00 93470.00
32. H + NH2 = H2 + NH
k: 4.000000e+10 0.00 3650.00
33. O + NH2 = HNO + H
k: 6.600000e+11 -0.50 0.00
34. O + NH2 = NH + OH
k: 6.800000e+09 0.00 0.00
35. O + NH2 = NO + H2
k: 1.300000e+05 1.02 -627.00
36. O2 + NH2 = HNO + OH
k: 4.500000e+09 0.00 25000.00
37. OH + NH2 = H2O + NH
k: 4.000000e+03 2.00 1000.00
38. HO2 + NH2 = OH + H2NO
k: 5.000000e+10 0.00 0.00
39. O + H2NO = O2 + NH2
k: 2.000000e+11 0.00 0.00
40. N + NH2 = N2 + 2H
k: 7.000000e+10 0.00 0.00
41. NH + NH2 = N2H2 + H
k: 5.000000e+10 0.00 0.00
42. 2NH2 = H2 + N2H2
k: 8.500000e+08 0.00 0.00
43. 2NH2 = NH3 + NH
k: 5.000000e+10 0.00 10000.00
44. 2NH2 (+M) = N2H4 (+M)
Fall-off (Lindemann)
k0: 1.000000e+12 0.00 0.00
kInf: 1.500000e+10 0.00 0.00
N2 enhanced by 2.500
H2O enhanced by 5.000
NH3 enhanced by 10.000
45. NO + NH2 = NNH + OH
k: 8.900000e+09 -0.35 0.00
46. NO + NH2 = N2 + H2O
k: 1.720000e+16 -2.29 1058.00
47. NO2 + NH2 = N2O + H2O
k: 3.200000e+15 -2.20 0.00
48. NO2 + NH2 = NO + H2NO
k: 3.500000e+09 0.00 0.00
49. H + NH = H2 + N
k: 3.000000e+10 0.00 0.00
50. O + NH = NO + H
k: 9.200000e+10 0.00 0.00
51. NH + OH = HNO + H
k: 2.000000e+10 0.00 0.00
52. NH + OH = H2O + N
k: 5.000000e+08 0.50 2000.00
53. NH + OH = NO + H2
k: 2.000000e+10 0.00 0.00
54. O2 + NH = HNO + O
k: 4.600000e+02 2.00 6500.00
55. O2 + NH = NO + OH
k: 1.300000e+03 1.50 100.00
56. 2NH = N2 + 2H
k: 2.500000e+10 0.00 0.00
57. N + NH = N2 + H
k: 3.000000e+10 0.00 0.00
58. NO + NH = N2 + OH
k: 2.200000e+10 -0.23 0.00
59. NO2 + NH = N2O + OH
k: 1.000000e+10 0.00 0.00
60. N + OH = NO + H
k: 3.800000e+10 0.00 0.00
61. O2 + N = NO + O
k: 6.400000e+06 1.00 6280.00
62. NO + N = N2 + O
k: 3.300000e+09 0.30 0.00
63. N2H4 + H = H2 + N2H3
k: 1.300000e+10 0.00 2500.00
64. N2H4 + O = N2H2 + H2O
k: 8.500000e+10 0.00 1200.00
65. N2H4 + OH = H2O + N2H3
k: 4.000000e+10 0.00 0.00
66. N2H4 + NH2 = NH3 + N2H3
k: 3.900000e+09 0.00 1500.00
67. N2H3 +M = N2H2 + H +M
k: 3.500000e+13 0.00 46000.00
68. H + N2H3 = 2NH2
k: 1.600000e+09 0.00 0.00
69. O + N2H3 = N2H2 + OH
k: 5.000000e+09 0.00 5000.00
70. O + N2H3 = HNO + NH2
k: 1.000000e+10 0.00 0.00

71. OH + N2H3 = N2H2 + H2O
k: 1.000000e+10 0.00 1000.00
72. OH + N2H3 = HNO + NH3
k: 1.000000e+09 0.00 15000.00
73. NH + N2H3 = N2H2 + NH2
k: 2.000000e+10 0.00 0.00
74. N2H2 +M = H + NNH +M
k: 5.000000e+13 0.00 50000.00
N2 enhanced by 2.000
H2 enhanced by 2.000
O2 enhanced by 2.000
H2O enhanced by 15.000
75. N2H2 + H = H2 + NNH
k: 5.000000e+10 0.00 1000.00
76. N2H2 + O = NO + NH2
k: 1.000000e+10 0.00 1000.00
77. N2H2 + O = NNH + OH
k: 2.000000e+10 0.00 1000.00
78. N2H2 + OH = H2O + NNH
k: 1.000000e+10 0.00 1000.00
79. NO + N2H2 = N2O + NH2
k: 4.000000e+09 0.00 11922.00
80. N2H2 + NH = NNH + NH2
k: 1.000000e+10 0.00 1000.00
81. N2H2 + NH2 = NH3 + NNH
k: 1.000000e+10 0.00 1000.00
82. NNH = N2 + H
k: 1.000000e+07 0.00 0.00
83. H + NNH = N2 + H2
k: 1.000000e+11 0.00 0.00
84. O + NNH = N2O + H
k: 1.000000e+11 0.00 0.00
85. O + NNH = NO + NH
k: 5.000000e+10 0.00 0.00
86. NNH + OH = N2 + H2O
k: 5.000000e+10 0.00 0.00
87. O2 + NNH = N2 + HO2
k: 6.670000e+10 0.00 0.00
88. O2 + NNH = N2 + O2 + H
k: 5.000000e+10 0.00 0.00
89. NH + NNH = N2 + NH2
k: 5.000000e+10 0.00 0.00
90. NNH + NH2 = N2 + NH3
k: 5.000000e+10 0.00 0.00
91. NO + NNH = N2 + HNO
k: 5.000000e+10 0.00 0.00
92. HNNO +M = N2O + H +M
k: 2.200000e+12 0.00 21600.00
93. HNNO +M = N2 + OH +M
k: 1.000000e+12 0.00 25600.00
94. HNNO + H = N2O + H2
k: 2.000000e+10 0.00 0.00
95. HNNO + H = NNH + OH
k: 1.000000e+10 0.00 0.00
96. HNNO + O = N2O + OH
k: 2.000000e+10 0.00 0.00
97. HNNO + O = O2 + NNH
k: 1.000000e+10 0.00 0.00
98. HNNO + OH = N2O + H2O
k: 2.000000e+10 0.00 0.00
99. HNNO + OH = NNH + HO2
k: 1.000000e+10 0.00 0.00
100. NO + HNNO = N2O + HNO
k: 1.000000e+09 0.00 0.00
101. NO + HNNO = NO2 + NNH
k: 3.200000e+09 0.00 270.00
102. NO2 + HNNO = NO3 + NNH
k: 1.000000e+10 0.00 0.00
103. NO2 + HNNO = N2O + HONO
k: 1.000000e+09 0.00 0.00
104. NO + HO2 = NO2 + OH
k: 2.100000e+09 0.00 -480.00
105. NO + O +M = NO2 +M
k: 7.500000e+13 -1.41 0.00
N2 enhanced by 1.700
O2 enhanced by 1.500
H2O enhanced by 10.000
106. NO + OH (+M) = HONO (+M)
Fall-off (Lindemann)
k0: 2.330000e+17 -2.40 0.00
kInf: 2.000000e+10 0.00 0.00
107. NO + HCO = HNO + CO
k: 7.200000e+09 0.00 0.00
108. NO + H +M = HNO +M
k: 4.000000e+14 -1.75 0.00
N2 enhanced by 1.000
H2O enhanced by 4.100
H2 enhanced by 1.250
109. HNO + H = NO + H2
k: 4.400000e+08 0.72 650.00
110. HNO + O = NO + OH
k: 1.000000e+10 0.00 0.00
111. HNO + OH = NO + H2O
k: 3.600000e+10 0.00 0.00
112. O2 + HNO = NO + HO2
k: 1.000000e+10 0.00 25000.00
113. HNO + NH2 = NO + NH3
k: 2.000000e+10 0.00 1000.00
114. NO + HNO = N2O + OH
k: 2.000000e+09 0.00 26000.00
115. NO2 + HNO = NO + HONO
k: 6.000000e+08 0.00 2000.00

116. 2HNO = N2O + H2O
k: 9.000000e+05 0.00 3100.00
117. NO2 + H2 = HONO + H
k: 3.000000e+10 0.00 29000.00
118. HONO + O = NO2 + OH
k: 1.200000e+10 0.00 6000.00
119. HONO + OH = NO2 + H2O
k: 4.000000e+09 0.00 0.00
120. HONO + NH = NO2 + NH2
k: 1.000000e+10 0.00 0.00
121. HONO + NH2 = NO2 + NH3
k: 5.000000e+09 0.00 0.00
122. 2HONO = NO + NO2 + H2O
k: 1.020000e+10 0.00 8540.00
123. H2NO +M = HNO + H +M
k: 1.000000e+13 0.00 50000.00
124. H + H2NO = HNO + H2
k: 3.000000e+04 2.00 2000.00
125. H + H2NO = OH + NH2
k: 5.000000e+10 0.00 0.00
126. O + H2NO = HNO + OH
k: 3.000000e+04 2.00 2000.00
127. OH + H2NO = HNO + H2O
k: 2.000000e+04 2.00 1000.00
128. NO + H2NO = 2HNO
k: 2.000000e+01 2.00 13000.00
129. NH2 + H2NO = HNO + NH3
k: 3.000000e+09 0.00 1000.00
130. NO2 + H2NO = HNO + HONO
k: 6.000000e+08 0.00 2000.00
131. NO3 + H = NO2 + OH
k: 6.000000e+10 0.00 0.00
132. O + NO3 = O2 + NO2
k: 1.000000e+10 0.00 0.00
133. NO3 + OH = NO2 + HO2
k: 1.400000e+10 0.00 0.00
134. NO3 + HO2 = O2 + NO2 + OH
k: 1.500000e+09 0.00 0.00
135. NO2 + NO3 = NO + O2 + NO2
k: 5.000000e+07 0.00 2940.00
136. NO3 = NO + O2
k: 2.500000e+06 0.00 12000.00
137. 2NO3 = O2 + 2NO2
k: 5.100000e+08 0.00 6750.00
138. NO2 + HCO = NO + CO2 + H
k: 8.400000e+12 -0.75 1930.00
139. NO2 + H = NO + OH
k: 1.320000e+11 0.00 360.00
140. NO2 + O = NO + O2
k: 3.900000e+09 0.00 -238.00
141. NO2 + O +M = NO3 +M
k: 2.940000e+15 -2.00 0.00
142. NO2 + HO2 = O2 + HONO
k: 6.310000e+05 1.25 5000.00
143. 2NO2 = 2NO + O2
k: 1.600000e+09 0.00 26123.00
144. 2NO2 = NO + NO3
k: 9.600000e+06 0.73 20923.00
145. 2NO2 = NO + NO3
k: 1.600000e+09 0.00 26123.00
146. NO2 + CO = NO + CO2
k: 9.040000e+10 0.00 33800.00
147. NO2 + HCO = HONO + CO
k: 1.200000e+20 -3.29 2355.00
148. CO2 + N = NO + CO
k: 1.900000e+08 0.00 3400.00
149. N2O +M = N2 + O +M
k: 4.000000e+11 0.00 56100.00
N2 enhanced by 1.700
O2 enhanced by 1.400
H2O enhanced by 12.000
CO enhanced by 1.500
CO2 enhanced by 3.000
150. N2O + H = N2 + OH
k: 3.300000e+07 0.00 4729.00
151. N2O + H = N2 + OH
k: 4.400000e+11 0.00 19254.00
152. NO + NH = N2O + H
k: 3.190000e+11 -0.46 0.00
153. N2O + O = 2NO
k: 2.900000e+10 0.00 23150.00
154. N2O + O = N2 + O2
k: 1.400000e+09 0.00 10800.00
155. N2O + OH = N2 + HO2
k: 2.000000e+09 0.00 40000.00
156. HNO2 + H = NO2 + H2
k: 2.400000e+05 1.50 5087.00
157. HNO2 + O = NO2 + OH
k: 1.700000e+05 1.50 3020.00
158. HNO2 + OH = NO2 + H2O
k: 1.200000e+03 2.00 -596.00
159. HNO2 = HONO
k: 1.300000e+29 -5.47 52814.00
160. NO2 + OH (+M) = HONO2 (+M)
Fall-off (Troe)
k0: 6.420000e+26 -5.49 2351.00
kInf: 2.400000e+10 0.00 0.00
Troe Parameters
a 5.25e-01
T*** 1.00e-15
T* 1.00e-15
T** 1.00e+15

H2O enhanced by 5.000
161. HONO2 + OH = H2O + NO3
k: 1.030000e+07 0.00 -1240.00
162. H2 + NH2 => NH3 + H
k: 1.576000e+02 2.00 3954.86
163. H2O + HO2 => H2O2 + OH
k: 5.388000e+02 2.00 28780.05
164. H2O + NH2 => NH3 + OH
k: 1.126000e+02 2.00 8169.13
165. NO2 + H2O2 => HONO + HO2
k: 6.831000e+02 2.00 14711.89
166. H2O2 + OH => H2O + HO2
k: 3.195000e+02 2.00 -4169.95
167. H2O2 + O => OH + HO2
k: 1.083000e+03 2.00 -1657.32
168. H2O2 + NH2 => NH3 + HO2
k: 9.005000e+00 2.00 -1507.20
169. O2 + NH3 => HO2 + NH2
k: 5.111000e+04 2.00 60086.33
170. NH3 + H => H2 + NH2
k: 7.220000e+04 2.00 15302.86
171. NH3 + OH => H2O + NH2
k: 1.198000e+04 2.00 4067.13
172. NH3 + O => OH + NH2
k: 4.060000e+04 2.00 13586.66
173. NH3 + HO2 => H2O2 + NH2
k: 1.616000e+03 2.00 27340.80

Appendix B

Evolution in time of emitted pollutants gases of numerical investigation regarding porous media insertion

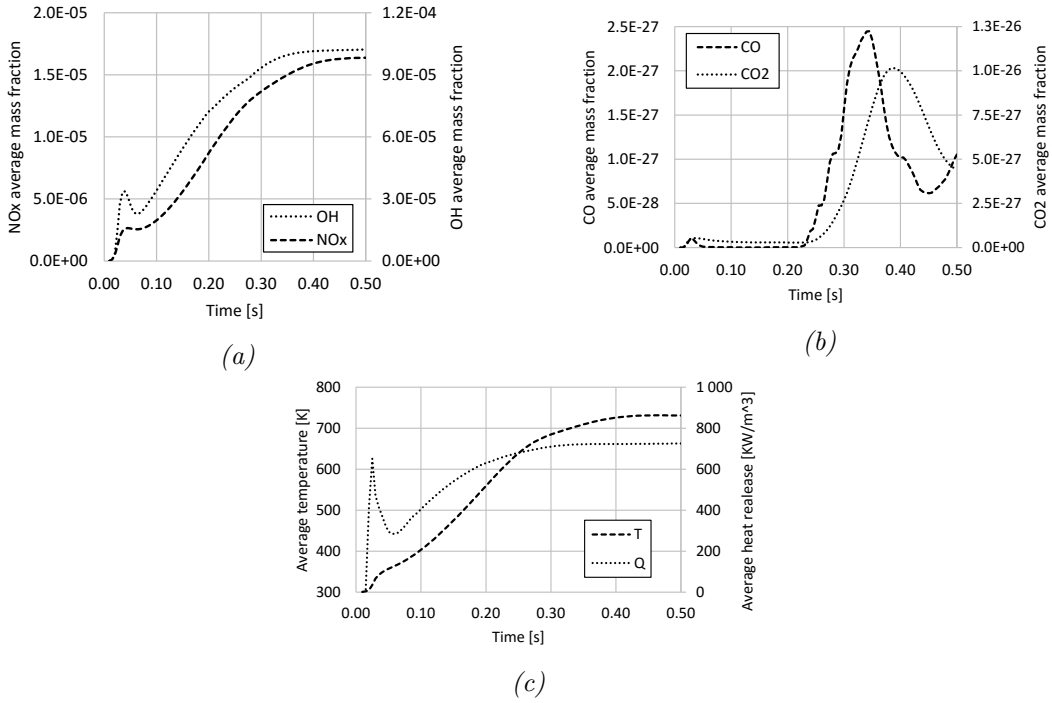

Figure B.1: Average temperature and mass fractions of emited pollutant gases in function of time, of H_2/N_2 coflow flames with inserted porous media in the combustion chamber, for the case (a.0) - without porous.

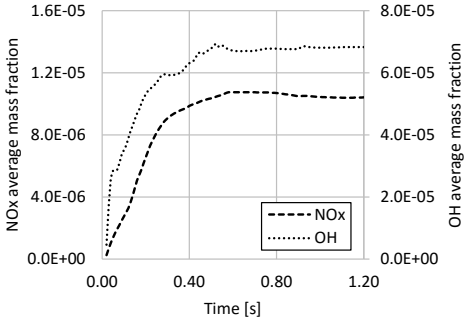

(a)

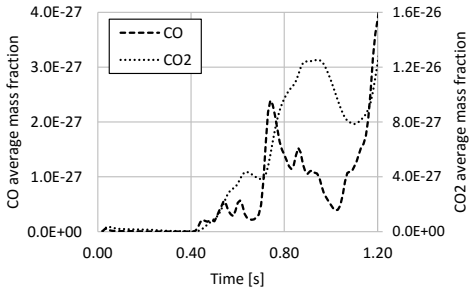

(b)

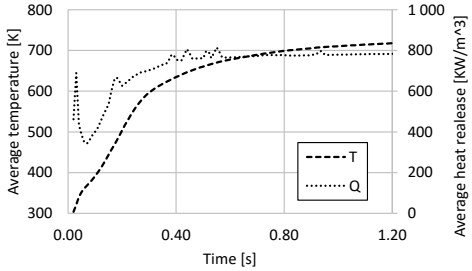

(c)

Figure B.2: Average temperature and mass fractions of emited pollutant gases in function of time, of H_2/N_2 coflow flames with inserted porous media in the combustion chamber, for the case (a.1) - adiabatic porous surface.

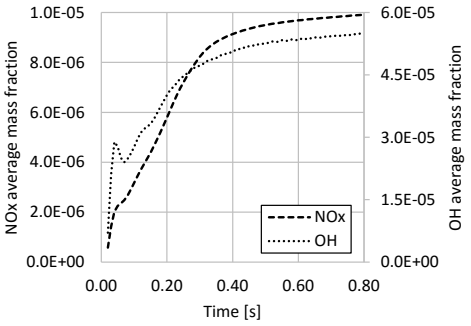

(a)

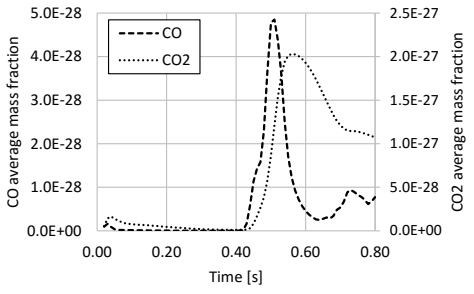

(b)

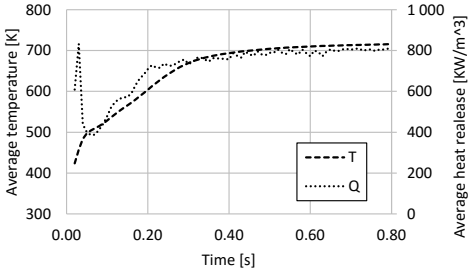

(c)

Figure B.3: Average temperature and mass fractions of emited pollutant gases in function of time, of H_2/N_2 coflow flames with inserted porous media in the combustion chamber, for the case (a.2) - $T = 1000$ K at porous surface.

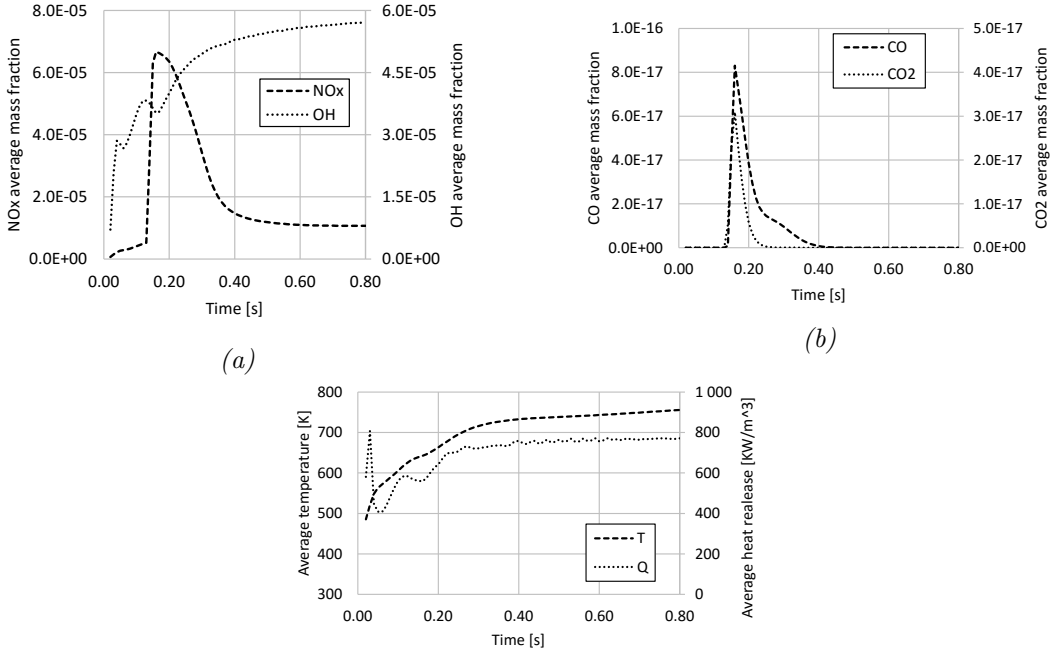

Figure B.4: Average temperature and mass fractions of emited pollutant gases in function of time, of H_2/N_2 coflow flames with inserted porous media in the combustion chamber, for the case (a.3) - $T = 1250$ K at porous surface.

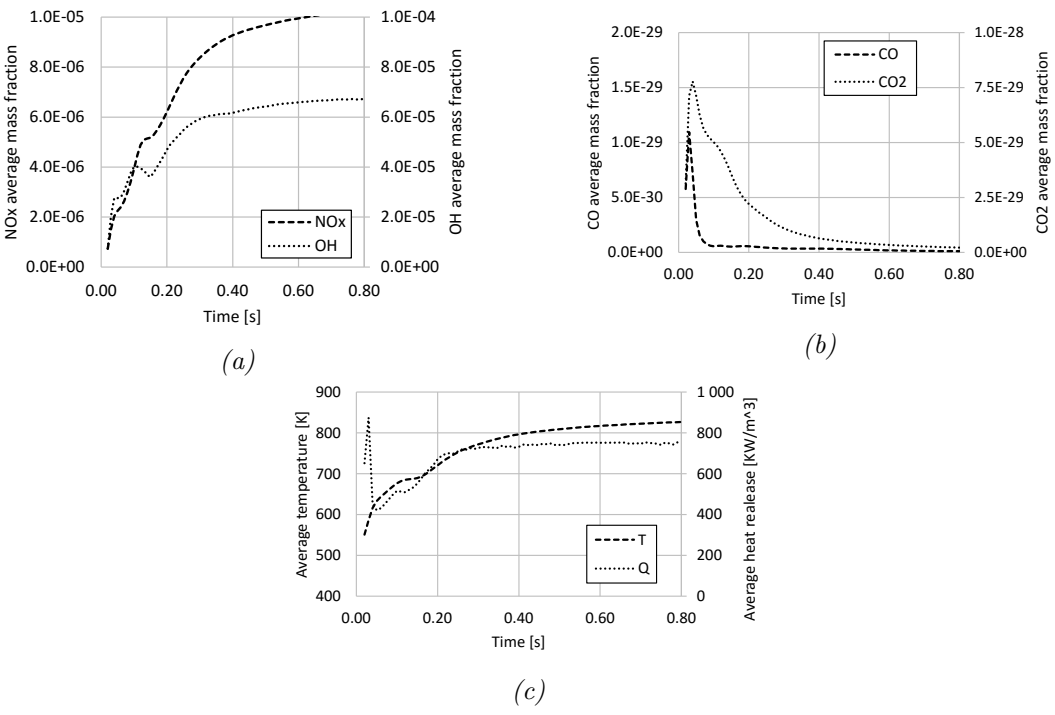

Figure B.5: Average temperature and mass fractions of emited pollutant gases in function of time, of H_2/N_2 coflow flames with inserted porous media in the combustion chamber, for the case (a.4) - $T = 1500$ K at porous surface.

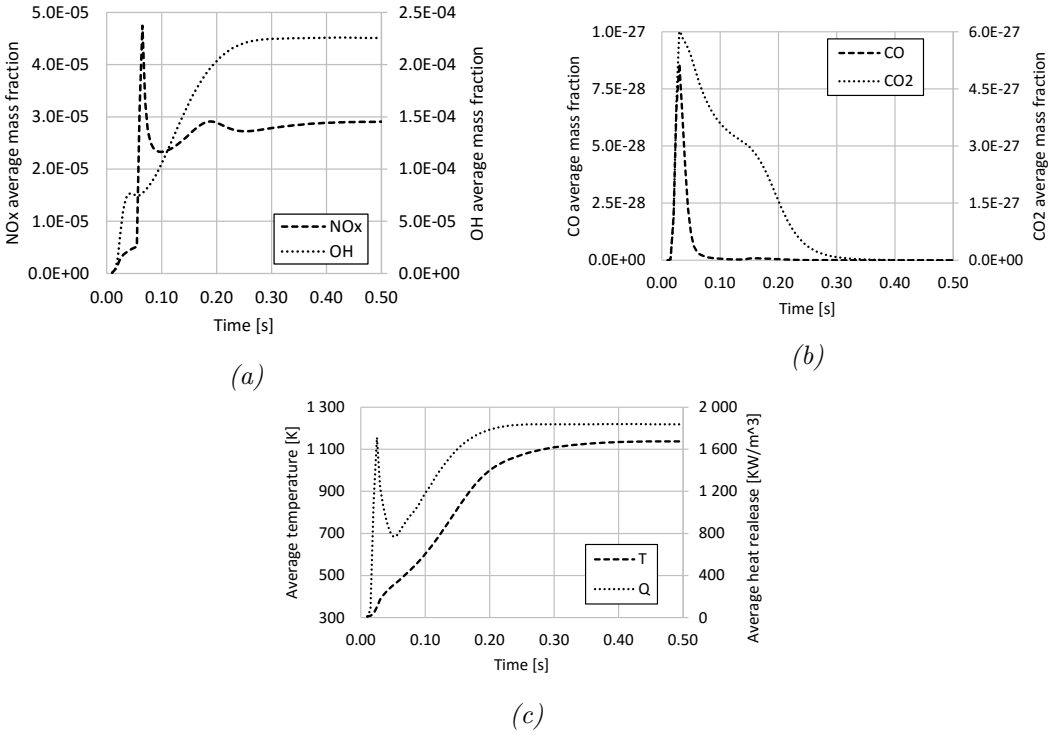

Figure B.6: Average temperature and mass fractions of emited pollutant gases in function of time, of H_2/N_2 coflow flames with inserted porous media in the combustion chamber, for the case (b.0) - without porous.

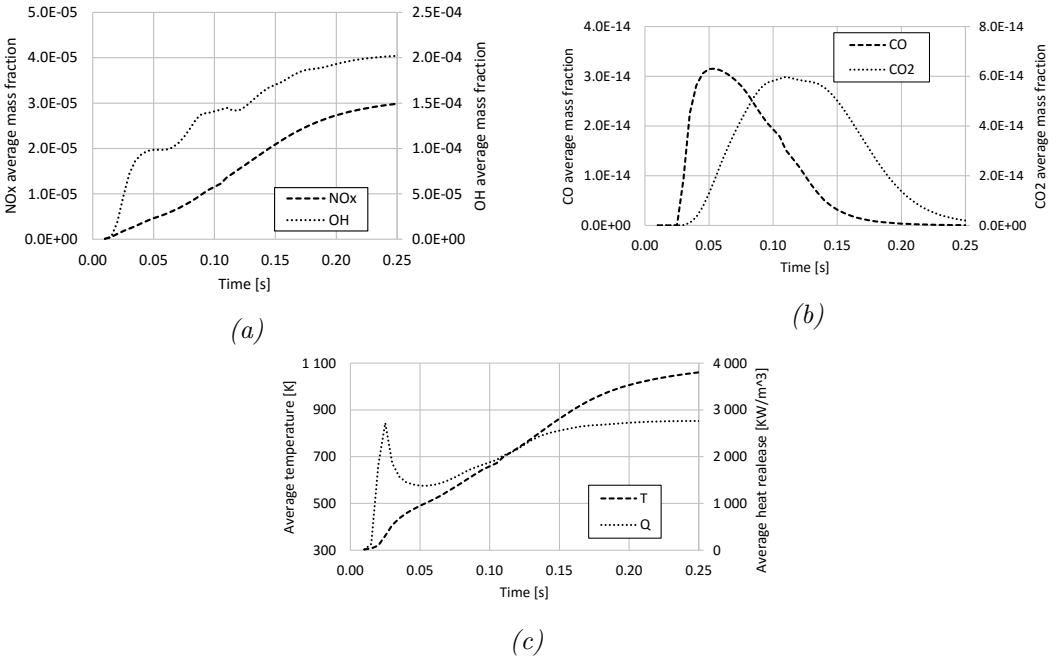

Figure B.7: Average temperature and mass fractions of emited pollutant gases in function of time, of H_2/N_2 coflow flames with inserted porous media in the combustion chamber, for the case (b.1) - adiabatic porous surface.

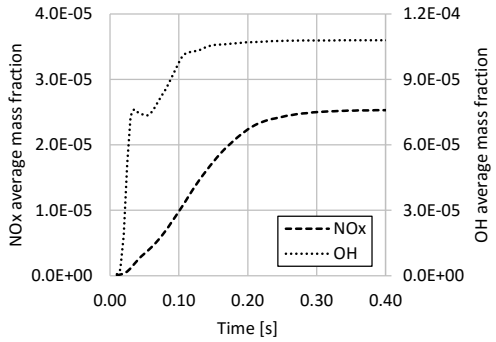

(a)

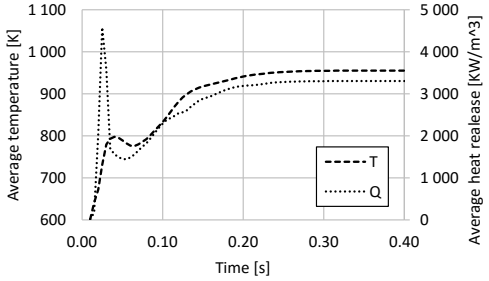

(b)

Figure B.8: Average temperature and mass fractions of emited pollutant gases in function of time, of H_2/N_2 coflow flames with inserted porous media in the combustion chamber, for the case (b.2) - $T = 1000$ K at porous surface.

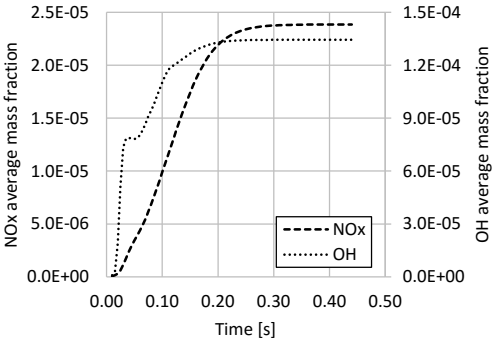

(a)

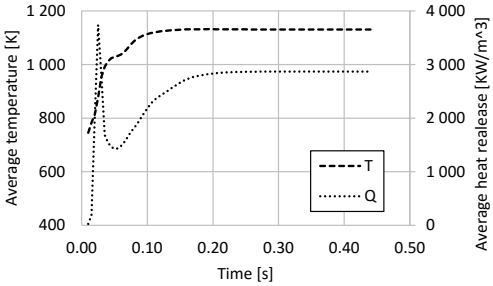

(b)

Figure B.9: Average temperature and mass fractions of emited pollutant gases in function of time, of H_2/N_2 coflow flames with inserted porous media in the combustion chamber, for the case (b.3) - $T = 1250$ K at porous surface.

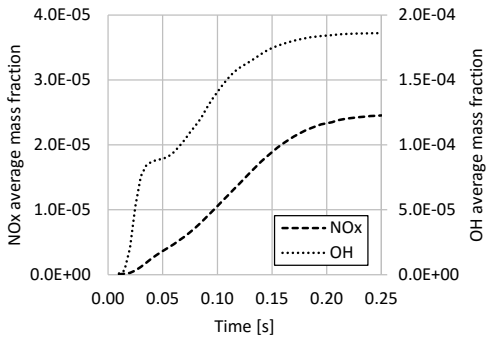

(a)

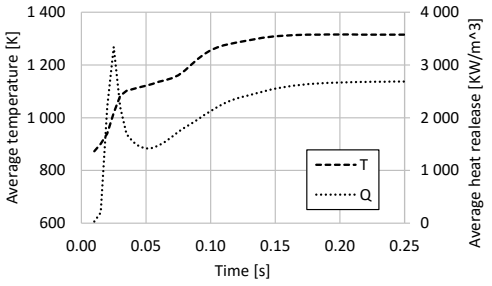

(b)

Figure B.10: Average temperature and mass fractions of emited pollutant gases in function of time, of H_2/N_2 coflow flames with inserted porous media in the combustion chamber, for the case (b.4) - $T = 1500$ K at porous surface.

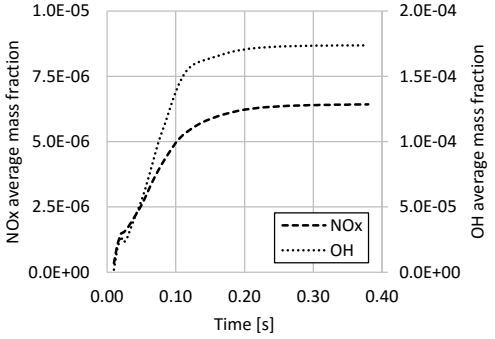

(a)

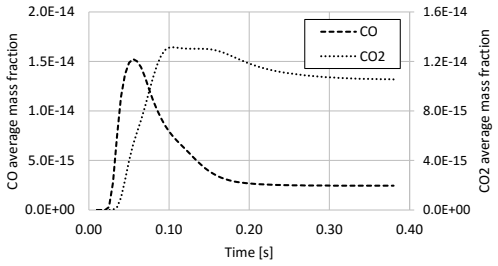

(b)

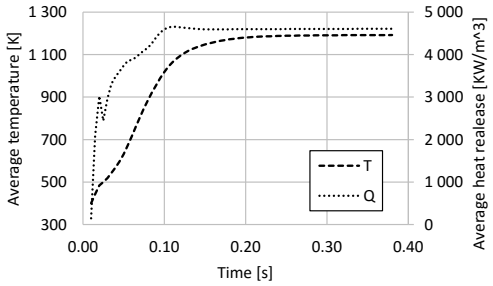

(c)

Figure B.11: Average temperature and mass fractions of emited pollutant gases in function of time, of H_2/N_2 coflow flames with inserted porous media in the combustion chamber, for the case (c.1) - T = 1000 K at porous surface.

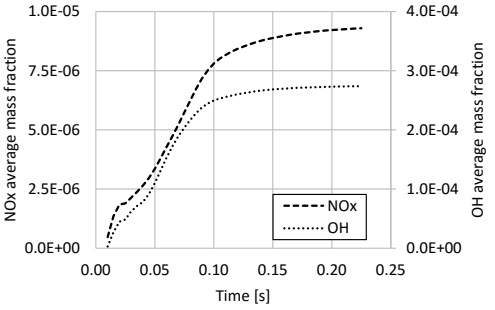

(a)

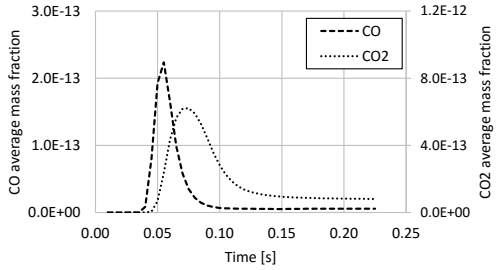

(b)

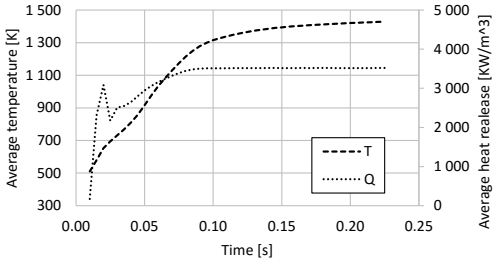

(c)

Figure B.12: Average temperature and mass fractions of emited pollutant gases in function of time, of H_2/N_2 coflow flames with inserted porous media in the combustion chamber, for the case (c.4) - T = 1500 K at porous surface.

Appendix C

chtlaminarSMOKE files

C.1 *Policy* file

```
    if(chtEquation == true)
    {
        while (mag(deltagrad)>innerRESI  && corrT < innerIT)
     {
         corrT=corrT+1;
      label solidInterface =
mesh2.boundaryMesh().findPatchID("solid_interface");
      label fluidInterface =
mesh.boundaryMesh().findPatchID("fluid_interface");
      if (-1 == solidInterface || -1 == fluidInterface)
      {
           error err("no solid or fluid interface");
           err.exit();
      }
      scalarField TsolidInterface = T2.boundaryField()
[solidInterface];
      scalarField TfluidInterface = T.boundaryField()
[fluidInterface];
      volVectorField gradT1cal = fvc::grad(T);
      volVectorField gradT2cal = fvc::grad(T2);
      fixedGradientFvPatchScalarField& gradTsolidInterface =
refCast<fixedGradientFvPatchScalarField>(T2.boundaryField()
[solidInterface]);
      scalarField& gradT2 =  gradTsolidInterface.gradient();
      surfaceVectorField unitNormals1 = mesh.Sf()/mesh.magSf();
      surfaceVectorField unitNormals2 =
mesh2.Sf()/mesh2.magSf();
      scalarField gradT1norm = gradT1cal.boundaryField()
[fluidInterface] & unitNormals1.boundaryField()
[fluidInterface];
      scalarField gradT2norm = gradT2cal.boundaryField()
[solidInterface] & unitNormals2.boundaryField()
[solidInterface];
      scalarField coeff = lambda/ksolid.component(tensor::XX);
        gradT2 = -gradT1norm*coeff;
      deltagrad = max(gradT2norm)-max(-gradT1norm*coeff);
            fvScalarMatrix T2Eqn
            (
                dTdt0*fvm::ddt(rhosolid*cpsolid,T2) -
fvm::laplacian(ksolid, T2)
            );
           T2Eqn.relax();
           fvOptions.constrain(T2Eqn);
           T2Eqn.solve(mesh2.solver("T"));
      T2.correctBoundaryConditions();
      fvOptions.correct(T2);
      T.boundaryField()[fluidInterface] ==  TsolidInterface;
      T.correctBoundaryConditions();
      fvOptions.correct(T);
        runTime.write();
              #include "TEqn.H"
     }
```

C.2 *transportProperties* file

```
/
*-----------------------------------------------------------------
--------------*\
| =========                 |
|
| \\      /  F ield         | OpenFOAM: The Open Source CFD
Toolbox           |
|  \\    /   O peration     | Version:  1.0
|
|   \\  /    A nd           | Web:
http://www.openfoam.org               |
|    \\/     M anipulation  |
|
\*-----------------------------------------------------------------
---------------*/

FoamFile
{
    version         2.0;
    format          ascii;

    root            "";
    case            "";
    instance        "";
    local           "";

    class           dictionary;
    object          transportProperties;
}

// * * * * * * * * * * * * * * * * * * * * * * * * * * * * * * * * *
* * * * * * * //
// choose input ksolid or DiffT on solverOptions file


ksolid   ksolid [1 1 -3 -1 0 0 0] (20. 0. 0. 0. 20. 0. 0. 0.
0.);

rhosolid    rhosolid [1 -3 0 0 0 0 0] 8000.;

cpsolid    cpsolid [0 2 -2 -1 0 0 0] 460.;

DiffT      DiffT [0 2 -1 0 0 0 0] (5.435e-06 0. 0. 0.
5.435e-06 0. 0. 0. 0.);

dTdt0            dTdt0 [0 0 0 0 0 0 0] 0.;

//
************************************************************
********** //
```